EUROPEAN COMMISSION

Community Research

# MATISSE

Materials' Innovations for Safe and Sustainable nuclear in Europe

**Support to the development of joint research actions between national programmes on advanced nuclear materials**

FP7-Fission-2013
Combination of Collaborative project (CP) and Coordination and Support Actions (CSA)

Grant agreement no: 604862
Start date: 01/11/2013 Duration: 48 Months

## *D.5.42*

# *Report for mech./microstr. character. of environ. assisted degrade. effects of steels in lead alloys and assess. of environm. degrad. effects on perf. of struct. and funct. comp. of MYRRHA ADS & LFR*

**MatISSE** – Contract Number: 604862

| | |
|---|---|
| Document title | Report for mech./microstr. character. of environ. assisted degrade. effects of steels in lead alloys and assess. of environm. degrad. effects on perf. of struct. and funct. comp. of MYRRHA ADS & LFR |
| Author(s) | M. Chocholousek (CVR), E. Stergar (SCK•CEN), X. Gong (SCK•CEN), P. Marmy (SCK•CEN), S. Gavrilov (SCK•CEN), F. Ersoy (SCK-CEN), M. Yurechko-Hussy (KIT), C. Schroer (KIT), J. Konys (KIT), J.B. Vogt (CNRS), I Proriol-Serre (CNRS), T. Auger (CNRS), B. Barkia (CNRS), Z. Spirit (CVR), F. Di Gabriele (CVR), A. Hojná (CVR) |
| Number of pages | 84 |
| Document type | Deliverable |
| Work Package | 5 |
| Document number | D5.42 |
| Issued by | CVREZ |
| Date of completion | 28/12/2017 |
| Dissemination level | Public |

**Summary**

This report aims at presenting the results obtained in the framework of the first subtask of the task 5.3, dedicated to fuel-cladding interaction.

**Approval**

| Rev. | Date | First author | WP leader | Project Coordinator |
|---|---|---|---|---|
| 0 | 12/2017 | M. Chocholousek (CVR) | K.F. Nilsson (JRC) | P.F. Giroux (CEA) |
| 1 | 08/2018 | M. Chocholousek (CVR) | K.F. Nilsson (JRC) | P.F. Giroux (CEA) |

**Distribution list**

| Name | Organisation | Comments |
|---|---|---|
| All beneficiaries | MatISSE | |

# Table of contents

# Abbreviations

| | |
|---|---|
| ADS | Accelerator Driven System |
| $A_g$ | Percentage plastic elongation at UTS |
| $A_{30}$ | is percentage plastic elongation after fracture: (Elongation after fracture)/(Initial gage length 30 mm) × 100% |
| $c_o$ | Oxygen concentration in liquid metal |
| COD | Crack Open Displacement |
| *D* | Gauge diameter |
| EBSD | Electron Back Scatter Diffraction |
| EDX/EDS | Energy-dispersive X-ray spectroscopy |
| $\varepsilon_R$ | Strain at rupture |
| $\varepsilon_S$ | Steady-state creep rate |
| FCG | Fatigue Crack Growth |
| FEG | Field Emission Gun |
| FIB | Focused Ion Beam Microscope |
| *Lo* | Distance between two shoulders |
| *Lc* | Gage length |
| *Lr* | Sampling length |
| LBE | Lead Bismuth Eutectic |
| LCF | Low Cycle Fatigue |
| HCF | High Cycle Fatigue |
| LME | Liquid Metal Embrittlement |
| $m_E$ | modulus of elasticity (tensile) |
| MYRRHA | Multi-purpose hYbrid Research Reactor for High-tech Application |
| $N_a$ | Number of cycles to initiate a macroscopic crack |
| $N_f$ | Number of cycles to failure |
| $R_\varepsilon$ | Strain Ratio |
| SEM | Scanning Electron Microscope |
| SSRT | Slow Strain Rate Tests |
| $\sigma$ | Uniaxial stress |
| TEM | Transmission Electron Microscope |
| YS | Yield Stress |
| UTS | Ultimate Tensile Strength |
| UE | Uniform elongation |
| T | Test temperature |
| TE | Total elongation |
| $t_R$ | Time-to-rupture |
| $t_{1,2}$ | Time corresponding to the transition of primary to secondary creep |
| $t_{2,3}$ | Time corresponding to the transition of secondary to tertiary creep |
| *Z* | Necking or reduction of cross-section area |

# 1 Introduction

Liquid lead and lead bismuth eutectic (LBE) are potential heat transfer liquids for future Gen-IV reactors. The Multi-purpose hYbrid Research Reactor for High-tech Applications (MYRRHA), currently under development at SCK•CEN in Mol, Belgium is an accelerator driven system (ADS) utilizing LBE as cooling liquid as well as spallation target [1, 2]. One critical factor in the development is therefore the compatibility of structural materials with the cooling liquid. Especially liquid metal embrittlement (LME) has gathered attention in the recent years as it might lead to premature failure of components [3, 4, 5, 6, 7, 8, 9, 10, 11] [12, 13, 14, 15, 16, 17, 18, 19] [20, 21, 22, 23]. In order to develop effective measures to mitigate and prevent liquid metal embrittlement it is crucial to investigate the underlying mechanisms. Therefore, this task is aimed at investigating the mechanisms of liquid metal embrittlement utilizing different mechanical testing methods combined with high resolution microscopy.

Austenitic stainless steels are a class of materials that are very important for conventional and advanced reactor technologies. They are Fe-Cr-Ni-Mo alloys with a fully or “quasifully” face-centered-cubic close-packed crystal structure which imparts most of their physical and mechanical properties. Various chemical additions enhance their properties over a wide range of temperatures. Austenitic steel of 316 type belongs to one of the main austenitic alloy classes that has a good combination of strength, ductility, and toughness at low and high temperature, along with good formability, weld ability, and corrosion properties. The 316 steels also have reasonably good creep resistance at high temperatures. The ferrite content of these steels is an important point since ferrite aging at high temperatures can lead to some brittle phase precipitation and to a toughness decrease. These steels are extensively used in nuclear power reactors. Made of type 316 austenitic stainless steels are pressure boundary pipes and the primary circuit of pressurized water reactors. Many austenitic stainless steels candidates for Generation IV systems belong to the same family (AISI 300 series) which was also used in the past. With regard to lead alloys-cooled technologies it is necessary to study the mechanical properties of these constructive materials in lead containing environment at elevated temperatures.

# 2 Background

The Ferritic-martensitic steel T91 has, due to its good corrosion resistance, excellent radiation and swelling resistance in fast neutron flux and high temperature mechanical properties. It is considered as a promising candidate for future Gen-IV reactors and also as material for the beam window of MYRRHA. Over the last decades extensive work has been conducted to investigate the LME characteristics of T91 under a wide variety of conditions.

Important results of these investigations were that LME seems to occur only in certain temperature range (the so-called ductility trough). Low oxygen concentrations in the LBE and slow strain rates are also considered to increase the susceptibility of T91 to LME.

The austenitic steel 316L is a low carbon-chromium-nickel-molybdenum steel with a wide variety of applications in the construction, industrial and nuclear energy fields. The mechanical properties of the steel were extensively studied in air. 316L has many favorable properties, including a high corrosion resistance, good mechanical strength at both low and high temperatures, high toughness and excellent machinability. As a result, its static or quasi static mechanical properties have attracted extensive attention [24, 25, 26, 27]. The mechanical test data of 316L stainless steels after 1500 hours aging at 290-400°C in air indicated negligible aging induced degradation: The short-term thermal aging did not cause any significant change in the strength and ductility as well as in the test-temperature dependence of those parameters [28]. It is used as a manufacturing material for nuclear fuel clad tubes and fuel sub assembly wrappers in fast breeder reactors owing to its superior mechanical properties at elevated temperatures and good compatibility with liquid sodium [29]. The expertise on compatibility of stainless steels with sodium is not transferable to lead and lead alloys, due to the significant differences in their physics and metallurgic properties [30]. Therefore, particular studies of constructive materials tested in heavy liquid metals is necessary.

# 3 Experimental

## 3.1 Tested Materials

The tested materials were the ferritic/martensitic steel T91 as well as the austenitic steels 316L and 15-15Ti. The chemical compositions can be found in Table 3-2. Material properties (according to EN ISO 6892) of the tested steels are summarized in Table 3-1, where $m_E$ is modulus of elasticity, YS- yield strength, UTS – ultimate

tensile strength, $A_g$ is percentage plastic elongation at UTS, $A_{30}$ is percentage elongation after fracture: (Elongation after fracture)/(Initial gage length 30 mm) × 100%, Z is reduction of cross-section area. The tests were performed on the rod shape specimens with 6 mm diameter.

Table 3-1: Mechanical properties of tested steels (CVR).

| Material | T | $m_E$ | YS | UTS | $A_g$ | $A_{30}$ | Z |
|---|---|---|---|---|---|---|---|
| | °C | GPa | MPa | MPa | % | % | % |
| T91 | 25 | 240 | 572 | 716 | 6.7 | 22.2 | 70 |
| T91 | 350 | 240 | 486 | 581 | 3.3 | 16.3 | 71 |
| 316L | 25 | 202 | 251 | 567 | 44.1 | 59.5 | 80 |
| 316L | 350 | 143 | 168 | 421 | 26.2 | 38.4 | 66 |
| 15-15Ti | 25 | 210 | 364 | 571 | 24.3 | 30.0* | 67 |
| 15-15Ti | 350 | 211 | 318 | 462 | 11.0 | 14.6* | 62 |

*Marked elongation is evaluated for rupture outside the measurement range. The value is just informative and the real value should be higher.

### 3.1.1 T91

Table 3-2: Chemical composition of ferritic/martensitic steel T91 (wt.%)

| *Lab.* | Fe | Cr | Mo | Ni | C | Si | Mn | P | S | Al | Cu | Nb | Ti | V | W | N | Sn | As |
|---|---|---|---|---|---|---|---|---|---|---|---|---|---|---|---|---|---|---|
| **SCK-CEN** | Bal. | 8.9 | 0.89 | 0.115 | 0.097 | 0.22 | 0.39 | 0.020 | 0.0005 | 0.010 | 0.08 | 0.08 | 0.004 | 0.20 | - | 0.0480 | - | - |
| **CNRS** | Bal. | 8,99 | 0,89 | 0,11 | 0,1025 | 0,22 | 0,38 | 0,021 | 0,0004 | 0,0146 | 0,06 | 0,06 | 0,0034 | 0,21 | 0,01 | 0,0442 | 0,004 | 0,008 |

Heat treatment:

The steel T91 was austenitized at 1050°C with a holding time of 1 min/mm followed by water quenching. This was followed by an annealing treatment at 770°C with a holding time of 3 min/mm followed by air cooling.

Material was provided as 15 mm thick plates. The final microstructure is shown in Figure 3.1 and Figure 3.2. The material had a fully martensitic structure with a prior austenitic grain size of 20 ± 5 µm. The Vickers macro hardness was about 220 ± 1 HV.

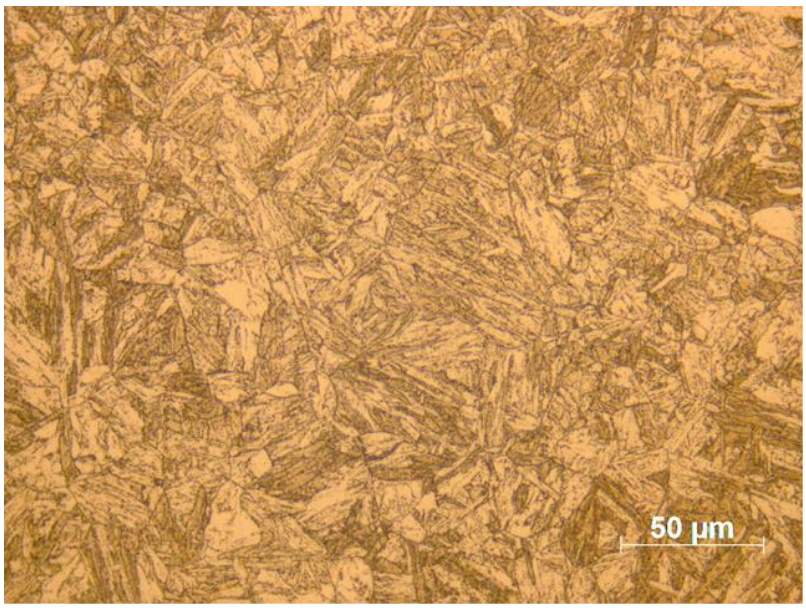


Figure 3.1: Typical microstructure of tested T91 material [33]

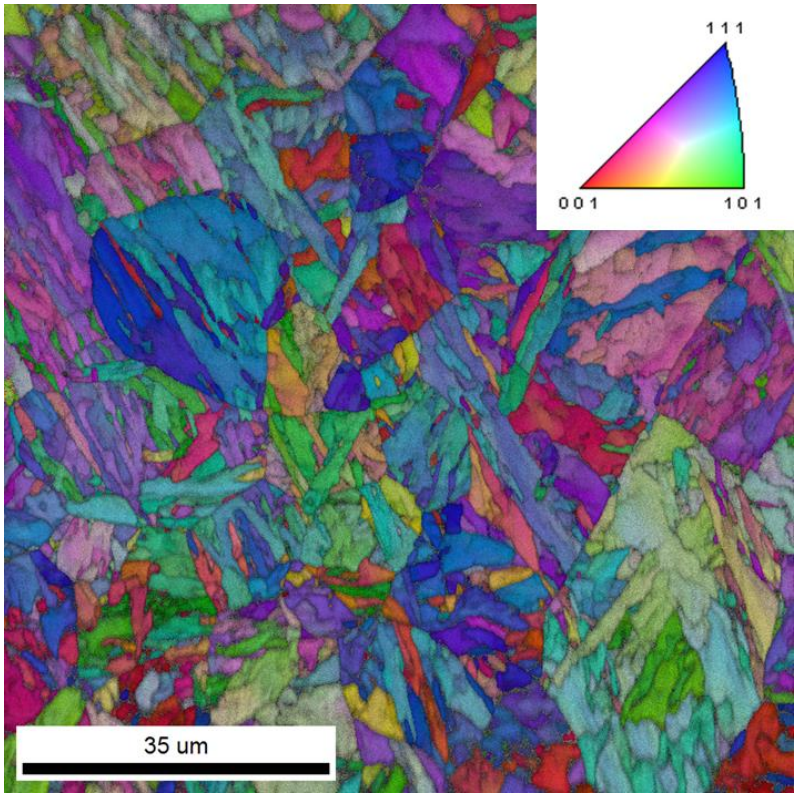


Figure 3.2: EBSD analysis of the as-received T91 material.

### 3.1.2 316L

Conventional austenitic steel 316L (ASTM A240-Ed02) used in the creep tests was produced within the EUROTRANS/ DEMETRA project. The chemical composition of the steel performed by the producing company Industeel, Alcelor group is presented in Table 3.3.

The austenitic stainless steel was delivered as hot rolled and heat treated plates with a thickness of 15 mm. The solution annealing was done at 1050-1100 °C [34] with a goal to reach a homogeneous microstructure as well as a homogeneous distribution of mechanical (strength and elongation) and corrosion compared to the hot rolled 316L [35].

Table 3.3: Chemical composition of austenitic conventional steel 316L delivered within DEMETRA project (wt.%).

| wt.% | Fe | Cr | Mo | Ni | C | Si | Mn | P | S | Al | Cu | Nb | Ti | V | W | N |
|---|---|---|---|---|---|---|---|---|---|---|---|---|---|---|---|---|
| Industeel | Bal. | 16.687 | 2.075 | 10.256 | 0.015 | 0.643 | 1.842 | 0.027 | 0.0028 | 0.010 | 0.080 | 0.079 | 0.004 | 0.202 | - | 0.0480 |

The 316L material was examined metallographically by optical and scanning electron microscopy equipped with energy dispersive X-Ray analysis. Optical micrographs are shown in Figure 3.3 and Figure 3.4. A fully austenitic microstructure interrupted with a small fraction of delta ferrite is evident. The large scale EDS mapping reveals some chemical banding with Ni fluctuation over hundreds of µm at the % level (Figure 3.3b). Furthermore a small number of annealing twins can be identified. In spite of stress relieving heat treatment a secondary phase was found along austenite grain boundaries in the rolling direction ( (Figure 3.3 - Figure 3.5).

Lamellas texture is enriched in Cr and slightly in Mo, as well as depleted in Fe and Ni in comparison to the austenite matrix (Figure 3.5). This is a sign of delta-ferrite formed during the fabrication of the steel.

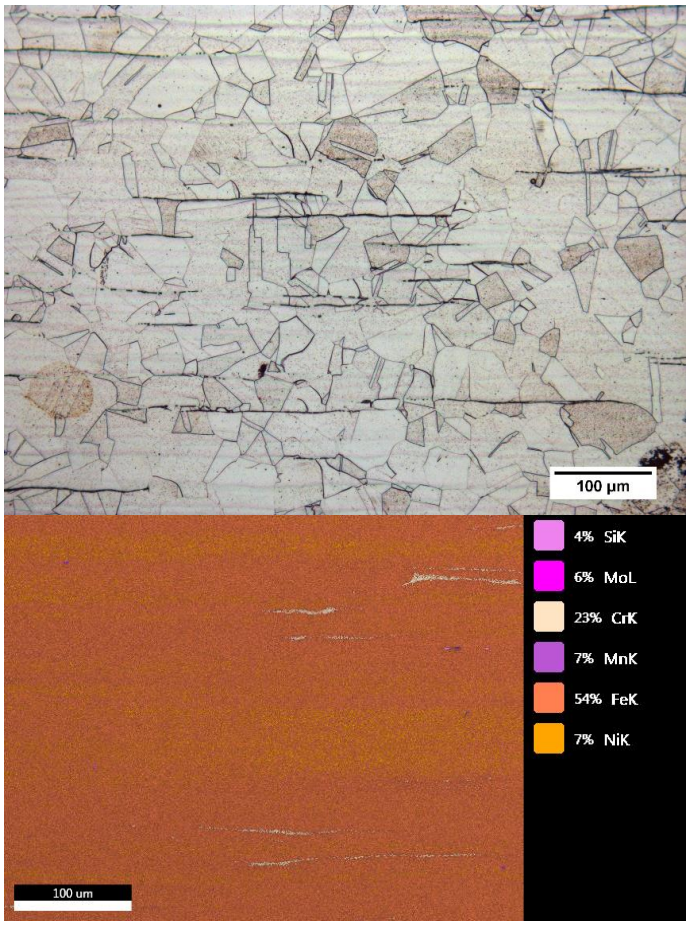


Figure 3.3: (Top) Typical microstructure of the tested 316L material, (Bottom) EDX mapping of a random area of tested 316L material

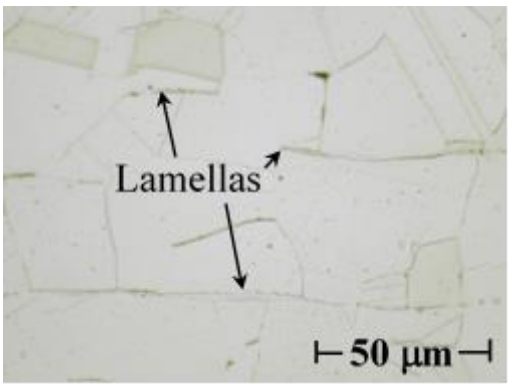


Figure 3.4 Microstructure of 316L in as-received state consisted of austenite grains and δ-ferrite stringers oriented in the rolling direction are marked with arrows.

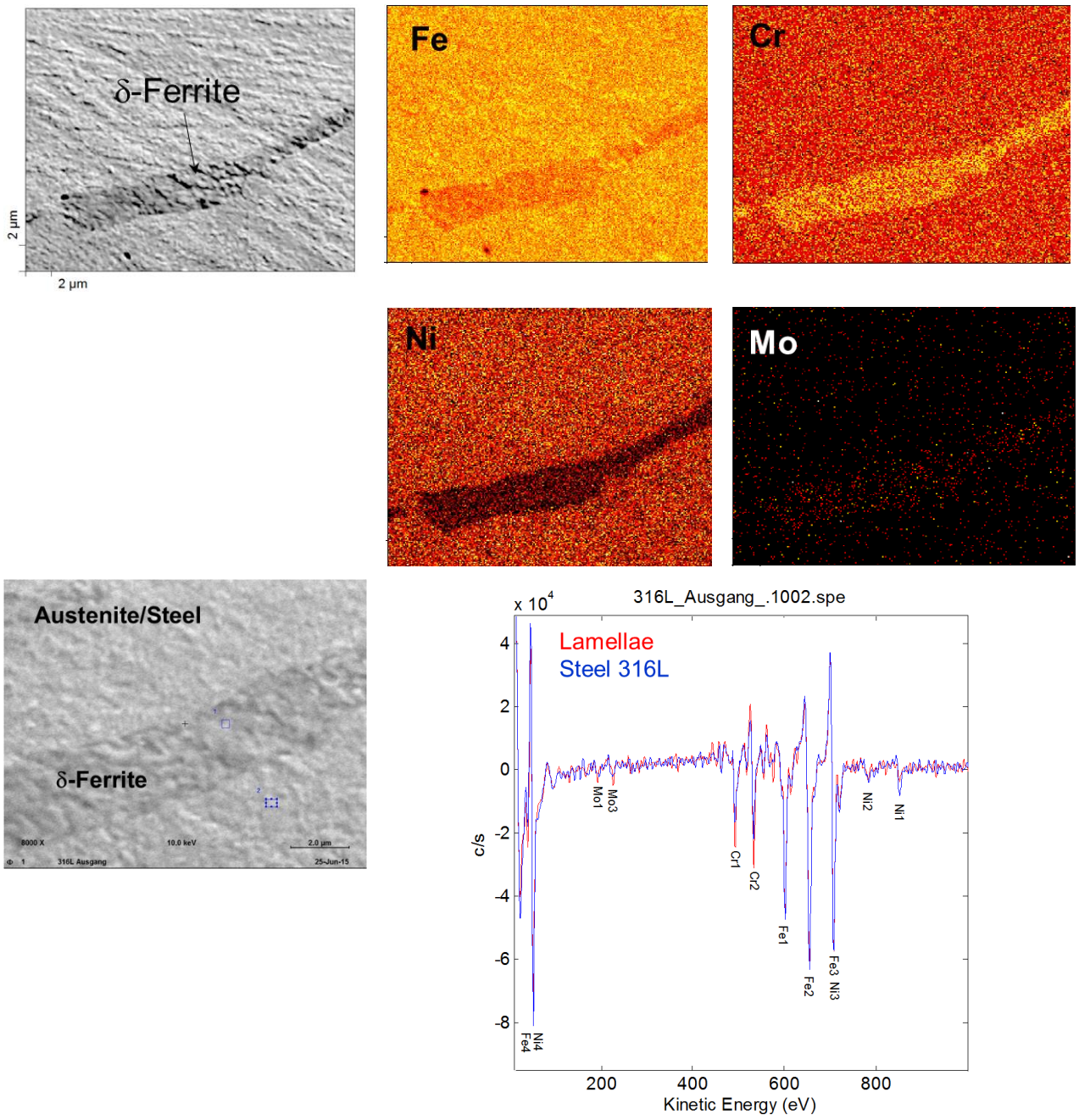


Figure 3.5: SEM/EDX mapping and Auger spectroscopy of 316L in as-received state.

Figure 3.6 shows the results of the conducted EBSD analysis. The same conclusion as given for the light optical investigations can be drawn.

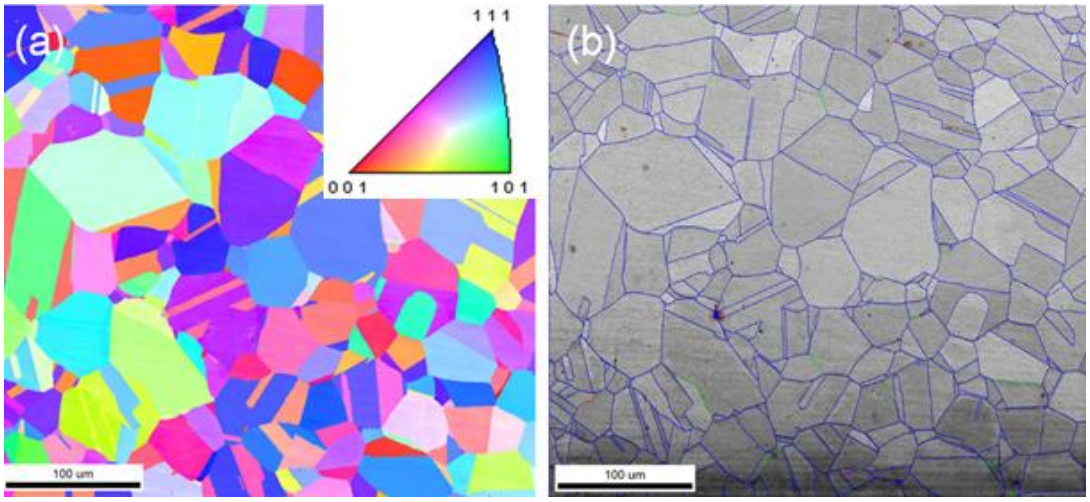


Figure 3.6: EBSD analysis of the tested 316L material

### 3.1.3 15-15Ti

Austenitic 1.4970 steel (also known as 15-15Ti) of nominal composition (wt%) Fe-15.95Cr-15.40Ni-1.49Mn-1.20Mo-0.52Si-0.44Ti was produced by Sandvik. The material was provided in form of a bar which was taken from intermediate step of the thin wall cladding tubes production.

The final step of the treatment for the supplied bar was homogenizing heat treatment at 1200°C for 24 hours, reheating to 1240°C-1260°C and hot forging by hydraulic press. The microstructure of the section from which the specimens were machined had large grains and contained numerous large intergranular Ti-rich precipitates.

Table 3-3: Chemical composition of austenitic steel 1.4970 (wt.%)

| *Lab.* | Fe | Cr | Mo | Ni | C | Si | Mn | P | S | Al | Cu | B | Ti | V | W | N |
|---|---|---|---|---|---|---|---|---|---|---|---|---|---|---|---|---|
| **CVR** | Bal. | 15.95 | 1.20 | 15.40 | 0.1 | 0.52 | 1.49 | <0.01 | 0.0036 | 0.023 | 0.026 | <0.01 | 0.44 | 0.036 | <0.005 | 0.009 |

## 3.2 Fatigue Tests

### 3.2.1 SCK-CEN

Fatigue tests were conducted on LIMETS3 [36] a fatigue testing machine equipped with a hydraulic actuator that applies the forces on the specimen via a metallic bellows. A load cell with a capacity of 15 kN is installed in the load train. Displacement and strains are measured using three extensometers. Large displacements (±25 mm) are measured at the hydraulic actuator, medium displacements (±5 mm) at the grips and strains on the gauge length (±100 µm). The strain is calculated from the displacement of two ceramic knife edges attached to the gauge length. The mechanical extensometer is capable to operate at temperatures limited only by the materials used for its construction and has been specially developed for application in LBE at high temperatures.

Cylindrical specimens with 3.2 mm diameter and 7 mm gauge length were used and the specimen surface was mirror polished using 3 µm diamond paste. A symmetrical push-pull mode with a triangular waveform was

applied. The used strain rate was approximately $4.5 \cdot 10^{-3}$ $s^{-1}$. Reference tests were done in high vacuum conditions ($10^{-5}$ -$10^{-6}$ mbar). Temperature control was done with 2 thermocouples welded to the sample. The maximum allowed temperature difference between the two thermocouples was +/-2.5°C. Cycles to failure (Nf) are defined as the number of cycles until a stress drop of 15% relative to the stress saturation part occurred.

Oxygen measurements above 300 °C were conducted using potentiometric oxygen sensors made of yttria stabilized zirconia as solid electrolyte and $Bi/Bi_2O_3$ as a reference electrode. Ar with 5%$H_2$ was used to control the oxygen content ($C_O$) in LBE. Typically, a $C_O$ of $10^{-5}$-$10^{-6}$ wt%O in LBE is considered as high oxygen conditions and a $C_O$ of $10^{-8}$-$10^{-9}$ wt%O is referred as low oxygen conditions.

### 3.2.2 CNRS

Fatigue specimens were cylindrical with a gauge length of 10 mm and gauge diameter of 6 mm. The gauge part was carefully polished by grinding paper and then by electro-polishing to remove machining defects which could have initiated early cracking.

Low cycle fatigue (LCF) test were performed on a hydraulic fatigue machine of 250kN capacity. Tests were performed under control of total strain. The signal was for most of the tests triangular with a strain rate of $4 .10^{-3}$ $s^{-1}$ or $4. 10^{-4}$ $s^{-1}$, a strain ratio $R_\varepsilon = -1$. Additional tests were also performed using a holding time in tension of 10 minutes. The total strain variation was ranging between $\Delta\varepsilon_t = 0.4\%$ to $\Delta\varepsilon_t = 1.2$ %.

Tests were performed at 350°C in air, oxygen saturated lead-bismuth eutectic (LBE, 45 wt% Pb and 55 wt % Bi) and low oxygen LBE. Additional tests were performed in oxygen saturated LBE at 300°C.

The purification of LBE was performed by an external purification unit by melting LBE and flushing a mixture of Ar-$H_2$ gas. This allowed to decrease the amount of oxygen down to $10^{-7}$ wt % - $10^{-9}$ wt %. Tests in air were performed in ambient environment.

For tests performed in oxygen saturated LBE, the specimen was immersed in a pre-heated liquid LBE bath and then heated at 350 °C till temperature homogenization was obtained. Then the test started and took place without any control on the environment.

For tests performed in low oxygen LBE, the specimen was first immersed in purified LBE and then heated at 350°C till temperature homogenization. The heating and temperature stabilization period was performed inside an environmentally controlled cell isolating from the ambient environment and by flushing Ar- $H_2$ to maintain low oxygen content in LBE. Then the test started under Ar- $H_2$ protection.

For all environments, an induction furnace was employed as heating device.

From LCF tests experiments, are reported:

- The cyclic accommodation, stress amplitude vs number of cycles or stress amplitude vs fatigue life fraction.
- The fatigue life or number of cycles to failure $N_f$ is defined as the number of cycles corresponding to a decrease in tensile stress of 25 %.

## 3.3 Crack Propagation Testing

### 3.3.1 SCK-CEN

Tests were conducted on LIMETS3 [36] (see above). A special extensometer has been constructed to measure the displacements on the crack propagation sample.

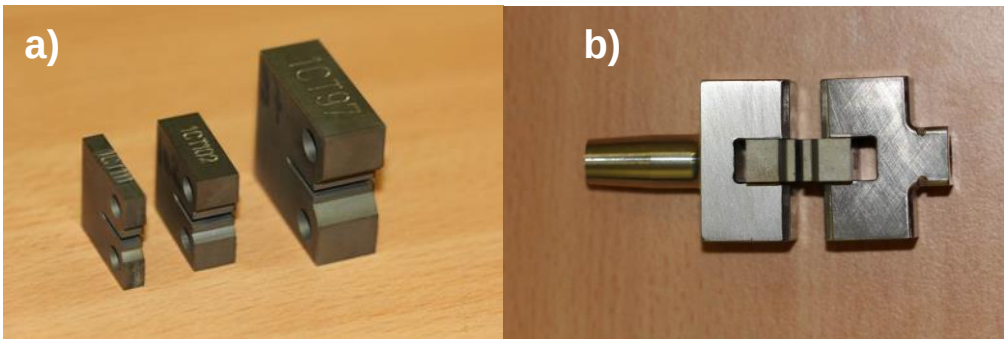


Figure 3.7: a) Different fracture toughness sample geometries and b) sample in the sample holder.

### 3.3.2 CVR

Tests in Centrum vyzkumu Rez (CVR) were carried out in the CALLISTO cell, a vessel containing PbBi (LBE) built on a Zwick/Roell Electromechanical Creep Testing machine, Kappa 50DS (Figure 3.8). CALLISTO is based on the 2-vessel concepts, where the first container is for the preparation of the liquid metal (rough oxygen dosing). The liquid is then transferred to the second preheated tank, containing holders and specimens. The testing frame (Figure 3.9) is common for alignment of all tested specimens.

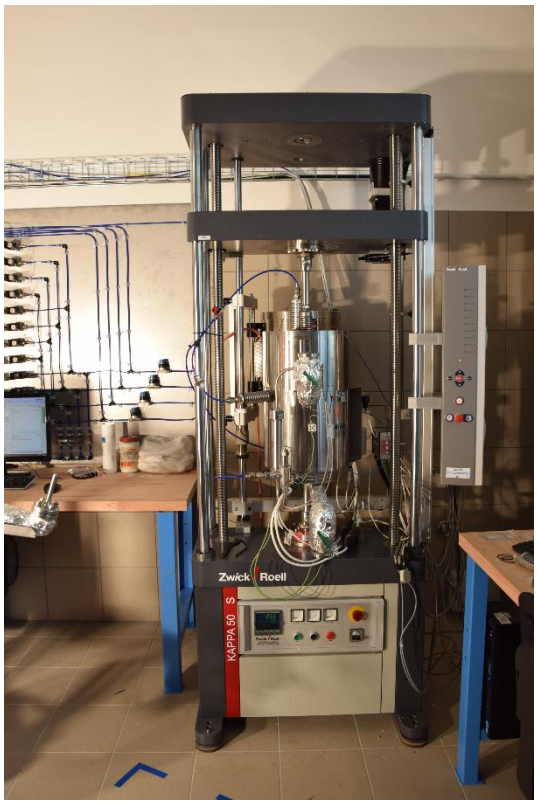


Figure 3.8:Kappa 50DS creep testing machine with CALLISTO cell for testing in HLM.

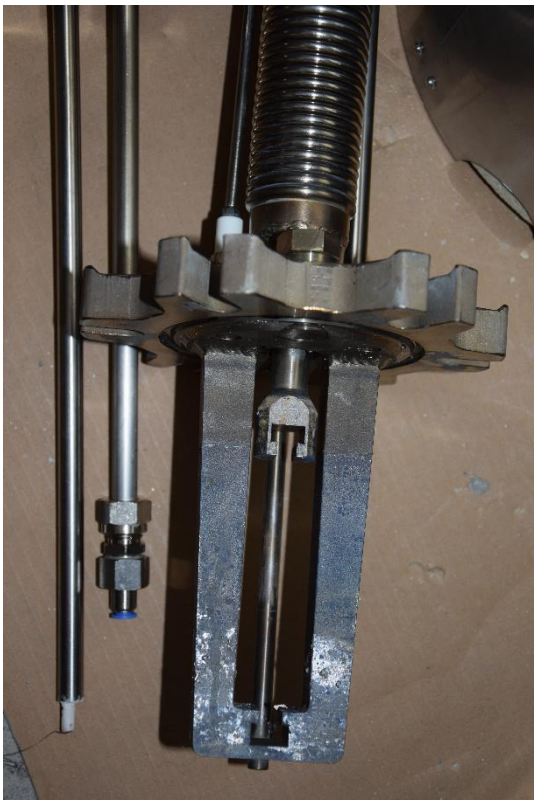

Figure 3.9: Testing frame of CALLISTO cell, common fitting for various adapters.

The testing cell is equipped with oxygen sensors based on the reference $Bi/Bi_2O_3$ inside a YSZ ceramic tube. The oxygen amount in LBE is actively regulated by dosing of hydrogen, which is added as a gas mixture of Ar and $H_2$.

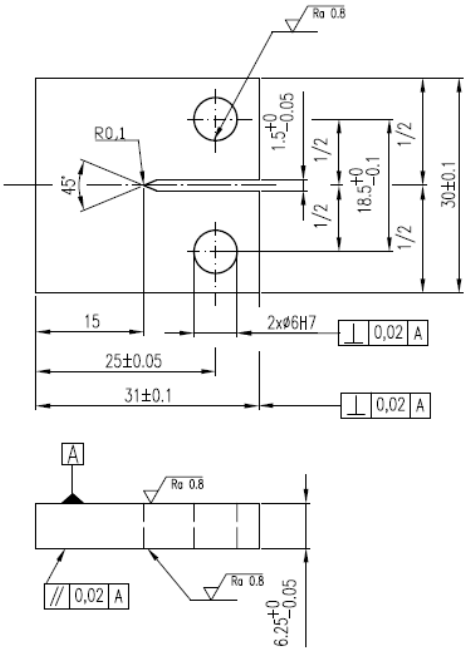


Figure 3.10: 0.5CT specimen with reduced thickness used for FCG tests.

Investigation of fatigue crack propagation was performed on steels T91 and 316L. Fatigue crack growth (FCG) tests were performed on CT specimens (Figure 3.10) in LT direction (longitudinal load and transversal crack growth). Specimens were pre-cracked in air to initial crack ca. 12.5 mm from load line (notch included). The pre-cracking in the air instead of LBE has influence on initial changes of stress intensity factor. The used load control mode (see below) can lead to unstable pre-crack growth. Therefore the propagations with the expected stable crack growth were compared, i.e. without the lower and upper range of stress intensity factor.

It must be taken into account that CALLISTO cells were not equipped with extensometer. Therefore, the crack opening displacement (COD) was evaluated from the testing machine crosshead displacement. A numerical correction was done to achieve more precise result of COD. The correction was verified on three crack growth measurements at room temperature and at 300° C in the air on T91 steel, where standard video extensometer was used for COD measurement. The correction factor takes into account the constant from the machine stiffness and the known initial stiffness of specific specimens. The universal tensile testing machine Z250 (Zwick/Roell), with a laser extensometer, was used to measure the initial specimen stiffness at 300°C. The stiffness (k) of the machine is then evaluated from initial cycles as:

$$1/k_{TOTAL} = 1/k_{SPECIMEN} + 1/k_{MACHINE}$$

The corrections were done for each specimen to avoid errors due to possible differences in specimen fittings. Initial tests were performed in the air with a video extensometer to verify agreement of numerical corrections with COD extensometer measurements.

Tests were performed at constant load instead of constant stress intensity factor, due to the lack of extensometer. The ratio of load asymmetry (R) is 0.1 for all materials.

Following equations were used for FCG evaluation:

Determination of the stress-intensity factor range (ΔK):

$$\Delta K = \frac{\Delta P}{B\sqrt{W}} \frac{(2+\alpha)}{(1-\alpha)^{3/2}} (0.886 + 4.64\alpha - 13.32\alpha^2 + 14.72\alpha^3 - 5.6\alpha^4)$$

where $\alpha = a/W$, P is the applied load, *a* is the crack size, B is the specimen thickness and W is the specimen length.

The crack size was evaluated as a standard function of plane stress elastic compliance for C(T) specimens according to the equation:

$$\alpha = \frac{a}{W} = 1.0010 - 4.6695u_x + 18.460u_x^2 - 236.82u_x^3 + 1214.9u_x^4 - 2143.6u_x^5$$

and

$$u_x = \left\{\left[\frac{EVB}{P}\right]^{\frac{1}{2}} + 1\right\}^{-1}$$

where E is elastic modulus of the sample (at 300 °C in this case) and V is the COD evaluation.

The polynomial was chosen as the best correlation of the cross-head displacement measurement (in load line) and of COD measurement with video extensometer on the front side of the sample (6 mm from the load line). The correction showed COD accuracy ±10 % (i.e. approx. 6 % scaling shift of ΔK at 1000 $Nmm^{-3/2}$).

### 3.3.3 CNRS & SCK-CEN

1/2 CT geometry specimens (W=25 mm, B=12.5 mm) were used in this work to meet the plane-strain condition (Figure 3.11). All specimens were machined in TL orientation where the direction of loading is along the T axis and the direction of crack propagation is along the L axis.

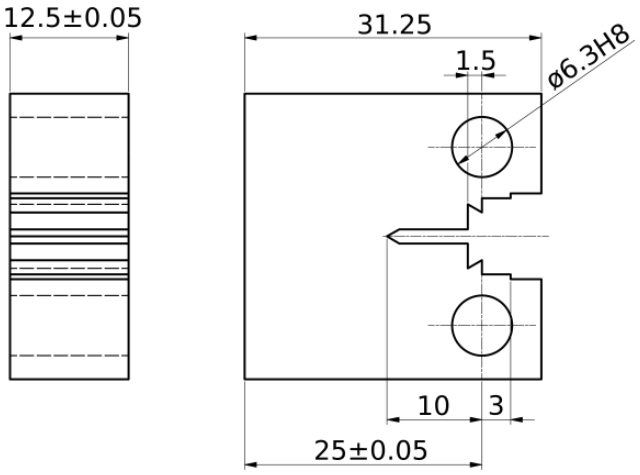


Figure 3.11: Schematic representation of 1/2 compact tension (CT) specimen (dimensions in mm).

Four specimens were used for EBSD and TEM investigations to study the crack paths to help elucidating the crack propagation mechanism in LBE. Sample 1 was pre-cracked in air and tested in Ar-$H_2$ at 350 °C at the displacement rate of 0.2 mm/min. This specimen was used as reference and the other specimens were compared to this one to see how LBE changes the crack propagation in the material. The three other specimens were pre-cracked in LBE at 350 °C at low dissolved oxygen potential to ensure wetting by LBE up to the crack tip so that the right conditions to observe LME could be met prior to testing. Sample 2 was pre-cracked in LBE but not tested, so pre-cracking by fatigue alone could also be examined. Samples 3 and 4 were tested at 350 °C immediately after pre-cracking in the same set-up. Sample 3 was tested at the same displacement rate as Sample 1 (0.2 mm/min) while Sample 4 was tested ten times lower displacement rate (0.02 mm/min). The testing and analysis of the specimens were carried out according to the procedures given in ASTM E 1820 standard. The details of pre-cracking and testing procedures as well as the mechanical analysis of the tests are given elsewhere [37]. The pre-crack lengths, the displacement rates at which each specimen was tested and their elastic-plastic fracture toughness values ($J_Q$) are given in Table 3.4.

Table 3-4: Displacement rates, pre-crack lengths and $J_Q$ values of each specimen

| Sample id | Pre-cracking environment | Test environment | Displacement rate (mm/min) | $a_0$ (mm) | $J_Q$ (kJ/m$^2$) |
|---|---|---|---|---|---|
| Sample 1 | Air | Ar-$H_2$ | 0.2 | 11.2 | 454 |
| Sample 2 | LBE | N/A | N/A | 14 | N/A |
| Sample 3 | LBE | LBE | 0.2 | 13 | 48 |
| Sample 4 | LBE | LBE | 0.02 | 12.7 | 41 |

All specimens were broken in liquid nitrogen as a last step. Since sample 2 was only pre-cracked, the pre-crack length could be read out directly from the fracture surface covered with LBE. For the three other samples, the pre-crack-length was measured by careful analysis of a change in the fracture surface. One can note the great drop of the fracture toughness induced by LBE (a factor of ten) that indicates that plain strain test conditions are extremely damaging.

## 3.4 Crack Initiation

### 3.4.1 CVR

Specimens were loaded in the CALLISTO cell in LBE environment at 300 °C on a Zwick/Roell Electromechanical Creep Testing machine, Kappa 50DS (see above).

Investigation of crack initiation was performed on steels T91 (specimen designation T), 15-15Ti (specimen designation I) and 316L (specimen designation L). Slow Strain Rate Tests (SSRT) were performed on tapered specimens (Figure 3.12) in longitudinal direction. Flat tapered specimens [38] were monotonic tensile loaded in the CALLISTO cell. Tests were performed mostly at a constant displacement rate 0.0012 mm/min (related to the narrowest cross-section area strain rate of $10^{-6}$ $s^{-1}$) and in different environments – air as a reference and LBE with various oxygen amounts.

Different surface manufacturing was used for the sample to see the surface influence on crack initiation. Tapered sides were as received from EDM (electric discharge machining). Flat sides were manufactured differently – one side was ground with 600 SiC paper and the other side was polished with 1 μm diamond suspension.

The tapered shape leads to a stress distribution over the length of the sample with the highest stress in the smallest cross section. The narrowest part is taken as an initial area for stain rate and UTS evaluation, however the tapered shape leads to increasing of the initial cross-section area approximately about 50 % (top part of the specimen), which leads to increasing of theoretical strain rate about 20 %. Tests were performed up to rupture or UTS to monitor and evaluate different effects on crack initiation and distribution.

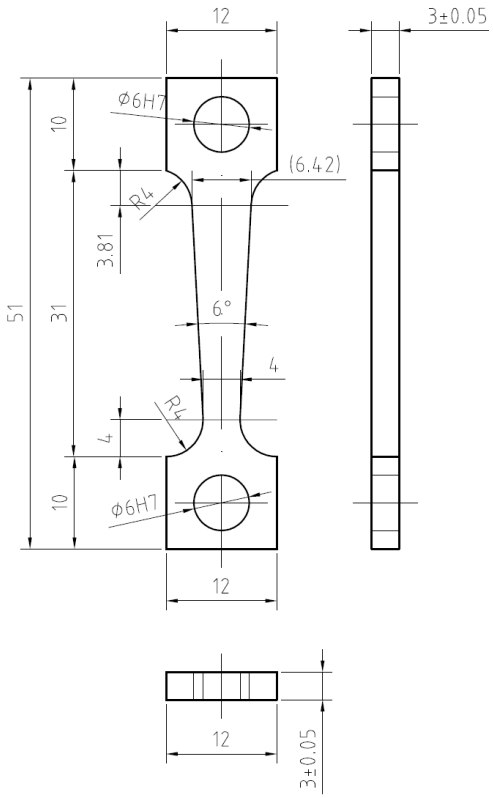


Figure 3.12: SSRT tapered specimen for crack initiation investigation.

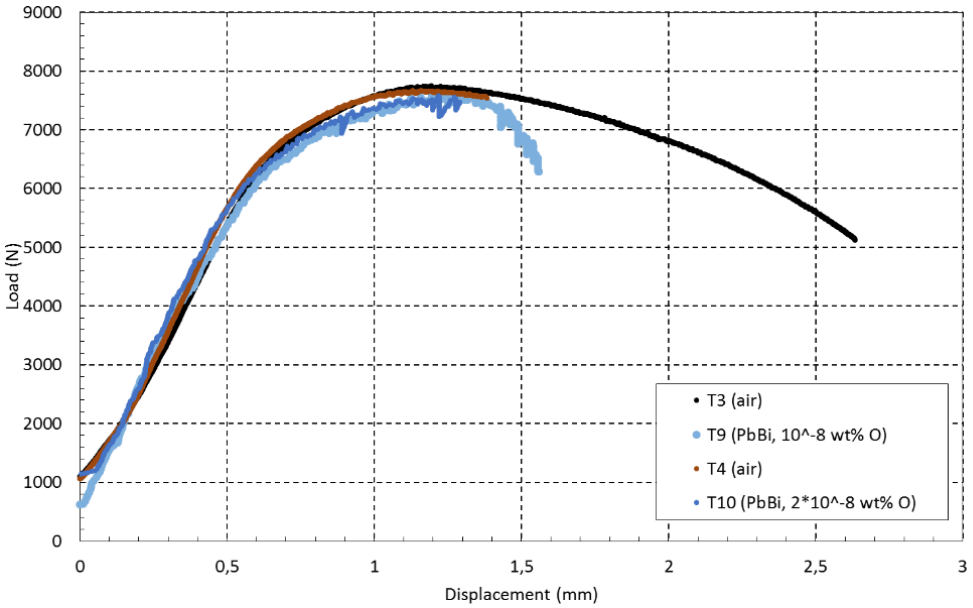


Figure 3.13: Comparing plots of T91 at 300 °C up to rupture and up to UTS.

Figures in chapter 4 will showing materials plots are separate for UTS-end and for rupture to have better overview about results. Figure 3.13 shows several examples for the obtained load displacement curves documenting the good repeatability of the material tests up to UTS.

Table 3-5: SSRT matrix of tapered specimens in CVR.

| Sample ID | Environment | oxygen wt% | T °C | strain rate $s^{-1}$ | Test stop |
|---|---|---|---|---|---|
| T1 | LBE | $6 \cdot 10^{-6}$ | 300 | $10^{-6}$ | rupture |
| T2 | air | - | 23 | $10^{-6}$ | rupture |
| T3 | air | - | 300 | $10^{-6}$ | rupture |
| T4 | air | - | 300 | $10^{-6}$ | UTS |
| T5 | LBE | $5 \cdot 10^{-8}$ | 300 | $10^{-6}$ | before UTS |
| T6 | Ar | - | 300 | $10^{-6}$ | rupture |
| T7 | Ar | - | 300 | $10^{-6}$ | UTS |
| T8 | LBE | $3 \cdot 10^{-13}$ | 300 | $10^{-6}$ | rupture |
| T9 | LBE | $10^{-8}$ | 300 | $10^{-6}$ | rupture |
| T10 | LBE | $2 \cdot 10^{-8}$ | 300 | $10^{-6}$ | UTS |
| T11 | LBE | $3 \cdot 10^{-7}$ | 300 | $10^{-4}$ | UTS |
| T12 | LBE | $3 \cdot 10^{-7}$ | 300 | $10^{-6}$ | rupture |
| I1 | air | - | 23 | $10^{-6}$ | rupture |
| I2 | air | - | 300 | $10^{-6}$ | rupture |
| I3 | air | - | 300 | $10^{-6}$ | UTS |
| I4 | LBE | $5 \cdot 10^{-8}$ | 300 | $10^{-6}$ | UTS |
| I5 | LBE | $4 \cdot 10^{-8}$ | 300 | $10^{-6}$ | UTS |
| I6 | LBE | $10^{-9}$ to $10^{-8}$ | 300 | $10^{-6}$ | rupture |
| L1 | air | - | 23 | $10^{-6}$ | failure |
| L2 | LBE | $3 \cdot 10^{-8}$ | 300 | $10^{-6}$ | rupture |
| L3 | air | - | 300 | $10^{-6}$ | rupture |
| L4 | air | - | 300 | $10^{-6}$ | UTS |
| L5 | LBE | $10^{-8}$ to $10^{-5}$ | 300 | $10^{-6}$ | UTS |
| L6 | LBE | $10^{-12}$ to $10^{-11}$ | 300 | $10^{-6}$ | rupture |
| L7 | LBE | $3 \cdot 10^{-12}$ | 300 | $10^{-6}$ | UTS |
| L8 | LBE | $5 \cdot 10^{-8}$ | 300 | $10^{-4}$ | UTS |

## 3.5 Creep Tests

The effect of lead and LBE on the creep properties of 316L is extremely limited [37]. Therefore, in this study creep strength of the 316L stainless steel was investigated in liquid oxygen-controlled LBE at 450-550°C in comparison to air. According to theoretical data, the surface of the steel at $10^{-6}$ wt% oxygen dissolved in LBE is expected to form an oxide scale. The oxide scale has to prevent steel elements dissolution and liquid metal attack and, therefore, any significant changes in time-to-rupture in comparison to the steel tested in air was expected, similar to creep behavior of the ferritic/martensitic steel T91 in Pb or LBE and air at elevated temperatures [38]. To study the effect of liquid LBE on 316L stainless steel, the oxygen content in liquid metal was specified to be decreased as low as possible.

Specimens employed in the creep-to-rupture tests conform to DIN EN ISO 204:2009. Figure 3.14 presents the basic geometry of the specimen. The creep-to-rupture specimens were cut from the plates in the rolling direction by electric discharge machining. The surface of the gauge section was finished by turning. Finally, the surface of the specimens was cleaned with acetone.

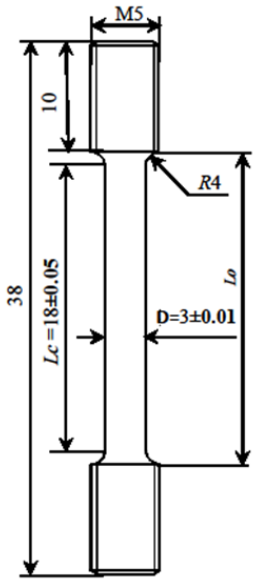


Figure 3.14: Workshop drawing of the employed specimens from 316L.

The dimension measurements of the creep specimen in their as-received state and after creep test were done by means of a laser scanner with a spatial resolutions of 0.1 mm and 1 µm for the length and gauge diameter, respectively. The measured initial diameter *D*, length *Lc* and length *Lo* were used to determine sampling length $L_r$, strain $\varepsilon_r$ and strain at rupture $\varepsilon_R$ according to DIN EN ISO 204:2009:

$$L_r = Lc + 2\sum_i [(D/d_i)^{2n} l_i)], \quad (1)$$

where n is the stress exponent in Norton's law of the material tested and equal of 5 for conventional steels. $l_i$ is the length increment with diameter along the curved transition from the gauge to the head of the specimen.

$$\varepsilon_r /\% = \Delta L / L_r \times 100, \quad (2)$$

$$\varepsilon_R /\% = \Delta L_r^R / L_r \times 100, \quad (3)$$

where $\Delta L_r^R$ is the elongation of the gauge length $L_r$ determined as a difference between $L_r$ before and after the test (at rupture). Reduction of load-bearing cross-section or necking, *Z*, is determined for each ruptured specimen by measuring diameter of the gauge diameter *D* before (*Do*) and after the tests (at rupture) ($D_R$):

$$Z /\% = (Do - D_R)/Do \times 100. \quad (4)$$

In spite of the fact that the ground austenitic steel surface transformed into ferrite during the test at elevated temperatures in LBE, the necking of the ruptured specimen can be determined with a laser scanner, since the ferrite is thick and brittle enough to split from the steel around fracture.

The CRISLA facility provides eight rigs for creep-to-rupture testing at elevated temperature (up to 650°C), three for testing in air and five for testing in liquid lead alloys. Each rig consists of a steel container (capsule) that encloses the specimen in the respective environment, and an external system for imposing a static tensile load (Figure 3.15). A pull rod conducted through the lid of the capsule forms the connection between the external loading system and the specimen, and simultaneously transmits the deformation of the specimen to two displacement transducers residing outside the capsule. The movement of the pull rod is accommodated by flexible bellows. The lever arm that is connected to the pull rod (and to a weight pan on the opposite end) has a load-strain factor of ten, which was verified for each system using a load cell. The results differed by 2%

using the same load frame and the different lids for experiments in air and lead including the impact of the bellows etc. The measurements of all test stands resulted in difference of 7% in the load factor and showed good reproducibility. The same lid was used for all experiments with lead.

The capsules for the tests in air and LBE are made of 17–12 Cr–Ni steel (DIN W.-Nr. 1.4571). The temperature inside the capsule is controlled via heating sleeves and monitored using a NiCr–Ni thermocouple residing close to the specimen. Measuring the temperature profile at 650°C in the capsule for tests in air showed variations 650±1°C along the gauge length of the specimen. Due to higher thermal conductivity of lead alloys in comparison to air the temperature gradient along the gauge length in lead alloys is expected to be less than ±1°C compared to the one determined in air. The maximum temperature deviation at the center of the specimens was ±1°C at 450-550°C for all experiments performed.

A distinctive feature of the capsules used for the tests in lead containing alloys (Pb, LBE) is the equipment for oxygen control, including an oxygen sensor and a gas supply (Figure 3.15a,c). Additionally, the inner surface and internals of these capsules are provided with an aluminide coating (FeAl), so as to minimize Ni dissolution from the austenitic construction material.

In a separate test, the coated steel was exposed to stagnant Pb for 2015 h, showing local cracking and oxidation inside the FeAl protection layer. Optical inspection of the inner surface of the capsules between experiments revealed only few degraded spots with acceptable corrosion. The capsules for tests in lead alloys contain approximately 9 kg (900 ml) of the liquid metal. The volume of the capsules for tests in stagnant air is smaller (appr. 230 ml).

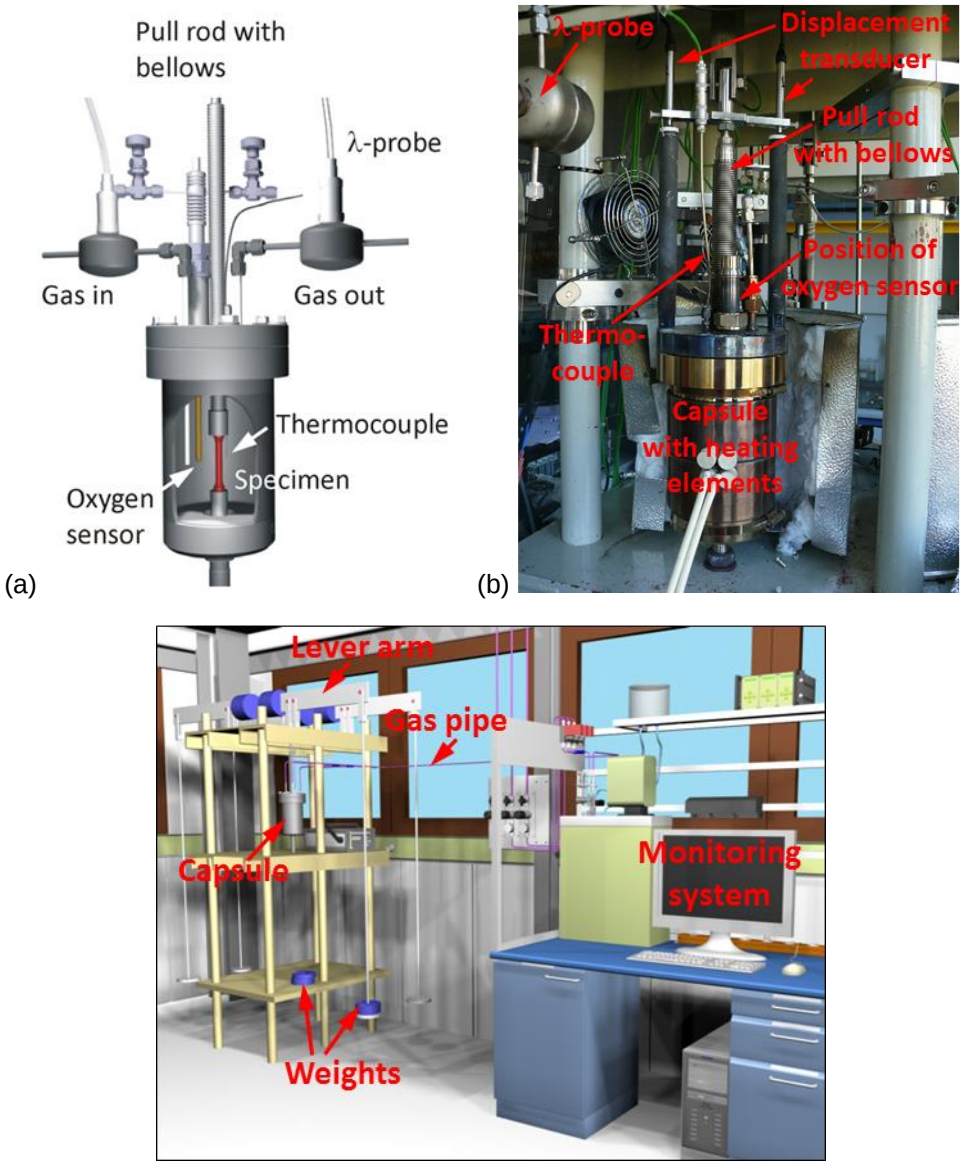


Figure 3.15: CRISLA-capsule for creep tests in heavy liquid metal (a, b) and CRISLA facility inclusive peripheral devices (c).

Elongation of the specimen is measured in-situ outside the capsule by means of two displacement transducers. The transducers are positioned on two rods with a ceramic slice on the top and fixed stable to the pull rod, so that two elongation curves are measured on two opposite sides of the specimen. It is worth noticing that the connector of both displacement transducers has to be perpendicular to the lever arm. Determining the actual strain, the average of two measured elongation values measured in-situ was used.

The specimens were tested in stagnant oxygen-controlled lead-bismuth eutectic (LBE) in the CRISLA facility at 550, 500 and 450°C and 300, 325 and 375 MPa, respectively. The test matrix is presented in Table 3-6. An oxygen activity measured in LBE at every temperature with an oxygen sensor in-situ corresponds low oxygen concentration presented in Table 3-6 as well. Reduction of oxygen concentration was reached by permanently introducing 100 ml/min and Ar-$H_2$ gas mixture during the whole creep-to-rupture tests. Reference experiments at all test temperatures started simultaneously with the tests in LBE and were carried out in air. To find an effect of oxygen concentration in LBE on the creep properties, three creep-to-rupture tests were done in LBE at $c_o=10^{-6}$ wt% and 550 °C.

Low oxygen concentration in LBE was reached by pre-conditioning of the liquid metal without the specimen inside the capsule. Before the specimen was mounted, the oxygen sensor output had to reach 1 V at the test temperature. To be sure that a low concentration could be expected everywhere in the capsule at the moment when the creep test started, further introduction of 100 ml/min Ar-5%$H_2$ gas in LBE was done during a few (up

to 12) hours. Once the specimen was mounted and the temperature reached the test temperature, the specimen was loaded. Ar-5%$H_2$ gas was introduced during the whole creep-to-rupture tests. In case of constant oxygen concentration ($c_o$=$10^{-6}$ wt%), the target oxygen sensor output had to be reached during preconditioning without the specimen and held at this concentration and test temperature for some hours before the specimen was mounted. The specimen was loaded as soon as the test temperature was reached.

Oxygen sensor output (E / V) and temperature were measured with a Pt/O oxygen sensor and NiCr-Ni thermocouple (T / K), respectively, close to the center of the specimen (Figure 3.15a) as well as an oxygen concentration in LBE calculated using Eq. (94) from [39]:

$$\log c_o = -3.2837 + \frac{6949.8}{T} - 10.080 \times \frac{E}{T} \quad (5)$$

Test conditions are presented in Figure 3.16 to Figure 3.19.

Table 3-6: Test matrix for the stainless steel 316L.

| Experiments | Status |
|---|---|
| LBE, $c_o = 10^{-9}$–$10^{-10}$ wt%, 550 °C/ 300 MPa | $t_R$ =1,060 h |
| LBE, $c_o = 10^{-6}$ wt%, 550 °C/ 300 MPa | $t_R$ = 182 h, 231 h, 365 h |
| Air, 550 °C/ 300 MPa | Stopped before rupture, $t_R$ > 1,150 h |
| LBE, $c_o = 10^{-8}$–$10^{-9}$ wt%, 500 °C/ 325 MPa | $t_R$ =5,025 h |
| Air: 500 °C / 325 MPa | Test is still running, $t_R$ > 10,000 h |
| LBE, $c_o$ =$10^{-9}$–$10^{-10}$ wt%, 450 °C/ 375 MPa | Test is still running, $t_R$ > 4,630 h |
| Air, 450 °C/ 375 MPa | Test is still running, $t_R$ > 3,265 h |

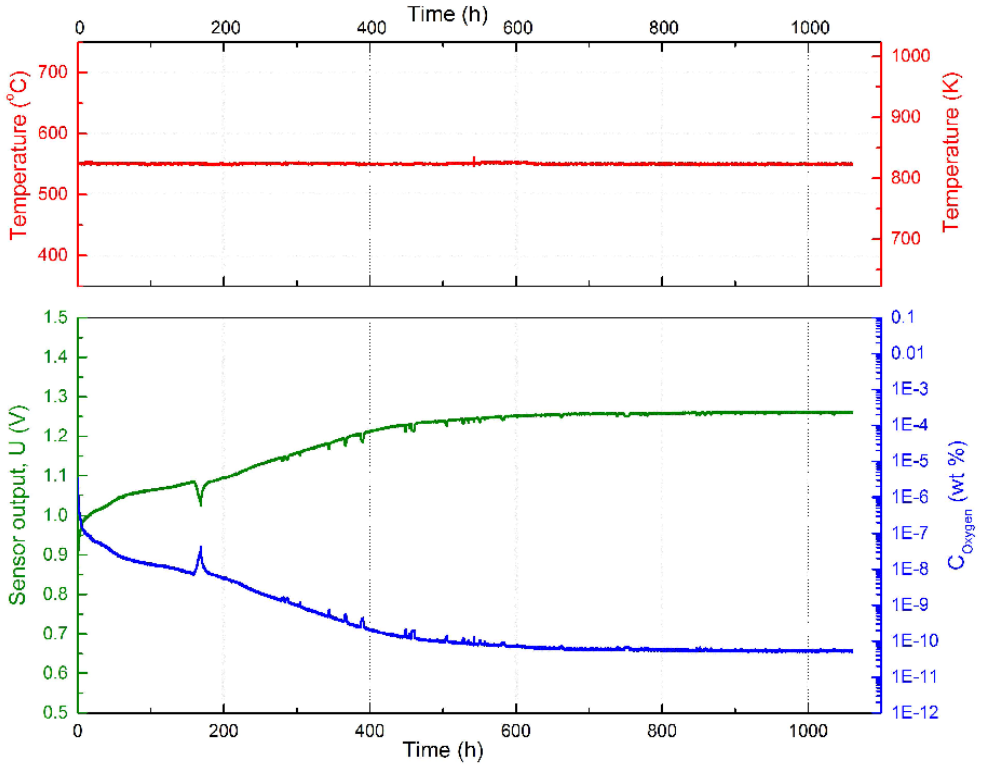


Figure 3.16: Test conditions – temperature of LBE, oxygen activity and oxygen concentration during the creep-to-rupture test with 316L at 550°C.

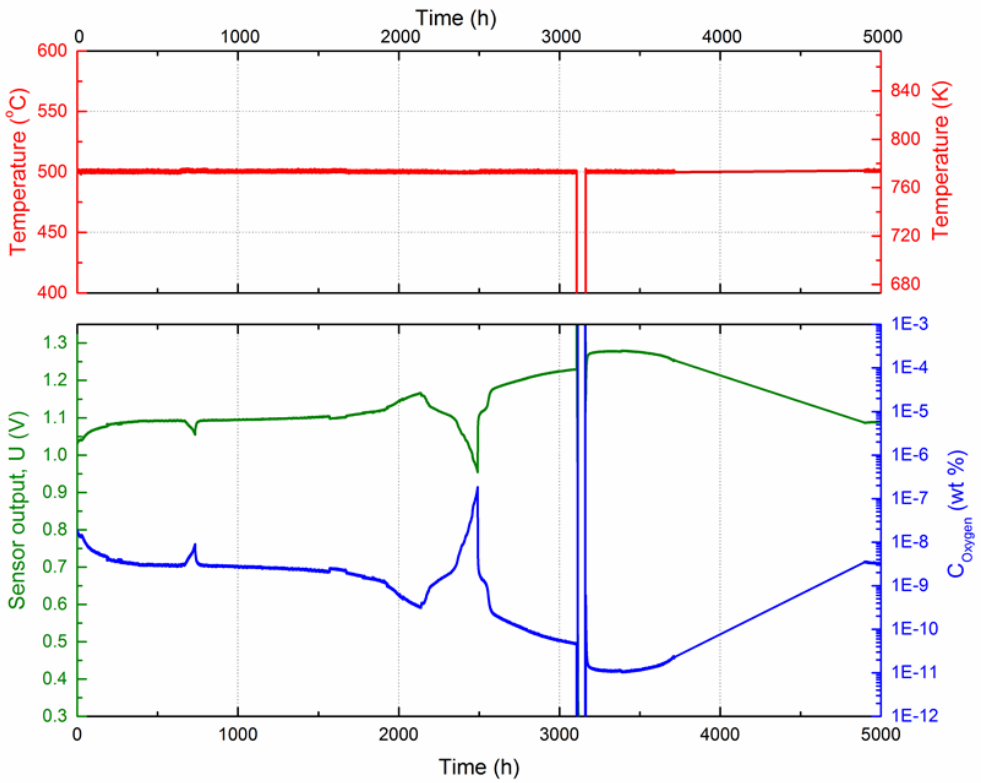


Figure 3.17: Test conditions – temperature of LBE, oxygen activity and oxygen concentration during the creep-to-rupture test with 316L at 500°C.

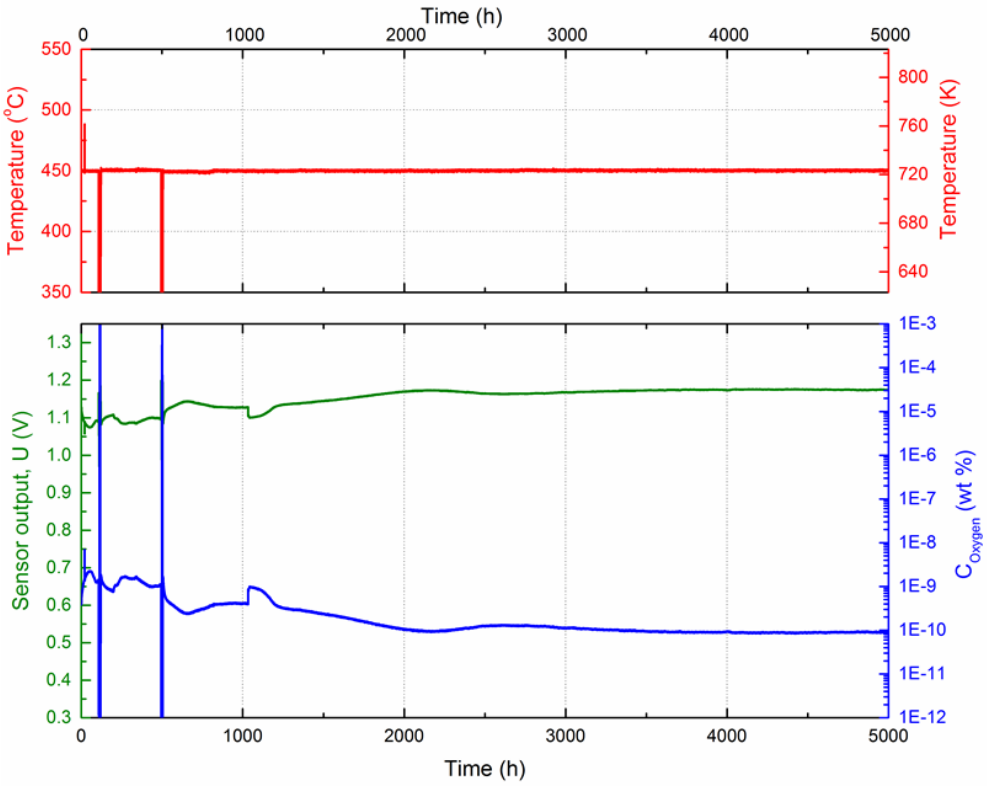


Figure 3.18: Test conditions – temperature of LBE, oxygen activity and oxygen concentration during the creep-to-rupture test with 316L at 450°C.

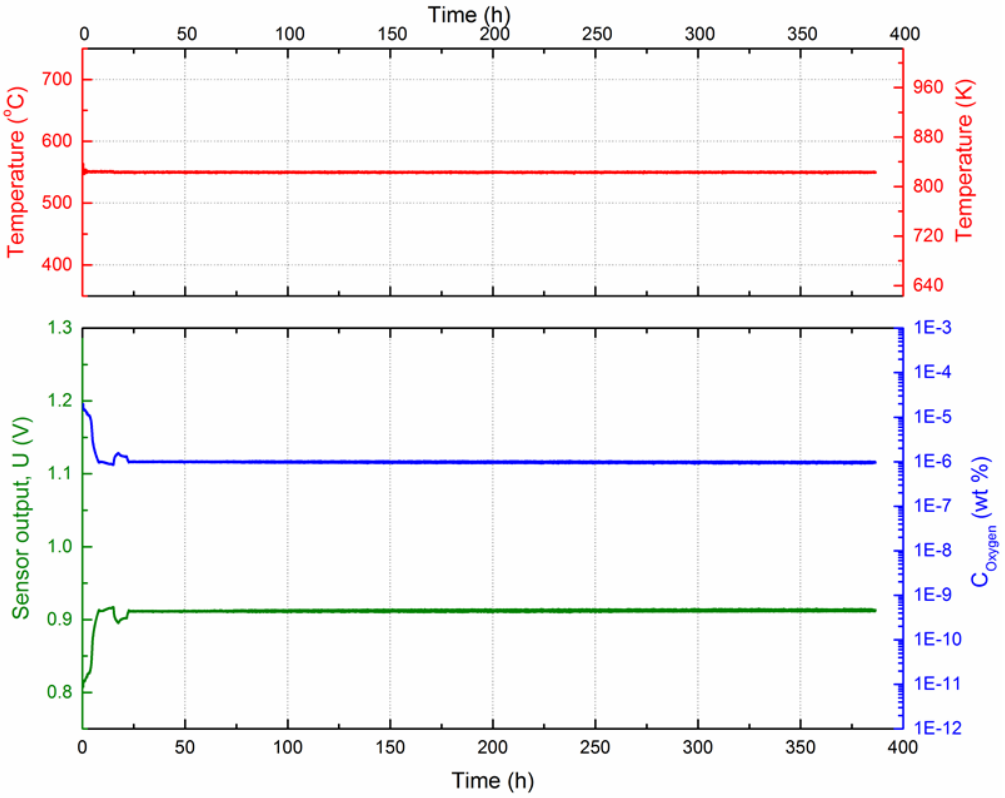


Figure 3.19: Test conditions – temperature of LBE, oxygen activity and oxygen concentration during the creep-to-rupture test with 316L at 550°C and co=$10^{-6}$ wt%.

As soon as the oxygen concentration co was around $10^{-6}$ wt% the creep-to-rupture test at 550°C was started. $c_o$ reached $10^{-10}$ wt% after 300 h test and remained at this value until the specimen ruptured. During the test at 500°C the temperature was sharply decreased after approximately 3,050 h because of technical problem. Starting with $10^{-8}$ wt% an oxygen concentration of $10^{-11}$ wt% was reached after about 3,100 h and increased again up to $c_o=5x10^{-9}$ wt% to the end of the test (after at 5000 h). The dissolved oxygen concentration in LBE at 450°C had a tendency to decrease from $10^{-9}$ till $10^{-10}$ wt% during first 2000 h. Example of a stable oxygen concentration and temperature for one from three creep-to-rupture tests at $c_o=10^{-6}$ wt% and 550°C is presented in Figure 3.19.

**Check of oxygen sensor function stability.**

An electrochemical oxygen sensor used in the tests works with a platinum (Pt)/air reference electrode, i.e., a stainless steel wire with a platinized tip residing in air. The solid electrolyte consists of stabilized zirconia, which is in the form of a tube that is closed at one end (1 in Figure 3.20). The sensor head is provided with an adaptor for a bayonet-nut-connector (BNC, 4 in Figure 3.20), via which the sensor output is transmitted to a voltmeter. The sensor head is additionally equipped with two open tubes (3 in Figure 3.20), in order to facilitate the ingress of air into the electrolyte tube. The oxygen content in the gas that leaves the capsule is qualitatively monitored using a λ-probe in the exhaust gas line.

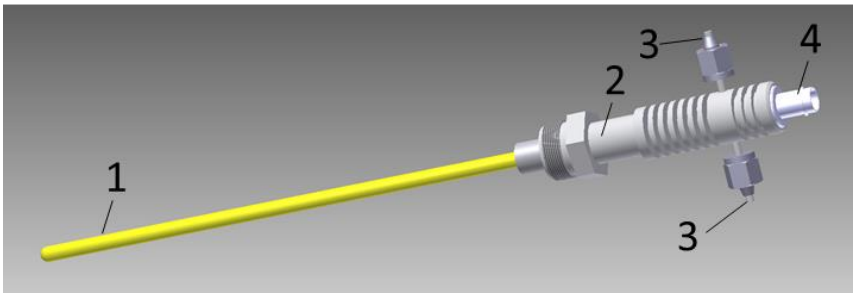


Figure 3.20: Visible components of the Pt/air electrochemical oxygen sensor: 1 - stabilized zirconia tube and stainless steel wire with platinum tip inside the zirconia tube; 2 - stainless steel housing; 3 - gas (air) apply; 4 – adapter for BNC plug.

The tendency to reduce time-to-rupture, $t_R$ in LBE at 550°C and $c_o=10^{-6}$ wt% in comparison to air as well as to dissolve of Ni and Cr from the steel surface by a direct contact to liquid metal were unexpected. Therefore, two additional replicates tests in LBE at $c_o=10^{-6}$ wt% and check-up of sensor functionality were additionally carry out. The testing of an oxygen sensor that was fresh built-in into the CRISLA-capsule for the experiment in LBE at $c_o=10^{-6}$ wt% and 550 °C was carried out just after the experiment. The sensor was introduced into the liquid metal with a following heating of the capsule up to 550 °C. During this time, Ar-$H_2$ of 100 ml/min was permanently introduced into the upper part of the capsule above LBE (Pre-conditioning stage in Figure 3.21). As soon as the oxygen sensor output was approaching to 1 V, Ar-$H_2$ gas was changed on 100 ml/min Ar of nominal purity ≥99.9999% (Ar 6.0). This resulted in decrease of the oxygen sensor output. Following addition of 50 ml/min Ar and up to 5 ml/min air for about 275 h allowed approximating the oxygen output to Pb/PbO equilibrium (Figure 3.22) due to saturation of the heavy liquid metal with an oxygen. Even adding Ar-$H_2$ afterwards for more than 25 h did not change the oxygen sensor output (Figure 3.21) and it remains close to Pb/PbO equilibrium. The observed deviation between the output of the sensor and theoretical expectation remains lower than 5 mV after following 375 h and is within the margin admissible for passing the test.

The oxygen sensor has shown stability of the voltage output that corresponds to PbO formation during long term of introducing of air and oxygen containing Ar into LBE at the constant elevated temperature. An approaching of the measured oxygen sensor output and the theoretical value of lead oxide formation allows us to be virtually certain that the oxygen sensor used by constant oxygen concentration in liquid metal $co=10^{-6}$ wt% displayed a real voltage before its functionality test as well.

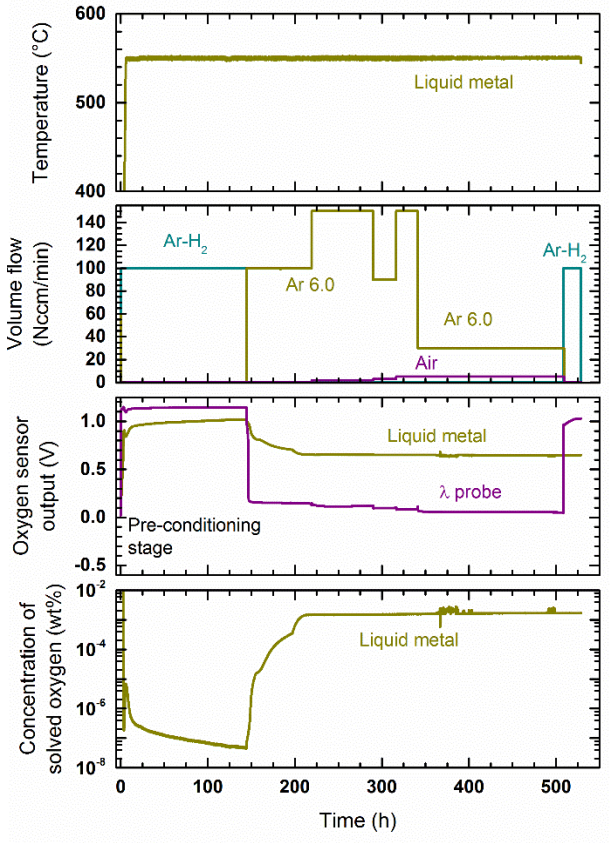


Figure 3.21: Functionality test of the oxygen Pt/air sensor in CRISLA equipment after the creep-to-rupture test with 316L in LBE at $c_o=10^{-6}$ wt%, 550 °C and 300 MPa.

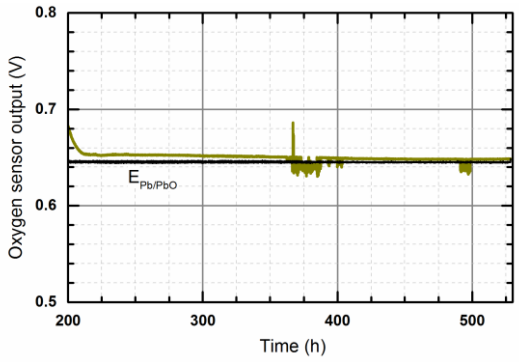


Figure 3.22: Comparison of oxygen sensor output with expectation for the temperature-dependent Pb/PbO equilibrium as a function of time during the test of the sensor.

## 3.6 Microstructural investigations and fractography

### 3.6.1 SCK-CEN

For light microscopy samples ground with SiC paper up to a grit size of 2000 followed by polishing steps up to 1µm diamond polish were investigated. TEM samples were prepared by either electro-polishing or using a focused ion beam microscope. Electro-polished samples were first mechanically polished to about 80 µm thickness followed by electrolytic thinning at -50 °C and 20 V using a double jet polisher from Struers.

EBSD samples were ground using SiC grinding papers in the order of P800, P1200, P2000 and P4000. Subsequently, the samples were polished using two diamond pastes: 3 microns for 3 min and 1 micron for 5 to 8 min. As final step OPS (colloidal silica in suspension) solution containing 40 nm silicon oxides was used to achieve the proper surface quality. For the SEM analysis a FEI Nova 600 Nanolab dualbeam FIB was used.

LBE residues on fracture surfaces were chemically removed with a solution consisting of $CH_3COOH$, $CH_3CH_2OH$ and $H_2O_2$ in a volume ratio of 1:1:1. SEM investigations of the cleaned fracture surfaces were conducted using a Jeol, JSM6610LV microscope. High resolution fractographic micrographs were taken using a FEI Helios Nanolab 650 SEM/FIB instrument. The fracture surface was further examined by AFM using a Digital Instruments Dimension 3100 microscope operated in tapping mode.

### 3.6.2 CNRS

The scanning electron microscopy (SEM) observations were conducted at an accelerating voltage of 20 kV on a FEI Quanta 400 tungsten SEM for fractographic observations. Additional investigation for microstructure evolution was performed in a JEOL JSM-7800F LV fitted with an EDS (Energy Dispersive X-ray Spectroscopy) and an EBSD (electron backscatter diffraction, AZtec) detectors from Oxford Instrument.

For EBSD analysis of the CT specimens, smaller samples from the crack propagation surfaces were cut in the LS direction from samples 1, 2 and 3. A sample with dimensions 6x8x2 mm was cut from each specimen by Secotom-10 cutting machine. They were embedded in Presi KM-U cold resin (covering the fracture surface) and ground down to leave a thickness of about 300 µm between the fracture surface and the flat ground back side. After grinding, the resin was dissolved by immersion in acetone assisted with ultra-sonic exposure. The samples released from resin were then glued to a thin sheet of steel and put in a JEOL cross section polishing machine (JEOL Cross-Polisher) for ion milling. The polisher uses an argon beam to mill a cross section of the sample which is under the protection of a mask except for the milled part. They were ion milled along the LS plane therefore perpendicularly to the fracture surface. Milling proceeded from the back of the fracture surface so that edges of the cross section remained sharp. 7-8 hours of ion milling were performed on each sample which resulted in an EBSD ready surface finish up to the fracture surface. A Leo 1530 FEG SEM operating at 15 kV was used to observe the ion milled surfaces and determine the regions of interest. An EDAX OIM data acquisition system was used for EBSD measurement and the TSL OIM 7 software was used for the analysis.

Starting from the notch each specimenss fracture surface has in the following order, a precracked area, a crack propagation area (sample 2 excluded) and the remaining area broken in liquid nitrogen. The EBSD ready area of sample 1 was milled in the part of the specimen that was broken in liquid nitrogen after testing in air. This gave the opportunity to study the low temperature brittle fracture mode of the steel to compare with the brittle fracture induced by LBE. Sample 2 was prepared for EBSD in the area of pre-cracking by fatigue in LBE. Sample 3 was prepared for EBSD in the area of crack propagation in liquid LBE. Sample 2 and sample 3 still had their fracture surface covered with LBE which was then protected from potential manipulation damage and eased imaging (LBE appears in white contrast in Back Scattered Electron (BSE) mode imaging, see Figure 3.23).

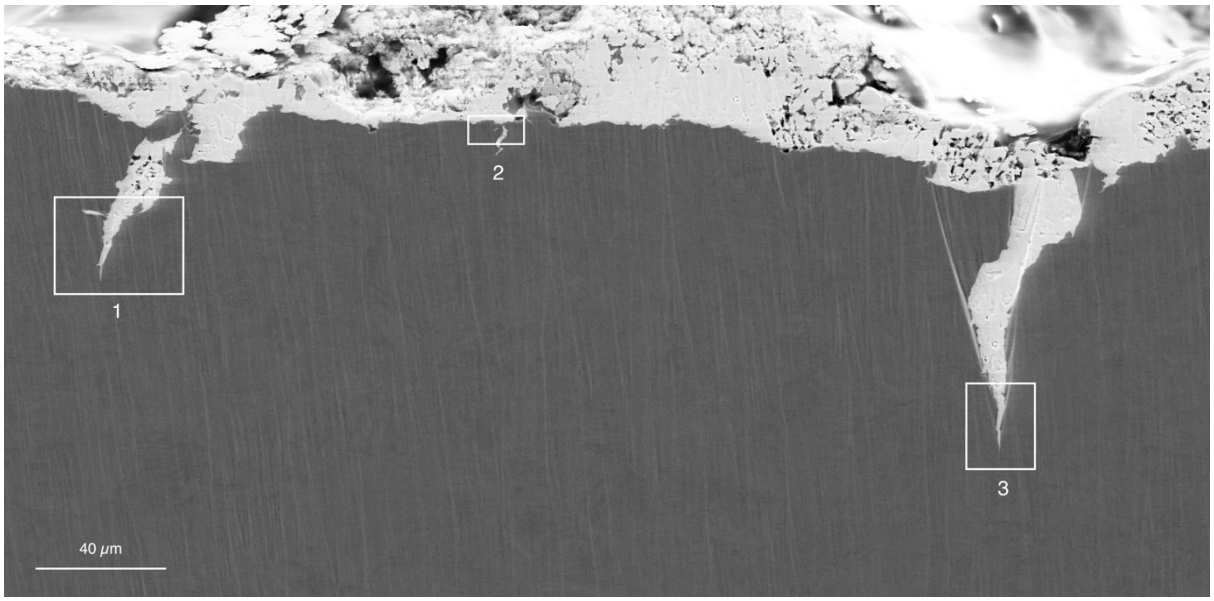


Figure 3.23: BSE view of the cut from Sample 3 with the areas analyzed by EBSD

The transverse cuts revealed several secondary cracks that were analyzed by EBSD (areas 1, 2 and 3 in Figure 3.23 for sample 3). When possible, the steel microstructure was mapped up to the fracture surface by EBSD (e.g. area 2 in Figure 3.23).

The TEM lamella was extracted from sample 4 using a FEI Dual Beam HELIOS Nanolab 650. The fracture surface shows unambiguously an aspect change between the area fractured in LBE and the one fractured in liquid nitrogen. In addition, some LBE still covers part of the surface and the final crack front can be imaged using backscattered electron imaging. The extraction area was selected before the final crack front in LBE in an area typical of crack propagation in LBE (located approximately at the center of Figure 3.24a) but with a low coverage of LBE. The cut was made perpendicularly to a surface step and included a portion of the flat surfaces aside (see Figure 3.24b).

a) b)

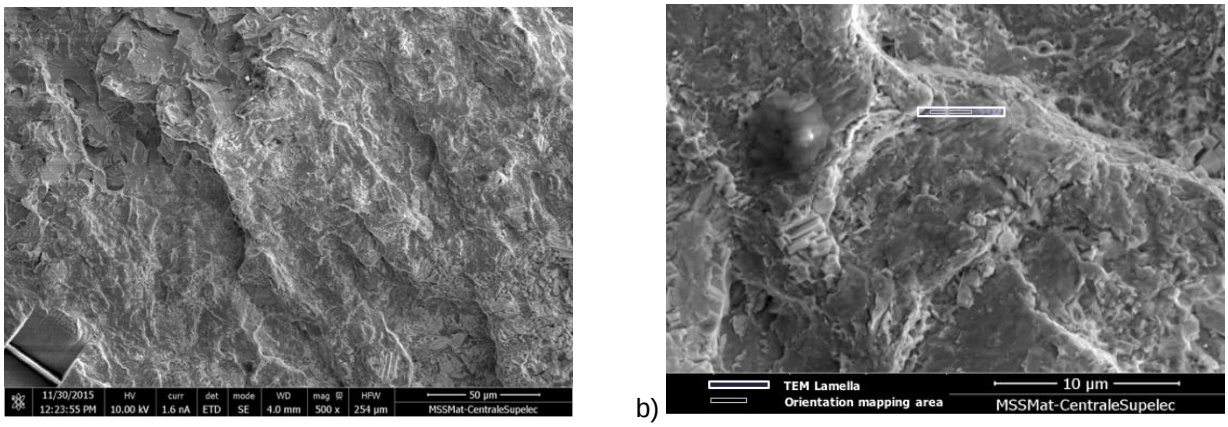


Figure 3.24: SEM view of the area from Sample 4 selected for FIB sampling a) general view of the fractured area for FIB sampling (notice the fracture surface in liquid nitrogen at the top left) b) detailed view of the area of FIB sampling with the step and the rectangular shape deciphering the area under investigation

The lift out technique was used to machine the TEM lamella in a similar manner than the technique used in [42]. A protective platinum line was deposited over the surface of interest. Two trenches were then milled on both sides of the platinum line using 30kV $Ga^+$ FIB. A U-cut was made and the sample was lifted out and attached on a TEM grid by Pt deposit. Then lower Gallium ions current down to 80 pA were used to thin the lamella to electron transparency with minimum surface artefacts. TEM imaging and orientation mapping was carried out with a Tecnai F20 operated at 200 kV equipped with the precession automated crystal orientation mapping (ACOM-TEM) [43]. Precession was turned on with an angle of 0.5°. The crystal orientation mapping measurements were made with a step varying from 3 to 10 nm. Three phases were included (ferrite, $M_{23}C_6$ carbide and amorphous). The mapping was carried out around arrested secondary cracks and in areas immediately below the fracture surface of the main crack.

### 3.6.3 KIT

Modifications in the microstructure of the austenitic stainless steel 316L affected by elevated temperature and surrounding corrosive medium were studied by comparing the steel in its as-received and post-test states. Longitudinal and vertical polished cross-sections provided from the specimens before and after the creep-to-rupture test, steel surface contacted to LBE during the test and fracture surface were examined after the tests using light optical microscopy (LOM) and scanning electron microscopy (SEM) supplemented by EDX. Auger spectroscopy was used for the study of 316L steel in as-received state as it was presented in chapter 3.1.

Loss of material, thickness of the ferrite layer and depth of local dissolution attack were measured with a Keyence VHX-600 digital microscope, so that the quantitative outcome of the interaction of 316L with oxygen-containing stagnant LBE can be characterized. A vertical circular polished cross-section of the specimens was evaluated with respect to the percentage of surface affected by dissolution. The thickness of the ferritic layer as well as material loss are measured turning a vertical cross-section of the specimen after the creep-to-rupture test around every 15° from 0 till 165°.

### 3.6.4 CVR

Fracture surfaces were cleaned from LBE with a mixture of $C_2H_6O+H_2O_2+CH_3COOH$ (1:1:1). After exposure, the specimens were analyzed in a TESCAN Mira 3 - FEG SEM with Oxford Instruments EDX detector (Parameters of each SEM observation are highlighted in the figures for each specific specimen).

# 4 Results

## 4.1 Fatigue Tests

### 4.1.1 Fatigue Tests at SCK-CEN

Figure 4.1 shows a comparison of LCF test results for samples tested in vacuum and low oxygen containing LBE. As can be seen from the figure the fatigue life of samples exposed to LBE is remarkably decreased. A factor of 7 to 9 can be found for high strain amplitudes while at lower strain amplitudes this factor decreases to about 3.

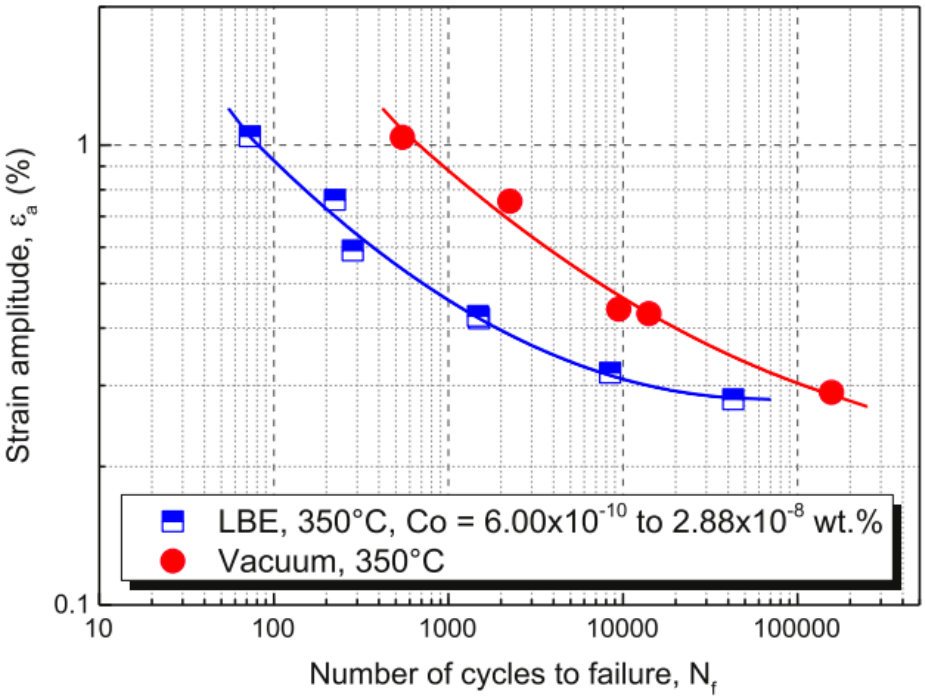


Figure 4.1: Comparison of the fatigue lives for T91 tested in vacuum and tested in LBE [33].

In order to identify the influence of temperature on the fatigue behavior of T91 in LBE tests at different temperatures and environment were conducted. Figure 4.2 shows the cyclic stress response of T91 as function of temperature in different environments. The given stress amplitude is the average of tensile peak stress and compressive peak stress (Δσ/2) at each cycle. Independent of the environment all cyclic stress curves show a similar principle behavior; cyclic softening during the first three cycles followed by stress stabilization in the following few cycles followed by continuous cyclic softening until sample failure. As it can be seen from Figure 4.2 the fatigue endurance in vacuum is not strongly dependent on the temperature. In contrast to this a significant influence of temperature can be found for the fatigue endurance in LBE environment. Here a factor of eight in the difference in fatigue life can be found. The shortest fatigue life was found for 350 °C. Between 160 and 350°°C the fatigue life decreases with increasing temperature while it increases again when the temperature is further increased.

Indirectly the influence of temperature on crack propagation can be described by plotting the number of cycles between the initiation of a macroscopic crack and failure of the samples ($N_f$-$N_{a)}$ over temperature (Figure 4.3). As can be seen from Figure 4.3 $N_f$-$N_a$ increases linearly with temperature for tests in vacuum. This indicates that crack propagation slows down with increasing temperature. In contrast to vacuum the material behaves different in LBE. Here a shallow trough can be found with its minimum (i.e fastest crack propagation) at about 350 °C. The factor between maximum and minimum $N_f$-$N_a$ in LBE is about 2. Nevertheless, the curve of tests in LBE shows significantly lower $N_f$-$N_a$ values indicating highly accelerated fatigue crack propagation in the presence of LBE compared to vacuum.

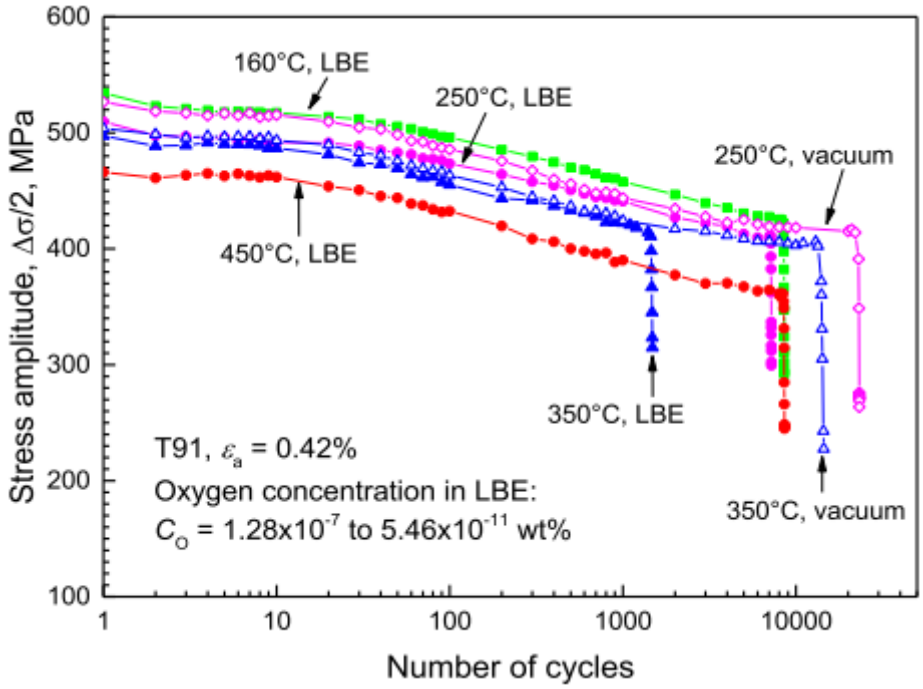


Figure 4.2: Cyclic stress response of T91 as function of temperature tested in LBE and vacuum [44].

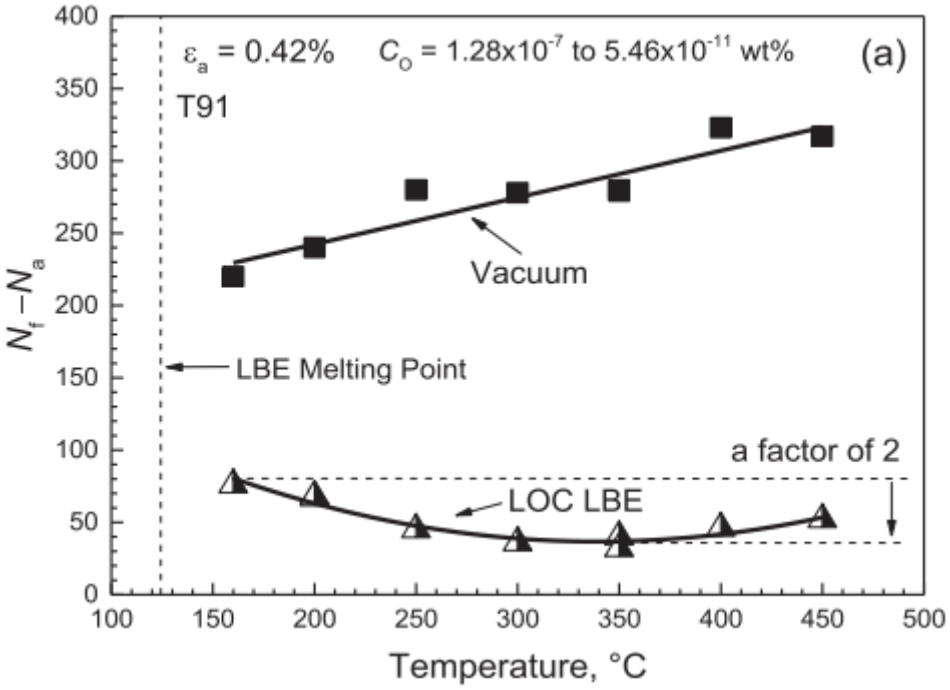


Figure 4.3: Effect of temperature on Nf-Na illustrating the temperature influence on fatigue crack propagation [44].

In Figure 4.4 and Figure 4.5 fracture surfaces of T91 steel after testing in LBE are shown. The fracture surfaces of the LBE embrittled material show different fracture features typical for so called quasi brittle fracture (Figure 4.4a) as well as tear ridges. Tear ridges are marked with arrows in Figure 4.4a. More detailed investigations show that the tear ridges are covered with micro-dimples (micro/nano-mounds and valleys) Figure 4.4b,c. Occasionally also larger ductile dimples can be found Figure 4.4d. On prior austenite grain boundaries, it is also possible to identify the aforementioned nano-dimples. An example is given in Figure 4.4e. Nevertheless, despite these ductile features the main fracture appearance is brittle as can be seen from the featureless regions as well as small secondary cracks in Figure 4.5a and b. A closer view on the secondary cracks in Figure 4.5c gives the impression that the small secondary cracks follow the direction of martensite laths. Investigation of the featureless regions at very high magnification (Figure 4.5d-f) reveals that these regions

are also not completely flat but covered with nano-dimples. Nevertheless, not all featureless regions show nano-dimples as can be seen from the example given in Figure 4.6. In order to clarify the differences between quasi-brittle fracture, as it is typical for liquid metal embrittlement, and cleavage fracture high resolution SEM investigation were also conducted on specimen broken in liquid nitrogen. The fracture morphology of such a sample can be found in Figure 4.7. River patterns and featureless regions are evident and even at very high magnification Figure 4.7b no nano-dimples can be identified.

In order to confirm the SEM observation complimentary atomic force microscopy investigations were conducted. The topographic images for fracture surfaces created in liquid $N_2$ and fatigue fracture surfaces generated in the presence of LBE can be found in Figure 4.8. Similar to the SEM observation no nano-dimples can be found for the sample broken in liquid nitrogen. For the fracture surface tested in LBE a highly undulated surface can be found. Width and depth of these undulations can be estimated with 20-30 nm and 1-3 nm respectively.

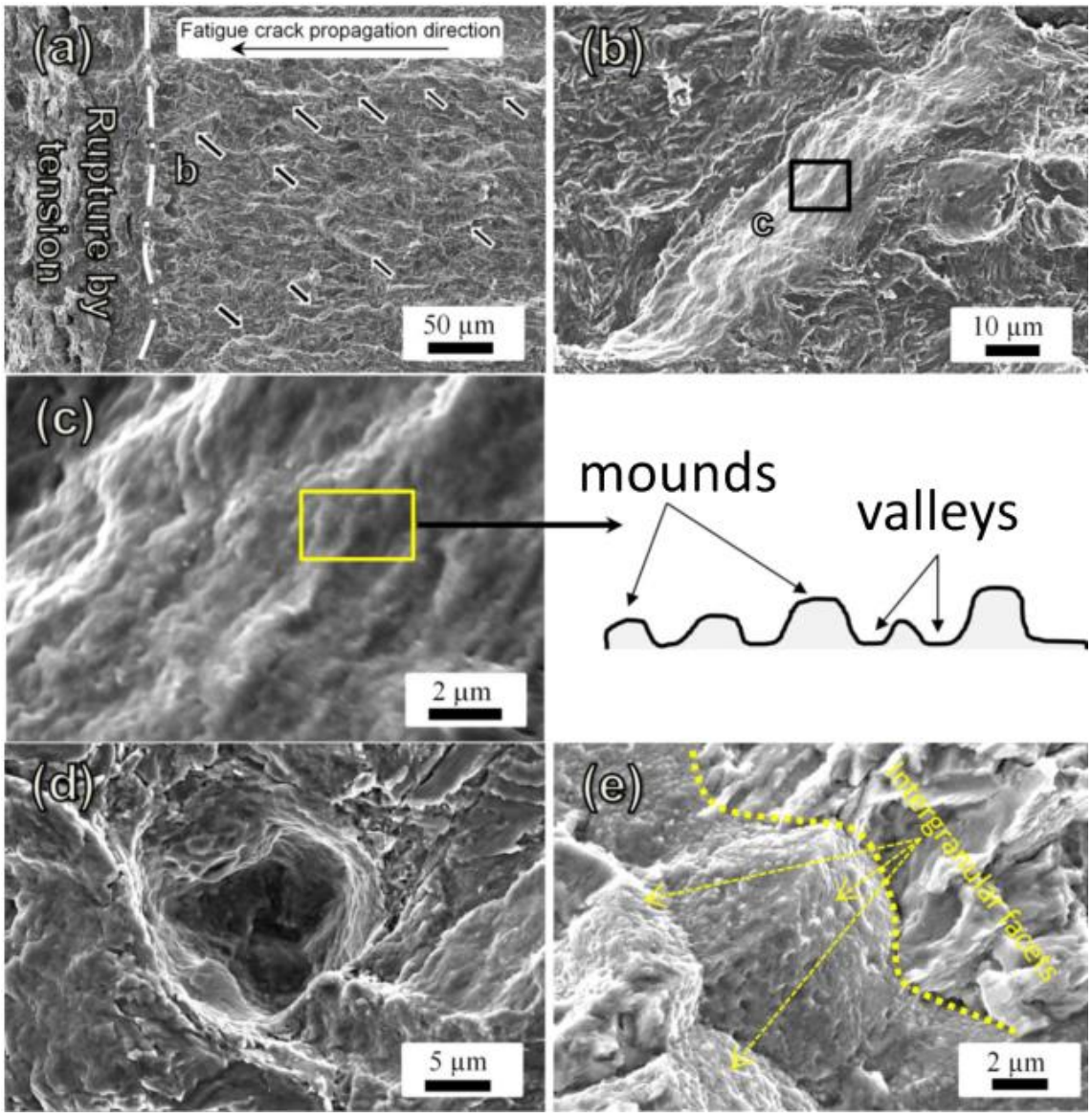


Figure 4.4: SEM fractographic micrographs show a typical quasi-brittle fracture surface after testing in LBE, covered by many tear ridges (a and b) on which submicron “mounds/valleys” are present (c); A large dimple with a size of 15 µm can be observed as well (d); Many submicron “mounds/valleys” are present on the intergranular facets (e). The T91 specimen in (a–d) was tested under the conditions: T = 350 °C, $\varepsilon_a$ = 0.76 %, $C_O = 5.8 \times 10^{-9}$ wt.%; The T91 specimen in (e) was tested at 160 ◦C, $\varepsilon_a$ = 0.43 %, $C_O = 3.80 \times 10^{-9}$ wt.% [45].

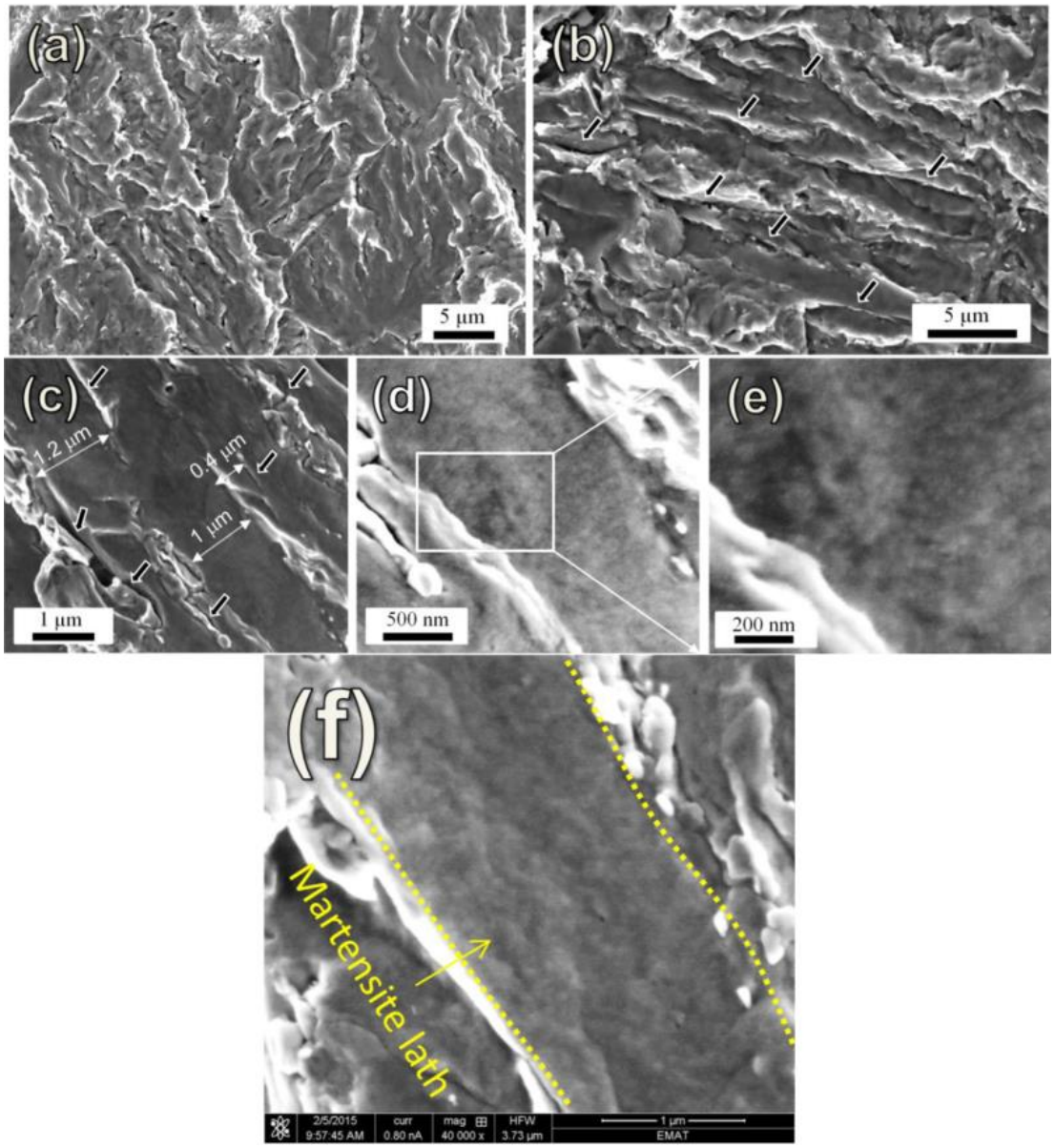


Figure 4.5: High resolution SEM fractographic micrographs showing very rough fracture surface after testing in LBE, characterized by numerous tiny secondary cracks and flat "featureless" regions (a and b); The tiny secondary cracks seem to propagate along the martensite lath boundaries (b and c); The flat regions are not perfectly featureless but are covered by a large number of nano "mounds/valleys" (d–f). The arrows indicate the positions of the secondary cracks. The T91 specimen in (a) was tested under the conditions: T = 350 °C, $\varepsilon_a$ = 0.59%, $C_O = 2.88 \times 10^{-8}$ wt.%; The T91 specimen in (b–f) was tested under the conditions: T = 350 °C, $\varepsilon_a$ = 0.76%, $CO = 5.8 \times 10^{-9}$ wt.% [45].

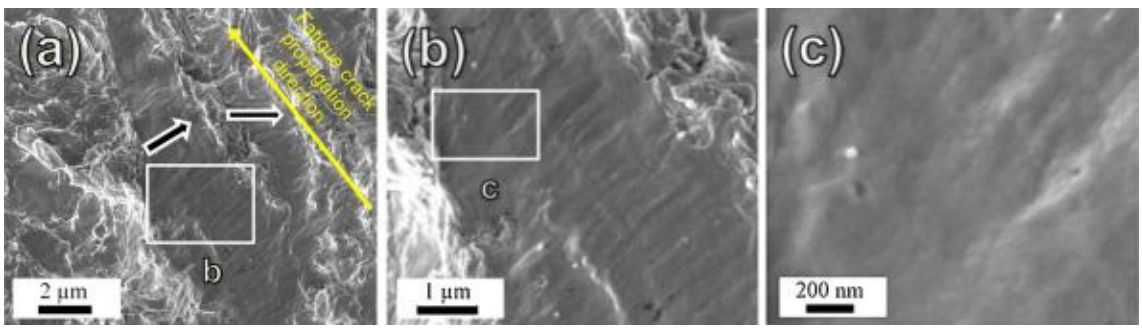


Figure 4.6: High resolution SEM fractographic micrographs of the LME fracture surface showing that the flat regions do not have as evident nanoscale dimples as those shown in Fig. 4e. The SEM pictures were taken under a tilt angle to show the relative position of two adjacent flat regions, as indicated by the two arrows (a). More details at the flat regions are shown in (b and c). The T91 specimen was tested under the conditions: T = 350 °C, $\varepsilon_a$ = 0.76%, $C_O = 5.8 \times 10^{-9}$ wt.% [45]

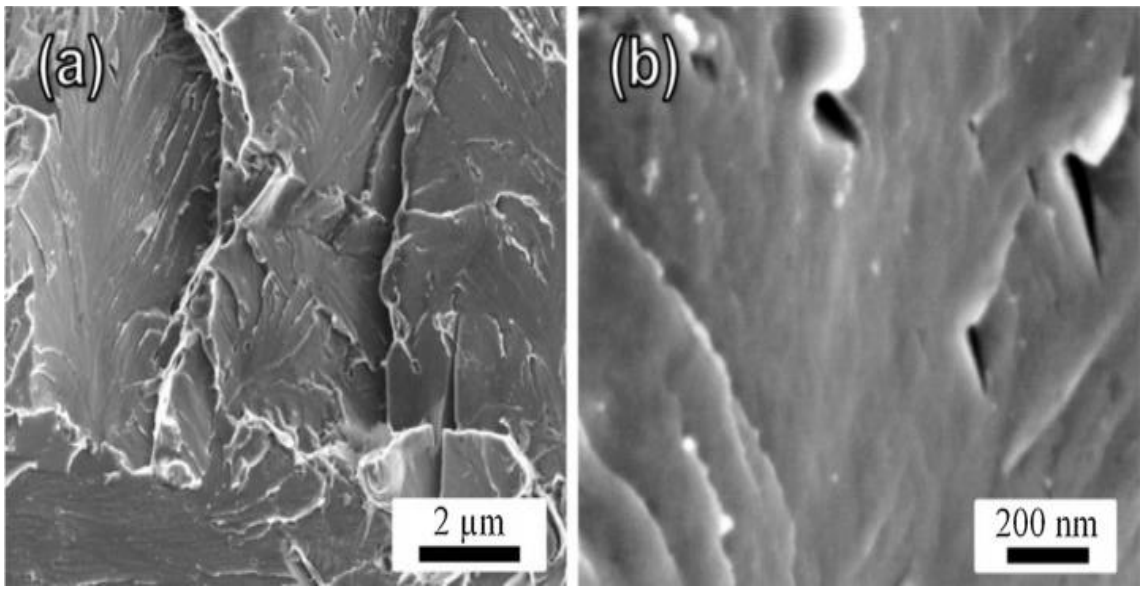


Figure 4.7: High resolution SEM micrographs of a cleavage fracture surface of T91 steel, generated by fracturing in liquid nitrogen, showing river patterns and brittle facets (a) and the absence of the nanoscale dimples lower than 10 nm (b). [45]

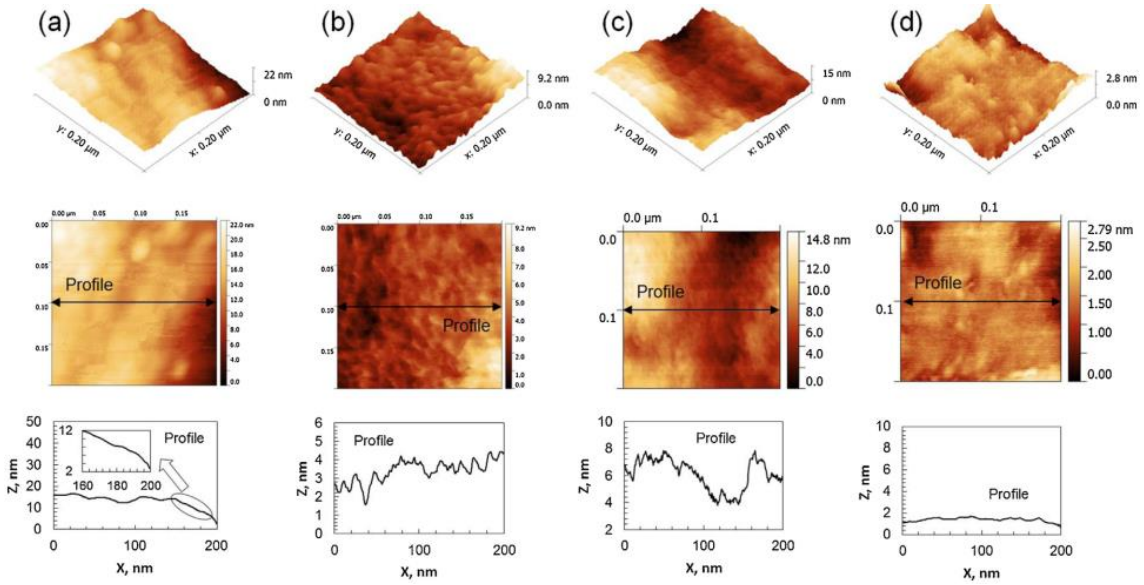


Figure 4.8: AFM topographic images of fracture surfaces: (a) fracture surface created in liquid N2; (b and c) fatigue fracture surfaces generated in the presence of LBE under the following conditions: T = 350 °C, $\varepsilon_a$ = 0.74%, $C_O = 6 \times 10^{-10}$ wt.%; (d) the fracture surface created in liquid $N_2$ and then exposed to LBE at 350–280 °C for about 4 h. [45]

### 4.1.2 Fatigue Tests at CNRS

Difference between tests in air and tests in oxygen saturated LBE

The evolution of the stress amplitude with the number of cycles for tests performed at 350°C in air and in oxygen saturated LBE using the triangular wave form with a strain rate of 4 $.10^{-3}$ $s^{-1}$ shows that T91 exhibits a strong cyclic softening which is not influenced by the considered environments.

The rapid decrease in the stress amplitude before failure corresponds to the propagation in the bulk of a long crack (Figure 4.8).

However, the fatigue life is considerably shorter in LBE than in air.

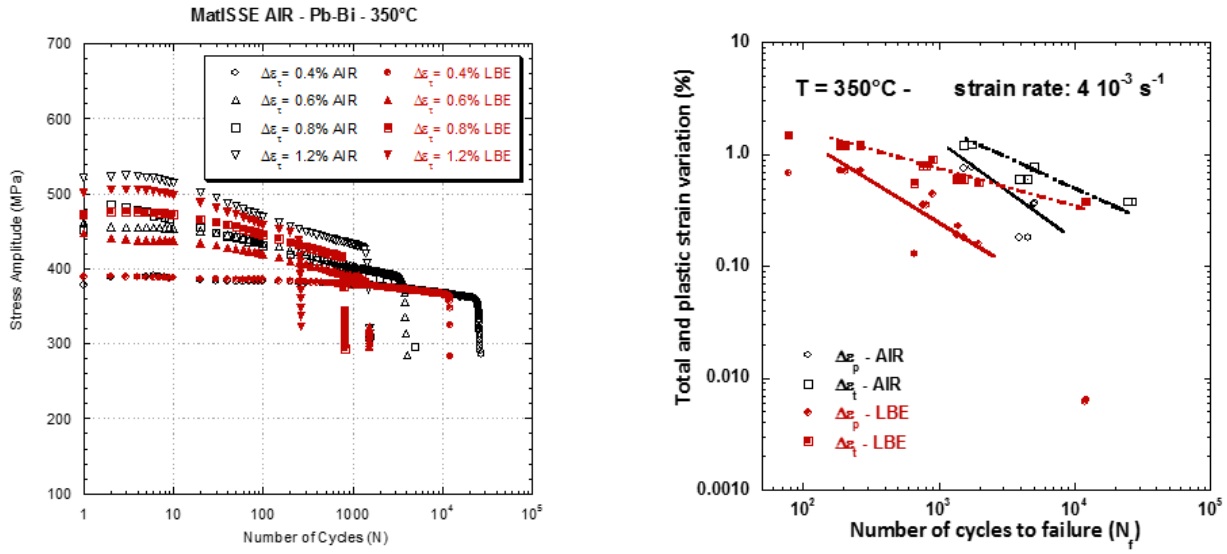


Figure 4.9: Comparison of fatigue results of T91 steel at 350 °C in LBE and air.

Cycling at 300°C instead of 350°C did not change the cyclic response since both the shape of the curves and the stress values remain the same but leads to higher fatigue lives (Figure 4.10).

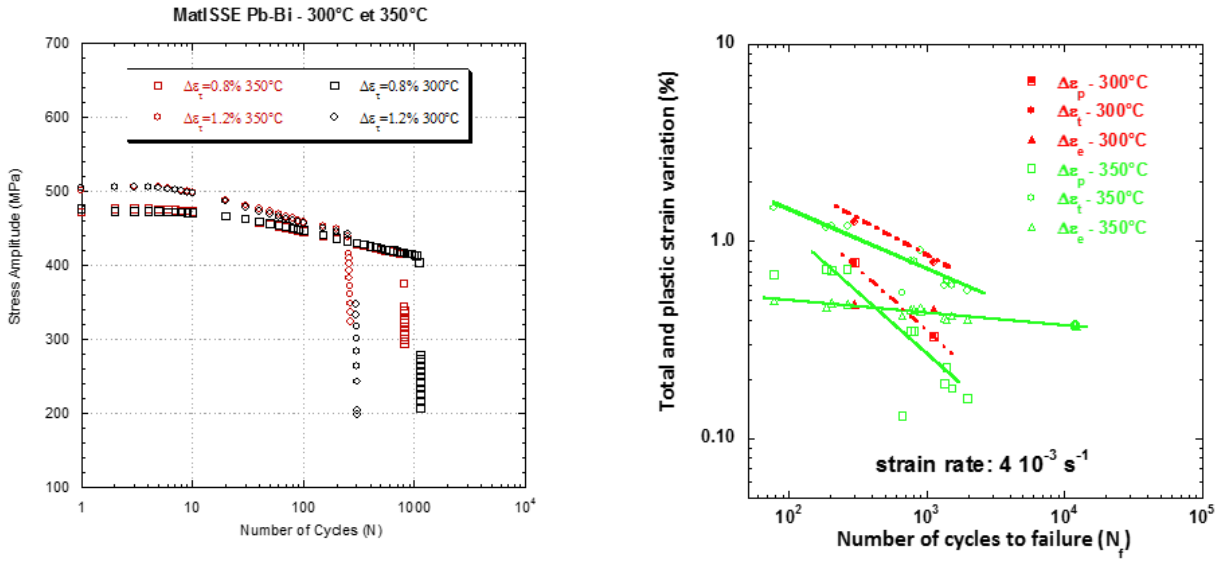


Figure 4.10: Comparison of fatigue results of T91 steel at 300 and 350 °C.

Cycling in low oxygen LBE instead of oxygen saturated did not change the cyclic response since both the shape of the curves and the stress values remain the same (triangular wave form with a strain rate of 4 .$10^{-3}$ $s^{-1}$) (Figure 4.11).

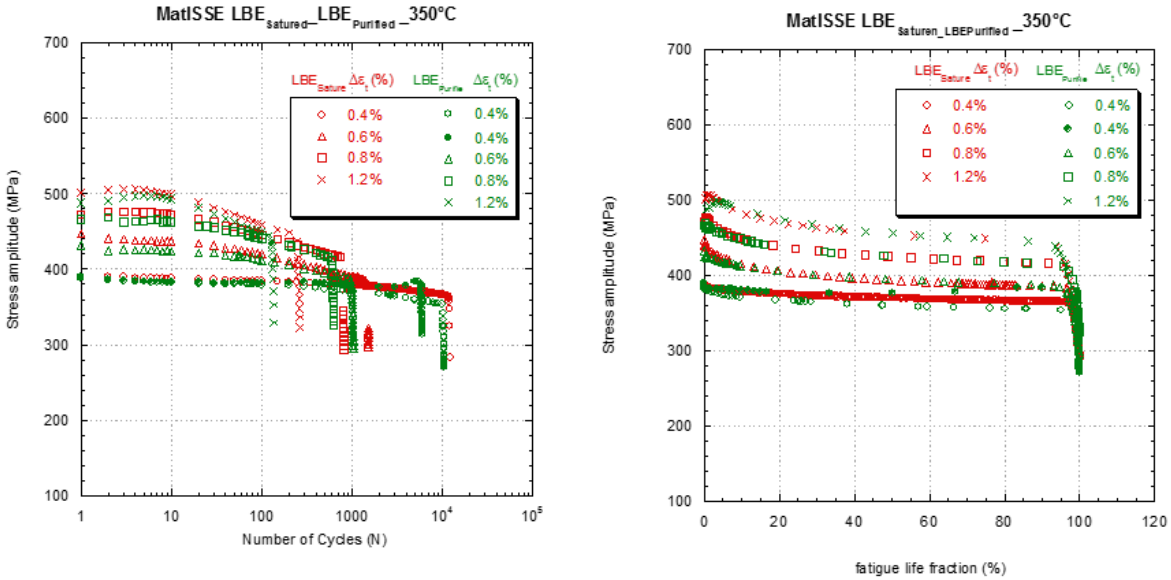


Figure 4.11: Comparison of fatigue results of T91 steel at 350 °C in saturated and purified ($c_o$=$10^{-7}$ – $10^{-9}$ wt%) LBE.

For the fatigue resistance, decreasing the oxygen content may decrease the fatigue life. Indeed, we found that the data obeyed two tendencies:

- Fatigue lives are of the same order than the test that was performed in oxygen saturated or low oxygen content LBE
- Fatigue lives are shorter for tests performed in low oxygen content LBE than for those performed in saturated oxygen LBE

It should be noted that the apparent scattering is not related with the possible variation in the average oxygen content in the low oxygen LBE.

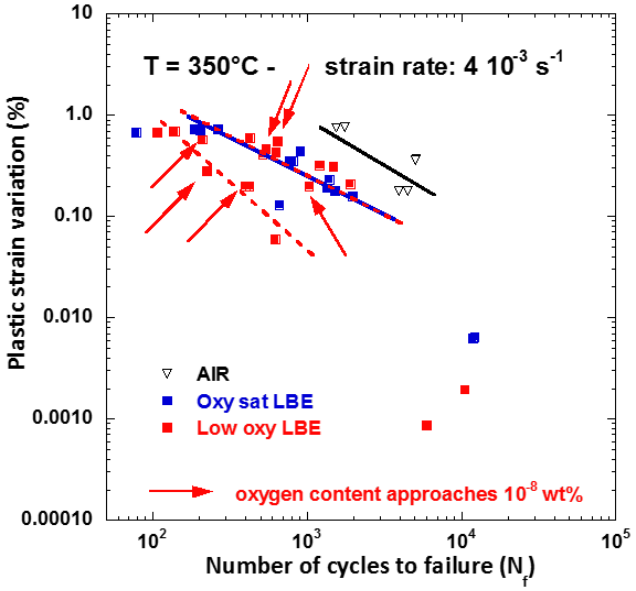


Figure 4.12: Comparison of fatigue results of T91 steel at 350 °C.

In oxygen saturated LBE at 350°C, changing the strain rate from 4 .$10^{-3}$ $s^{-1}$ to 4. $10^{-4}$ $s^{-1}$ in the triangular signal did not produce a huge effect except at the beginning of cycling for the low strain range test.

With the limited number of tests, it is difficult to conclude but the decrease in strain rate seems to impact the fatigue resistance in oxygen saturated LBE at high strain range.

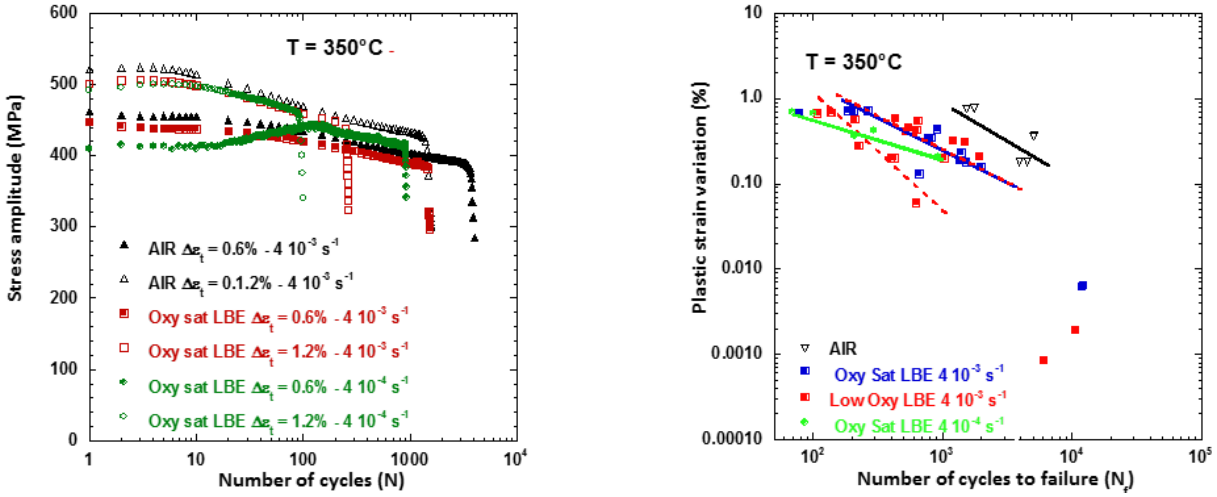


Figure 4.13: (Summary) Comparison of fatigue results of T91 steel at 350 °C

In oxygen saturated LBE at 350°C, the introduction of a holding time of 10 minutes did not produce a huge effect on the cyclic response.

With the limited number of tests, it is difficult to conclude but the introduction of a holding time seems to impact the fatigue resistance in oxygen saturated LBE at low strain range.

It also can be noted that the decrease oxygen content in LBE is of higher importance.

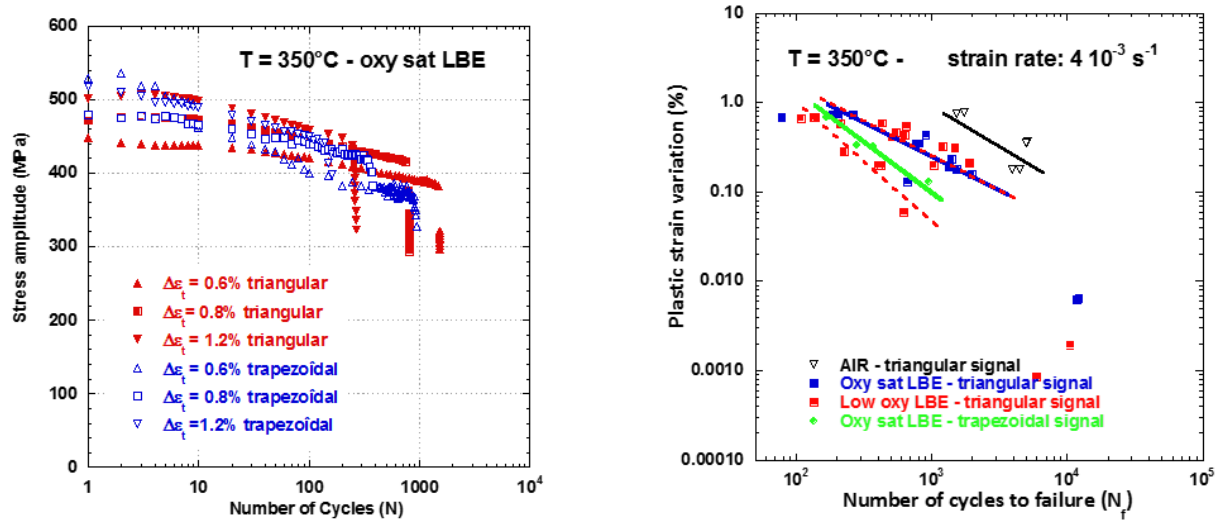


Figure 4.14: Comparison of fatigue results of T91 steel at 350 °C for different types of strain rate

## 4.2 Crack Propagation

### 4.2.1 Crack Propagation at SCK-CEN

In order to investigate the effect of crack initiation due to liquid metal embrittlement a series of tensile tests have been conducted. For these tensile tests notched cylindrical T91 samples were used. The samples were exposed to low oxygen containing LBE during the tests. The gained results show a unique phenomenon of unstable cracking which leads to the formation of striation like markings on the fracture surface. An example for such markings can be found in Figure 4.15. Such marking have also been reported by other researchers [5,

12] on T91 and other steels and were attributed to the effect of dynamic strain aging. The results in this work, nevertheless, link the formation of these 'striations' to the coupled effect of liquid metal embrittlement and the compliance of the tensile machines. In Figure 4.1, a comparison of load-displacement curves for different tensile test machines with different compliance can be found. As can be seen from this figure the profiles of the curves are the same as usual but the final parts of the LIMETS1 and LIMETS4 curves in Figure 4.1 show steps which are not often seen in tensile tests. These final parts are characterized by 'steps' of alternate occurrence of sudden load dropping and load dwelling events. By comparing the load displacement curves of machines with different stiffness it can be shown that this effect disappears with increasing compliances of the testing machine. Based on fractographic examinations (Figure 4.15) it can be expected that the markings can be related to the steps in the tensile curves in further consequence be related to the crack extension rate. Therefore, using SEM, the widths of such markings were manually measured and plotted as function of crack length (Figure 4.15). A conservative estimate of the crack propagation rate of 2 to 76 µm/s could be made.

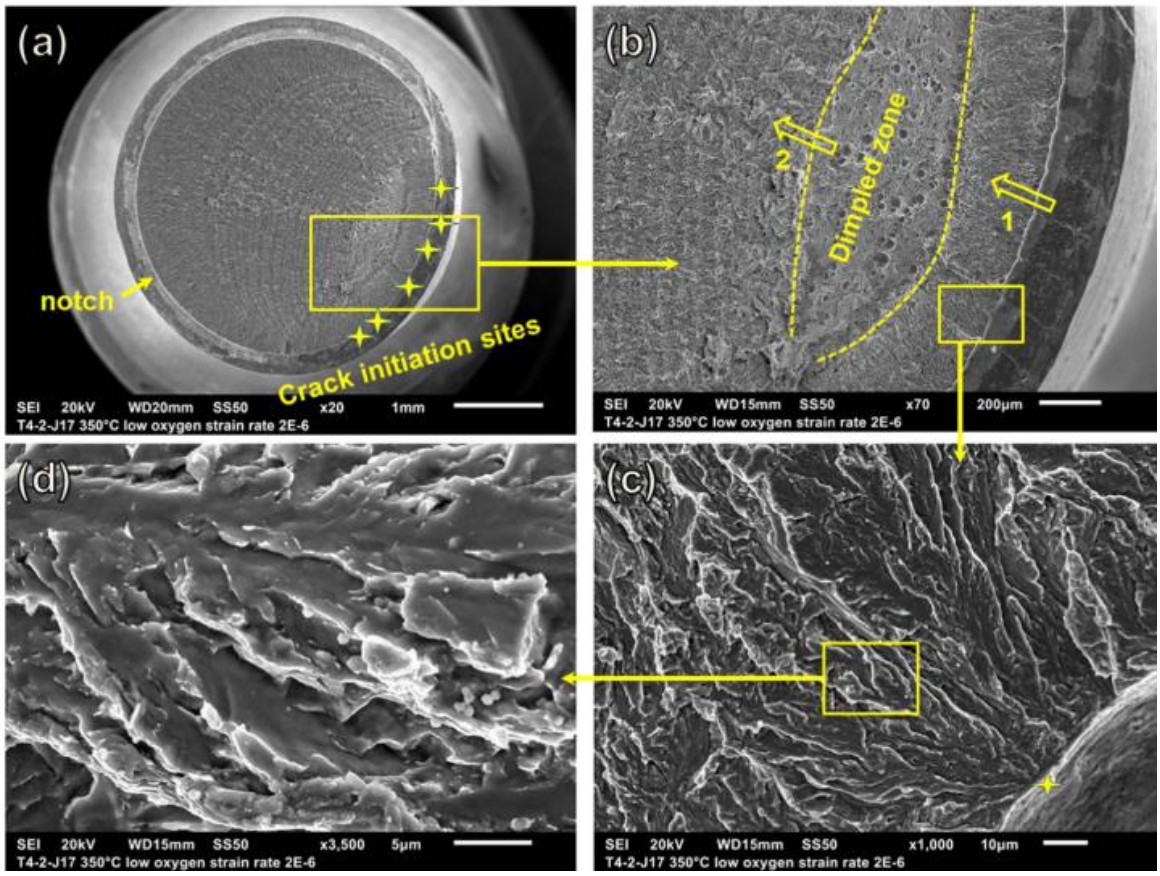


Figure 4. 15: Fractography of the fracture surface of a notched T91 tensile sample tested in low oxygen LBE at 350°C [46].

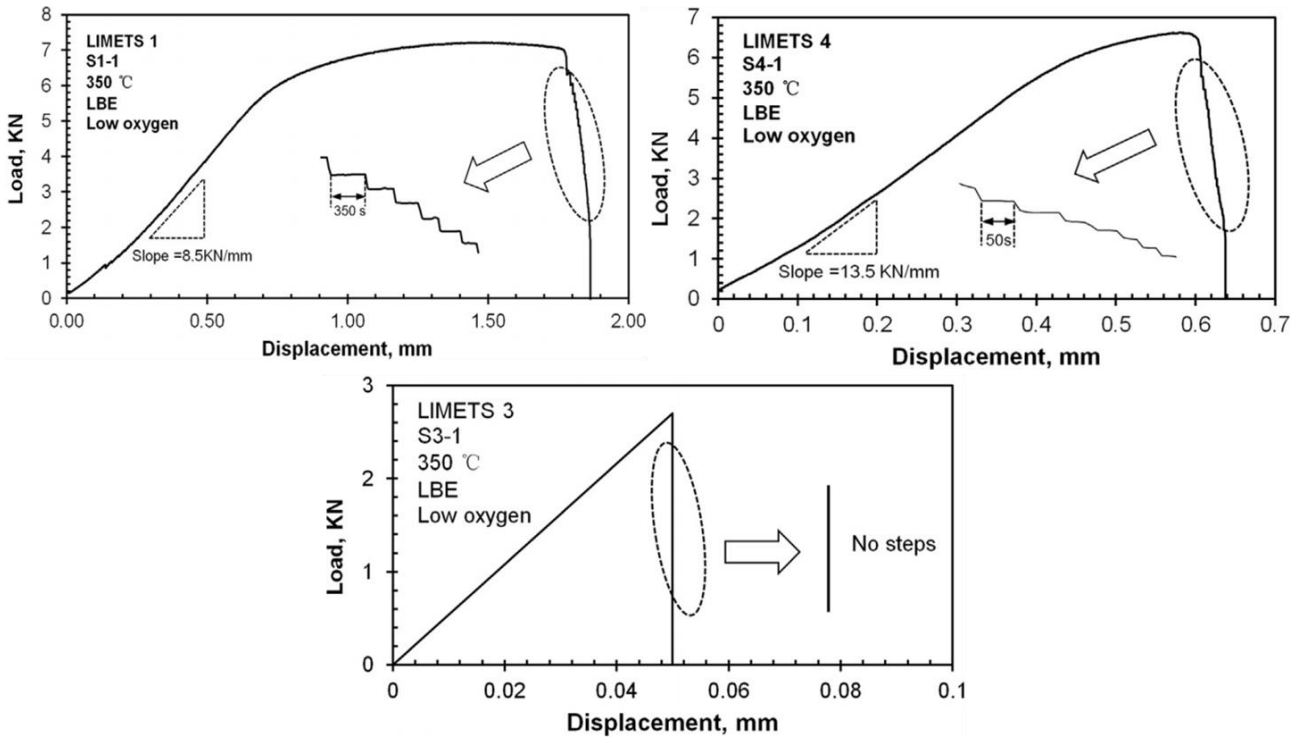


Figure 4.16: Comparison of stress strain curves for different tensile test machines [46].

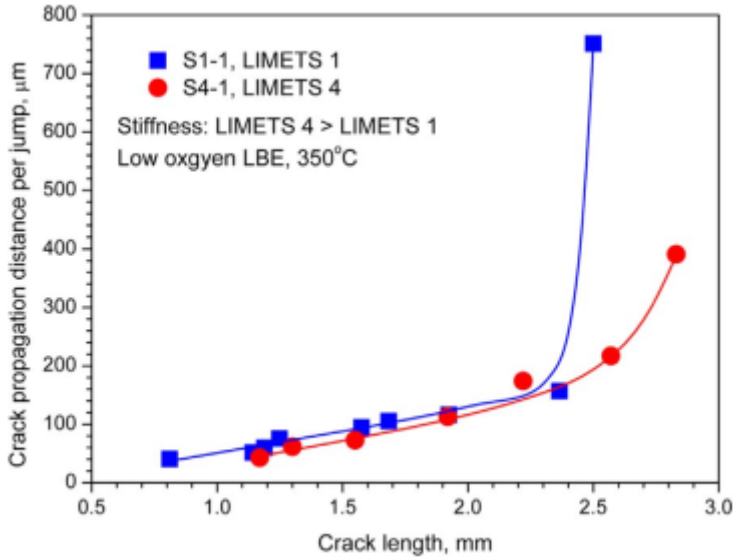


Figure 4.17: Crack propagation distance as function of crack length indirectly indicating the LME crack propagation rates [46].

### 4.2.2 Crack Propagation at CNRS

The fracture surface of the specimen failed in air is shown in Figure 4.18. A lot of crack initiation sites can be identified. From these, some cracks propagated from the surface into the bulk at different depths and the final fracture occurred by tensile loading. The surface fracture detail in Figure 4.18b shows ductile fatigue striations.

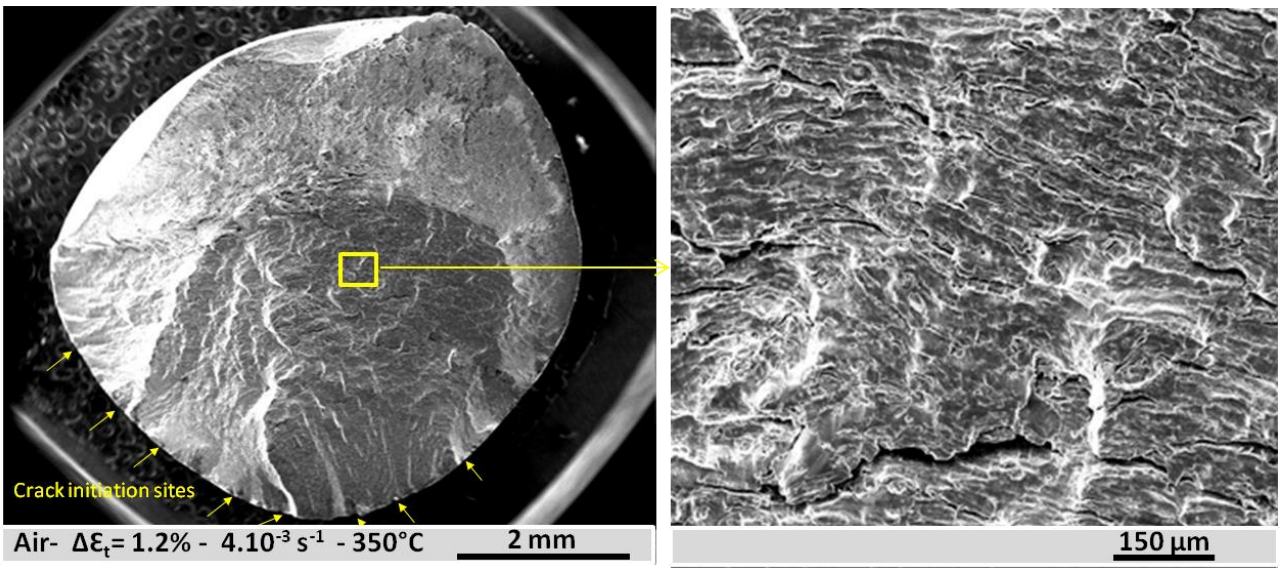


Figure 4.18: Fracture surface of T91 after fatigue test in the air at 350°C.

The fracture surfaces of the specimen failed in oxygen saturated and low oxygen LBE were very flat. Striations could be seen at the naked eye Figure 4.19 and Figure 4.20. At higher magnification, brittle fracture was unambiguously observed. The same feature was observed for both strain rates.

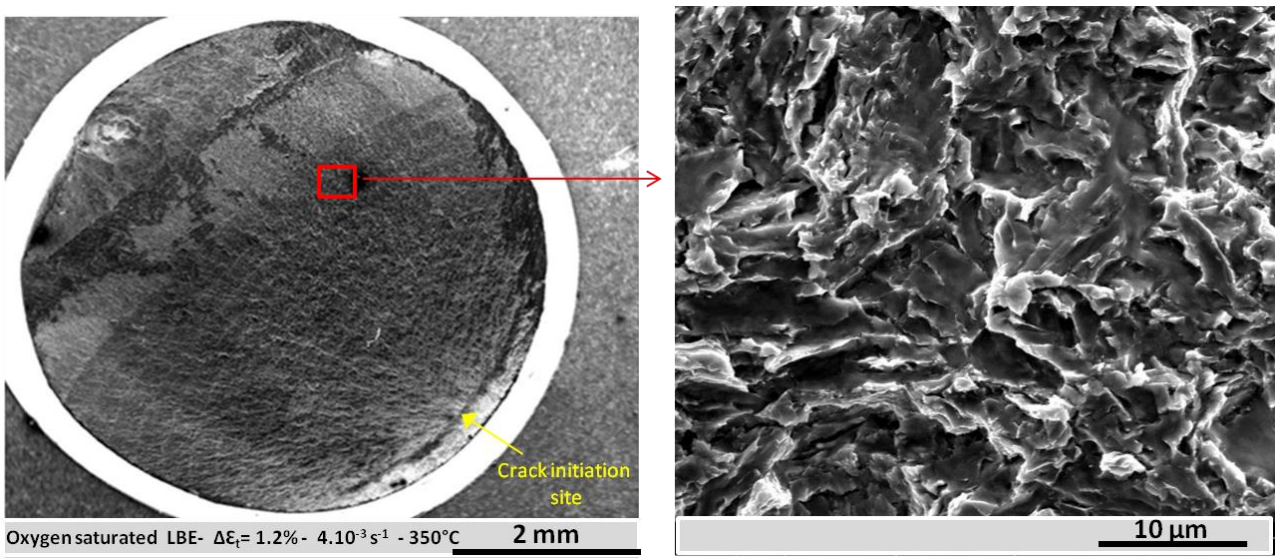


Figure 4.19: Fracture surface of T91 after fatigue test in saturated LBE at 350°C (strain rate 4·10$^{-3}$ s$^{-1}$) a) overview, b) detail out of a).

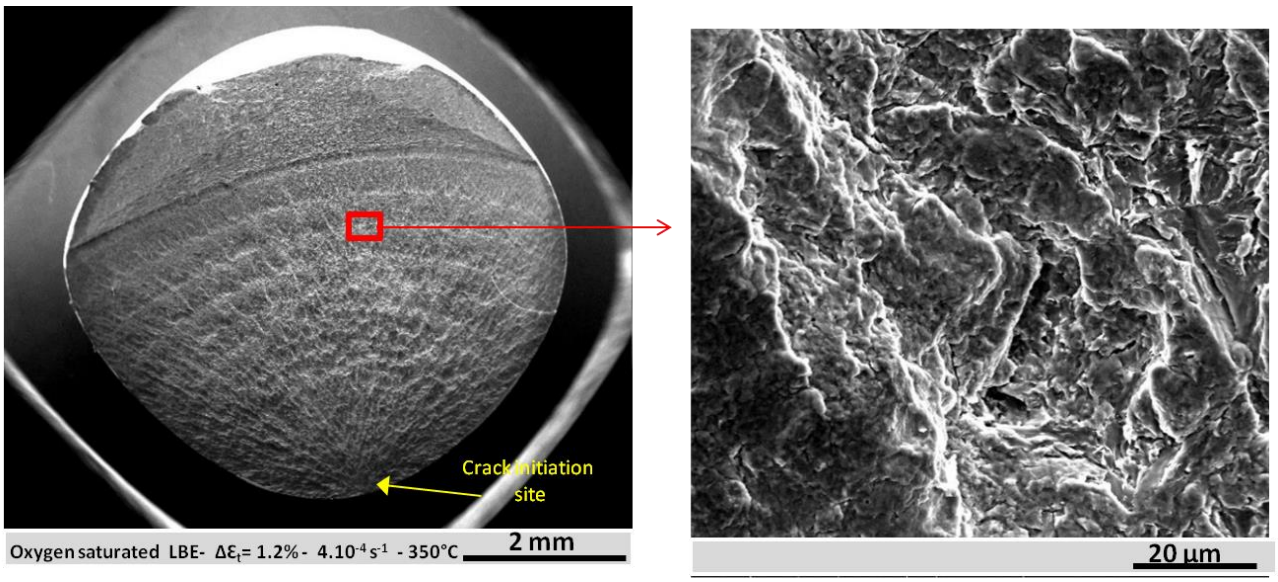


Figure 4.20: Fracture surface of T91 after fatigue test in saturated LBE at 350°C (strain rate 4·10$^{-4}$ s$^{-1}$) a) overview, b) detail out of a).

### 4.2.3 Crack Propagation at CVR

Materials T91 (specimen designation CT-T) and 316L (specimen designation CT-L) were tested for Fatigue Crack Growth Tests (cyclic frequency ca. 0.25 Hz) on CT specimens at 300 °C in air and LBE with various oxygen amount. The fracture surface was observed and characteristics of the FCG speed were compared. Parameters and FCG results are summarized in Tables 4.1 and 4.2 and summarized in Figures 4.20 and 4.25.

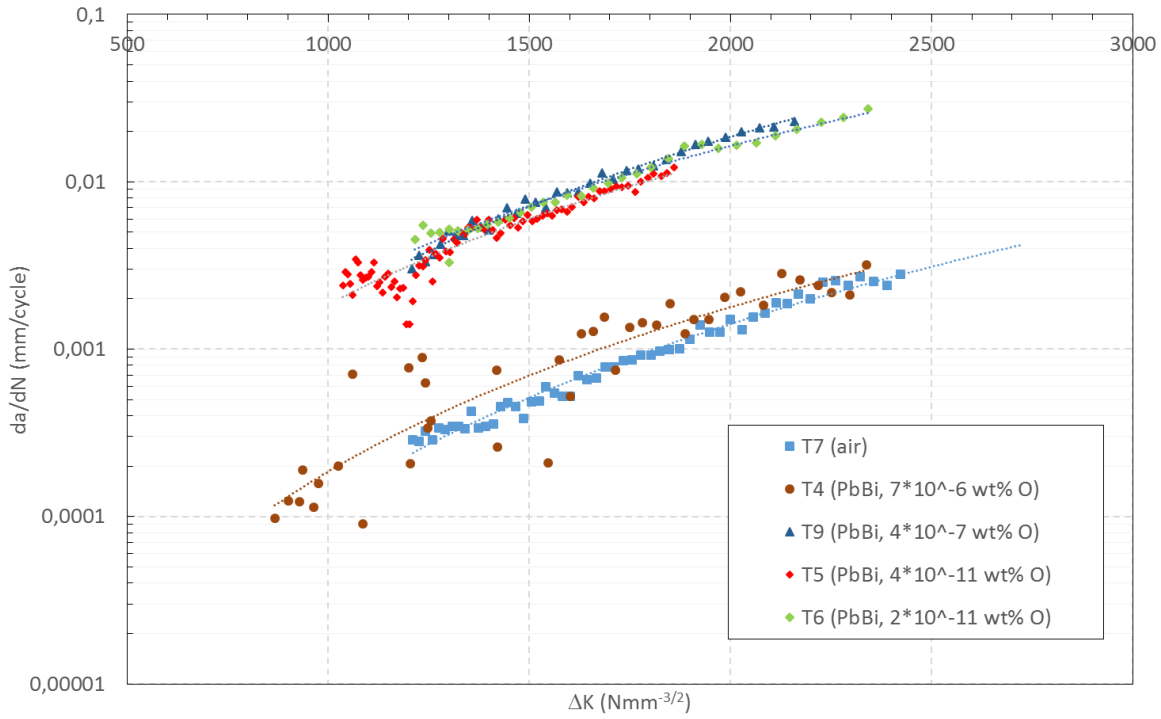


Figure 4.21: Fatigue crack growth of T91 steel at 300 °C comparing air and LBE environment.

Table 4-1: Parameters and results of Fatigue Crack Growth of T91 steel.

| **Designation** | **$a_0$** | **$P_{max}$** | **R-ratio** | **T** | **Δa** | **N (cycles)** | **Environment** | **FCG: $\frac{da}{dN} = C1 \cdot \Delta K^{C2}$** | |
|---|---|---|---|---|---|---|---|---|---|
| | mm | kN | - | °C | mm | - | ($c_o$ in wt%) | **C1** | **C2** |
| CT-T7 | 12.14 | 4.0 | 0.1 | 300 | 5.25 | 14770 | air | $3.25 \cdot 10^{-15}$ | 3.53 |
| CT-T4 | 12.14 | 3.5 | 0.1 | 300 | 5.25 | 19700 | LBE ($7 \cdot 10^{-6}$) | $3.00 \cdot 10^{-14}$ | 3.26 |
| CT-T5 | 12.55 | 3.5 | 0.1 | 300 | 5.95 | 1800 | LBE ($4 \cdot 10^{-11}$) | $4.00 \cdot 10^{-12}$ | 2.89 |
| CT-T6 | 12.28 | 2.75 | 0.1 | 300 | 6.30 | 23807 | LBE ($2 \cdot 10^{-11}$) | $6.13 \cdot 10^{-12}$ | 2.86 |
| CT-T9 | 12.37 | 3.5 | 0.1 | 300 | 5.35 | 6526 | LBE ($4 \cdot 10^{-7}$) | $1.76 \cdot 10^{-13}$ | 3.34 |

The increase of CGR, in the case of the sample CT-T6 seems surprising due to the lower maximum loading than CT-5. This specimen requires further detailed investigations and ye disregard it for the subsequent analysis. Figures 4.22 – 4.25 show fracture areas from T91 fatigue crack growth test specimens at 300 °C at a distance of approx. 1 mm from the precrack line. The specimen CT-T7 was tested in air. The fracture area (Figure 4.22) shows transgranular crack growth path with ductile striation morphology during the fatigue loading. The specimen CT-T4 was tested in the LBE with high concentration of oxygen. The fracture area (Figure 4.23) shows also transgranular fracture with striation morphology which is similar to specimen tested in the air environment. Similar behavior is also in crack growth speed shown in Figure 4.20. The specimen CT-T9 was tested in the LBE with $4 \cdot 10^{-7}$ wt% concentration of oxygen. The fracture area (Figure 4.24) did not show striations, but more irregular fracture surface consisting of cleavage-like facets locally following intergranular planes. The crack growth speed (Figure 4.21) shows high increase. The specimen CT-T6 was tested in in the LBE with low oxygen amount ($2 \cdot 10^{-11}$ wt%). The fracture area (Figure 4.25) shows character of fracture similar to the specimen CT-T9. The crack growth speed (Figure 4.21) is the same as for the specimen CT-T9.

The T91 results from FCG in LBE shows negligible changes in crack growth speed at oxygen amount near saturated state in comparison with air. However, the crack growth speed increases when the oxygen content is reduced to $4 \cdot 10^{-7}$ wt%. The speed is more than 10-times higher than in the air. The speed is then similar with decreasing oxygen amount and no significant changes were observed following further reduction of the oxygen content.

a)

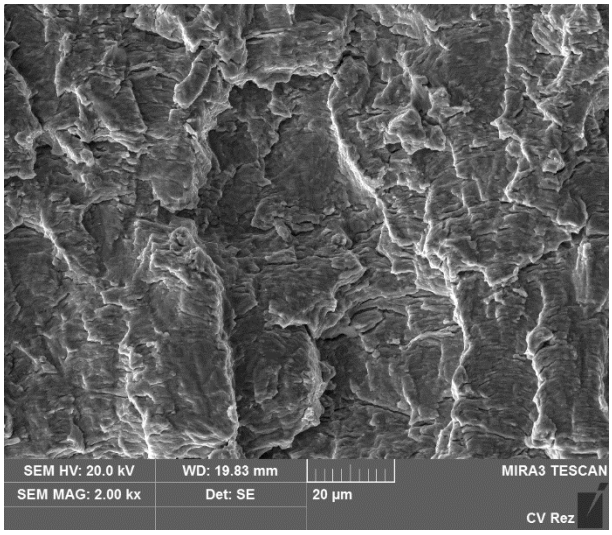


b)

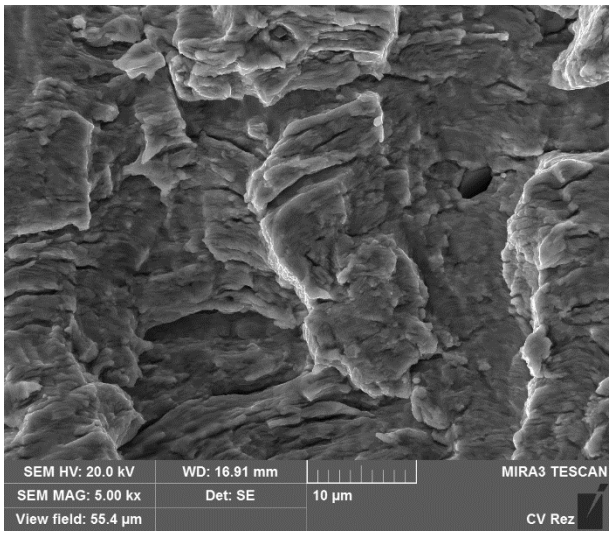


Figure 4.22: Sample CT-T7– steel T91, 300 °C, air: (a) fracture area, (b) detail.

a)

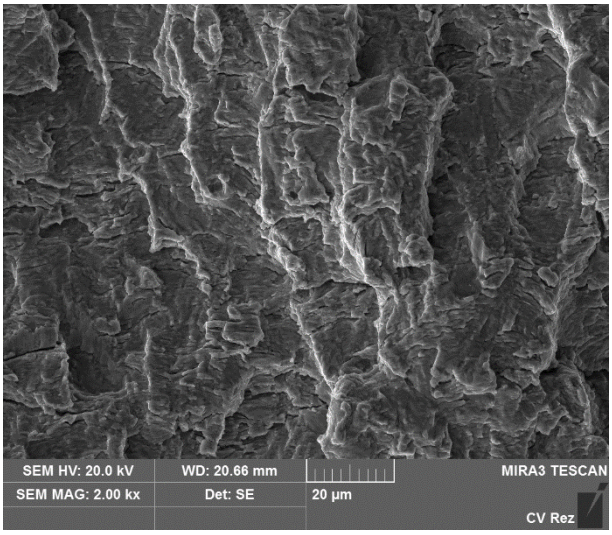


b)

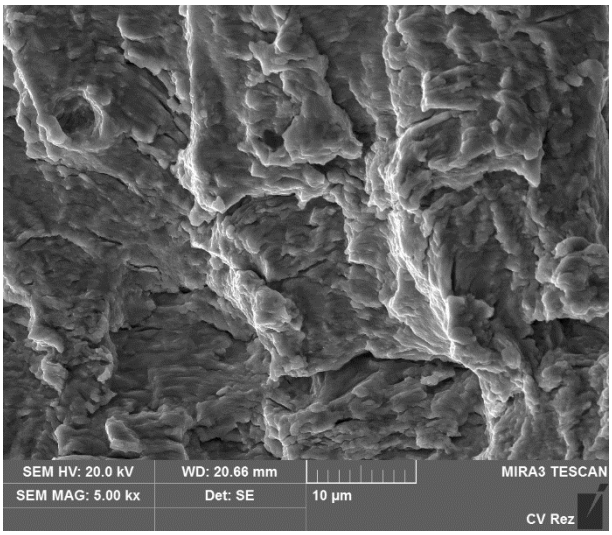


Figure 4.23: CT-T4– steel T91, 300 °C, PbBi, $c_o=7\cdot10^{-6}$ wt%: (a) fracture area, (b) detail

a)

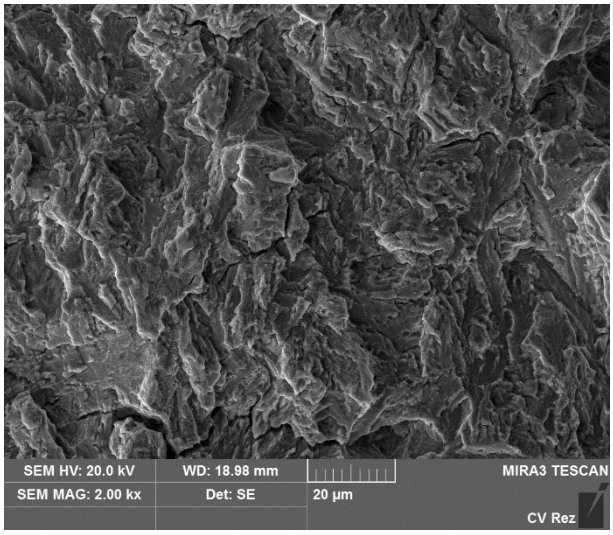


b)

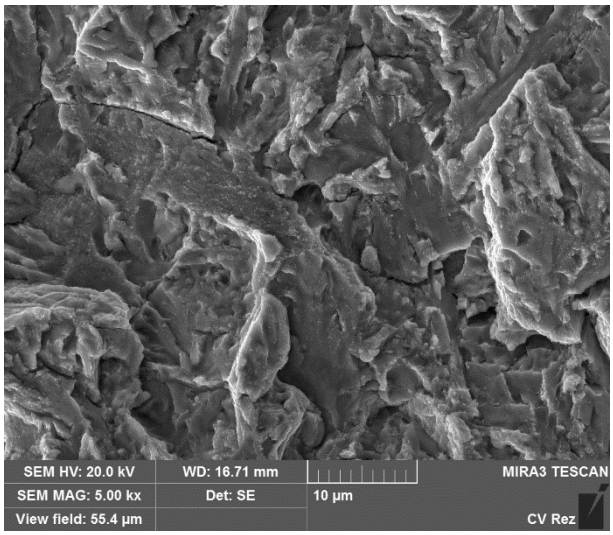


Figure 4.24: Sample CT-T9 – steel T91, 300 °C, PbBi, $c_o=4\cdot10^{-7}$ wt%: (a) fracture area, (b) detail.

a)

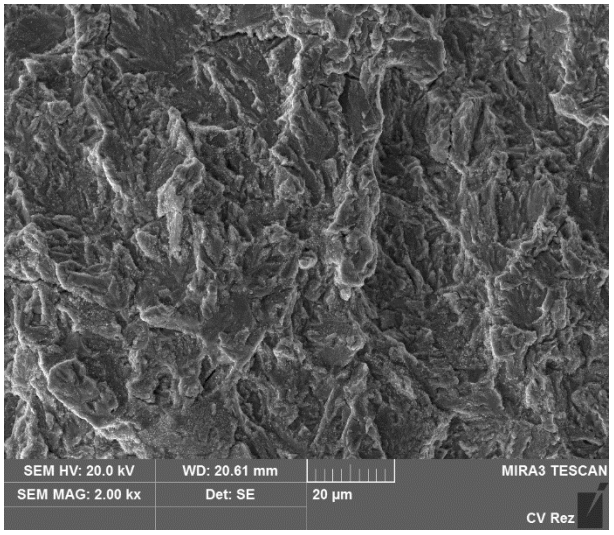


b)

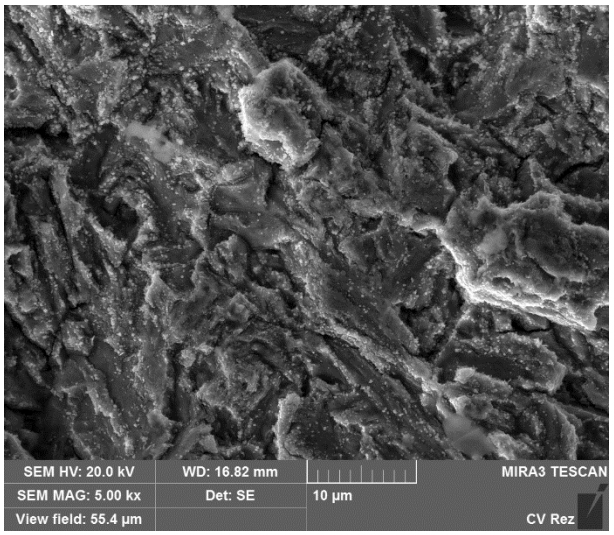


Figure 4.25: Sample CT-T6 – steel T91, 300 °C, PbBi, $c_o=2\cdot10^{-11}$ wt% : (a) fracture area, (b) detail.

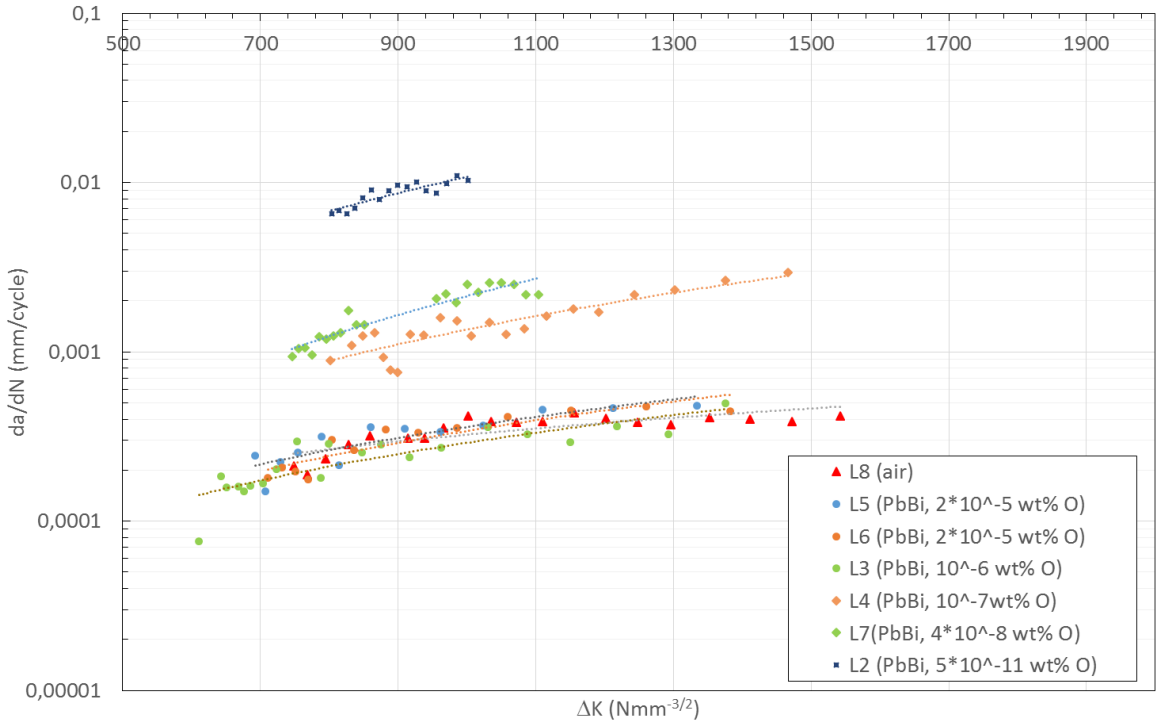


Figure 4.26: Fatigue crack growth of 316L stainless steel at 300 °C comparing air and LBE environment.

Table 4-2: Parameters and results of Fatigue Crack Growth of 316 steel.

| **Designation** | **$a_0$** | **$P_{max}$** | **R-ratio** | **T** | **Δa** | **N (cycles)** | **Environment** | **FCG: $\frac{da}{dN} = C1 \cdot \Delta K^{C2}$** | |
|---|---|---|---|---|---|---|---|---|---|
| | mm | kN | - | °C | mm | - | ($c_o$ in wt%) | **C1** | **C2** |
| CT-L2 | 13.26 | 2.5 | 0.1 | 300 | 5.70 | 2764 | LBE ($5 \cdot 10^{-11}$) | $5.47 \cdot 10^{-9}$ | 2.10 |
| CT-L3 | 12.94 | 2.25 | 0.1 | 300 | 6.35 | 16583 | LBE ($10^{-6}$) | $1.40 \cdot 10^{-8}$ | 1.44 |
| CT-L4 | 12.38 | 2.25 | 0.1 | 300 | 6.0 | 15500 | LBE ($10^{-7}$) | $2.50 \cdot 10^{-9}$ | 1.91 |
| CT-L5 | 12.49 | 2.25 | 0.1 | 300 | 6.30 | 24841 | LBE ($2 \cdot 10^{-5}$) | $1.92 \cdot 10^{-8}$ | 1.42 |
| CT-L6 | 12.55 | 2.25 | 0.1 | 300 | 5.70 | 30594 | LBE ($2 \cdot 10^{-5}$) | $8.88 \cdot 10^{-9}$ | 1.53 |
| CT-L7 | 12.35 | 2.25 | 0.1 | 300 | 6.10 | 13607 | LBE ($4 \cdot 10^{-8}$) | $9.56 \cdot 10^{-11}$ | 2.45 |
| CT-L8 | 12.47 | 2.25 | 0.1 | 300 | 5.80 | 31954 | air | $5.92 \cdot 10^{-9}$ | 1.59 |

Figure 4.27 – 4.30 show fracture areas of 316L FCG test specimens at 300 °C in a distance ca. 1 mm from the pre-crack line. The specimen CT-L8 was tested in air. The fracture area (Figure 4.27) shows transgranular fracture with striation morphology during the fatigue loading similar to steel T91, but with more significant striations. Specimen CT-L3 was tested in the LBE with high concentration of oxygen. The fracture area (Figure 4.26) shows also transgranular fracture with striation morphology which is similar to the specimen tested in the air environment, although it was observed an increase in roughness. Similar behavior to air environment is also in crack growth speed shown in Figure 4.26. Specimen CT-L7 was tested in LBE with $4 \times 10^{-8}$ wt% concentration of oxygen. The fracture area (Figure 4.28) shows high ratio of intergranular fracture. The crack growth speed (Figure 4.26) shows a slight increase. Specimen CT-L2 was tested in LBE with low oxygen amount ($5 \cdot 10^{-11}$ wt%). The fracture area (Figure 4.30) shows also a higher ratio of intergranular fracture. The crack growth speed (Figure 4.26) is also higher than in previous cases.

The 316L results from FCG in LBE shows negligible changes in crack growth speed with an oxygen content near the saturated state. However, the crack growth speed increases slightly when the oxygen concentration changes from $10^{-6}$ to$\cdot 10^{-7}$ wt%.

a)
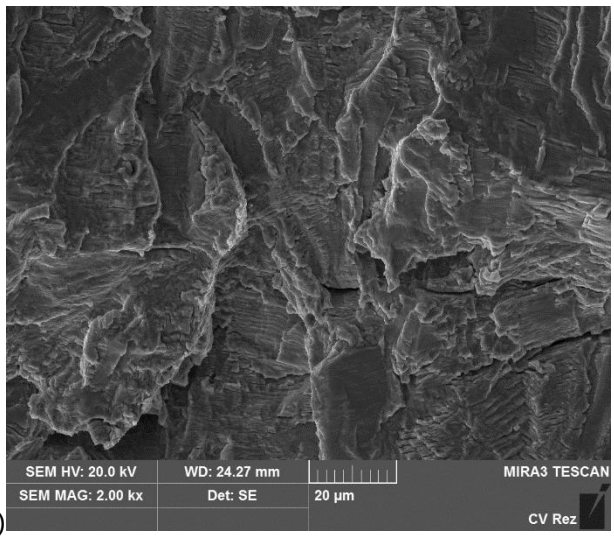


b)
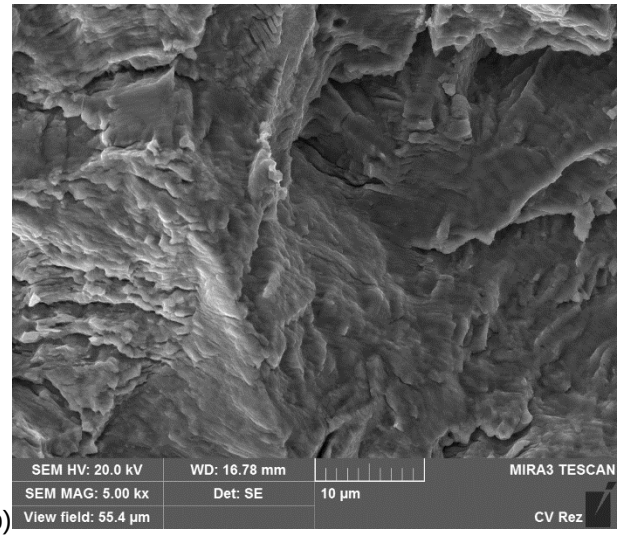


Figure 4.27: Sample: CT-L8 – steel 316L, 300 °C, air: (a) fracture area, (b) detail.

a)
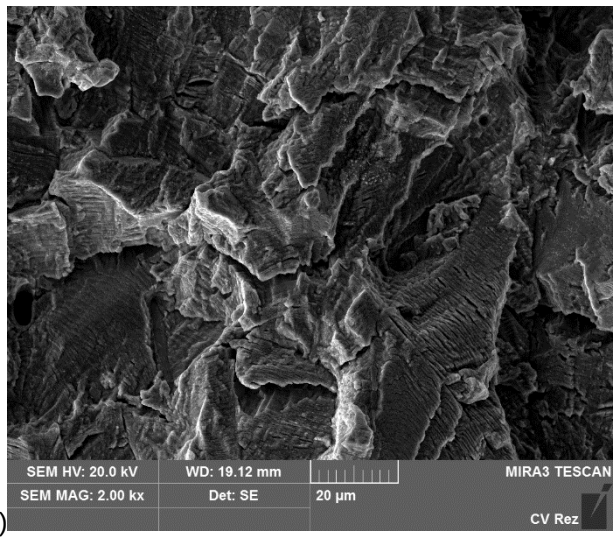


b)
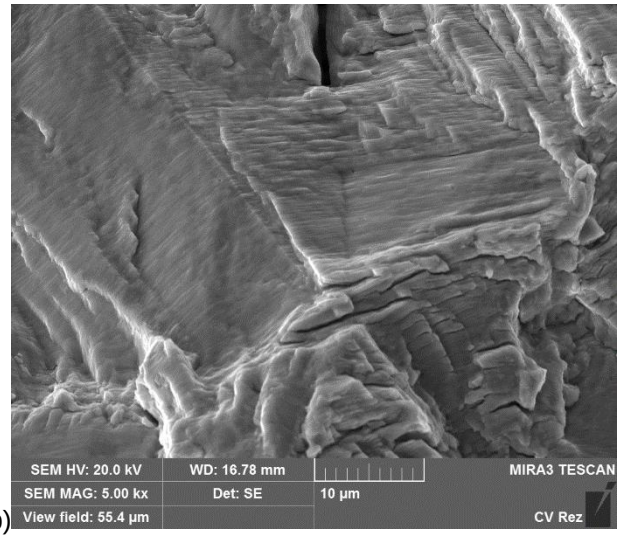


Figure 4.28: Sample CT-L3 – steel 316L, 300 °C, PbBi, $c_o=10^{-6}$ wt%: (a) fracture area, (b) detail.

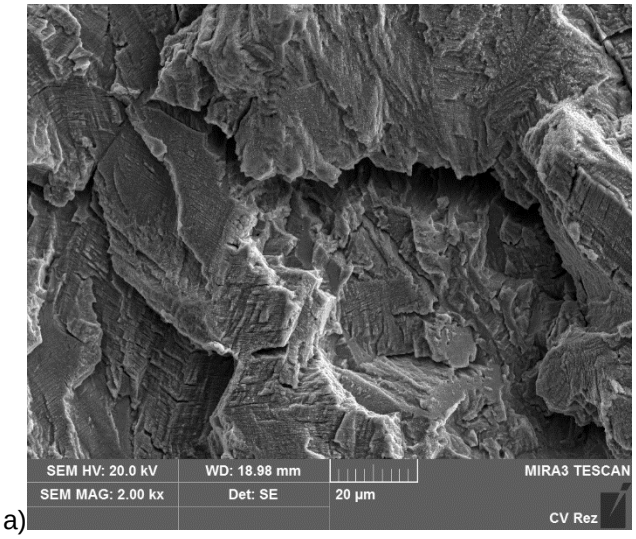


a)

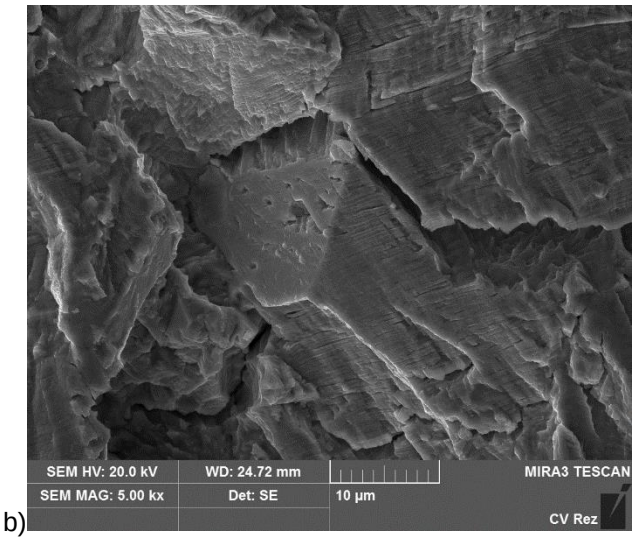


b)

Figure 4.29: Sample CT-L7 – steel 316L, 300 °C, PbBi, $c_o=4\cdot10^{-8}$ wt%: (a) fracture area, (b) detail.

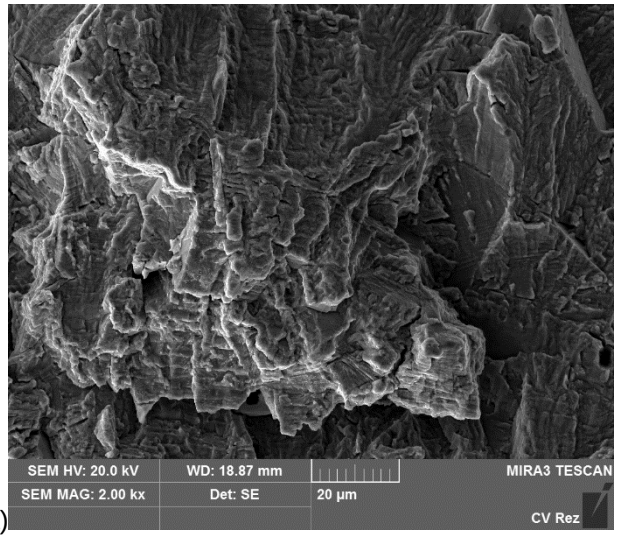


a)

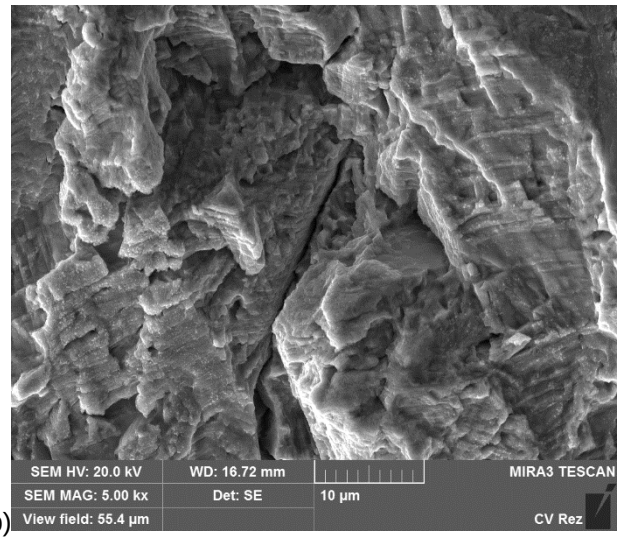


b)

Figure 4.30: Sample CT-L2 – steel 316L, 300 °C, PbBi, $c_o=5\cdot10^{-11}$ wt%: (a) fracture area, (b) detail.

The Crack growth rate (CGR) as a function of the range of $\Delta K$ shows that for both the T91 steel and the 316L steel one observes a CGR increase in the presence of LBE (respectively an increase by a factor of 10 for T91 and a factor of 5 for 316L). One can estimate the potential error induced by the lack of an extensometer located at the lips of the CT geometry: the $\Delta K$ range can be shifted by as much as 6% if the crack opening displacement is not evaluated correctly by the compliance (±10%). In terms of CGR, such a shift of $\Delta K$ leads to a conservative estimate of CGR to be increased only by a factor of 5 for T91 and a factor of 3 for 316L (from a direct reading of Figures 4.21 and 4.26). In the case of T91, this increase is comparable to the one observed by Verleene et al. [14] on low cycle fatigue. For 316L, the observed increase is also comparable to the one observed by Kalkhof et al. [45].

However, it has to be highlighted that interpretation and quantification of data and errors are subject and markedly influenced by the very specific experimental and infrastructures conditions. The fact that these tests were conducted without use of extensometers, does not allow for verification of measurements and cannot be accounted for a final conclusion. More tests will be necessary to quantify and verify the phenomena observed in this study.

## 4.3 Crack Initiation

### 4.3.1 Crack Initiation at CNRS

For tests in air, cracks initiated at the surface of the specimen. From transversal cuts, it can be noted that there were a lot of micro-cracks and that the dimensions of them were ranging between 20 µm to 100 µm. One or few of these micro-cracks transformed into long cracks and propagated through the bulk of the specimen.

In oxygen saturated LBE, cracks also initiated at the surface of the specimen but were very scarce. Once a micro-crack initiated at the surface of the specimen, it propagated as a long crack early and fast in the bulk of the specimen.

In low oxygen LBE, the situation was the same except that we observed additional very short cracks.

In tests where a holding time was introduced, more short micro-cracks were observed.

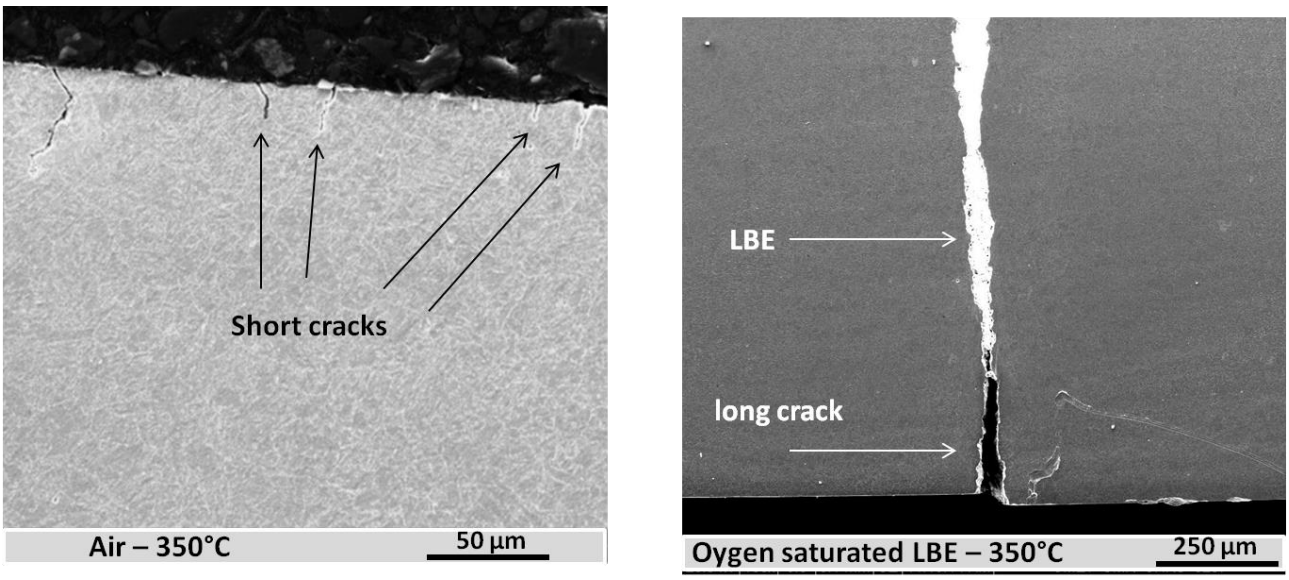


Figure 4.32: Comparison of cracks in cross sections of fatigue samples in T91 at 350°C in air and saturated LBE

### 4.3.2 Crack initiation at CVR

Materials T91 (specimen designation T), 15-15Ti (specimen designation I) and 316L (specimen designation L) were tested under uniaxial tensile Slow Strain Rate Tests (deformation rate 0.0012 mm/min) on tapered specimens with ground and polished surfaces, at 300°C in air and LBE with various oxygen amounts. Surface cracks were observed and their characteristics were compared.

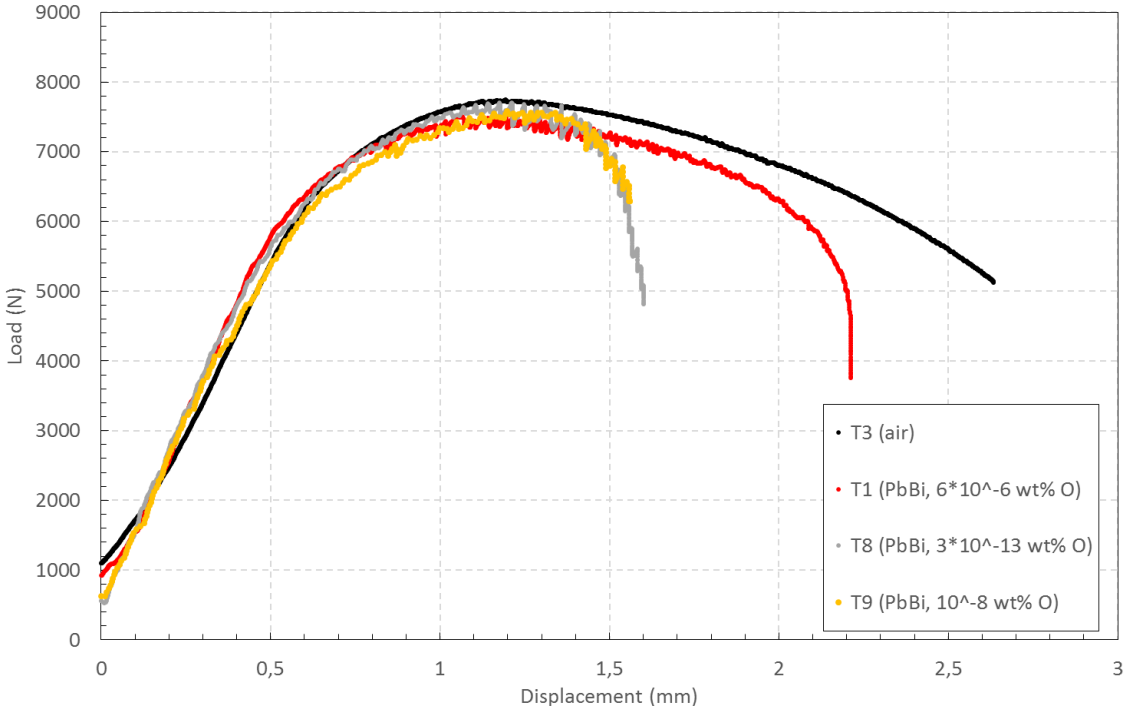


Figure 4.33: Comparison of load-displacement curves for T91 tapered specimens tested up to rupture at 300°C.

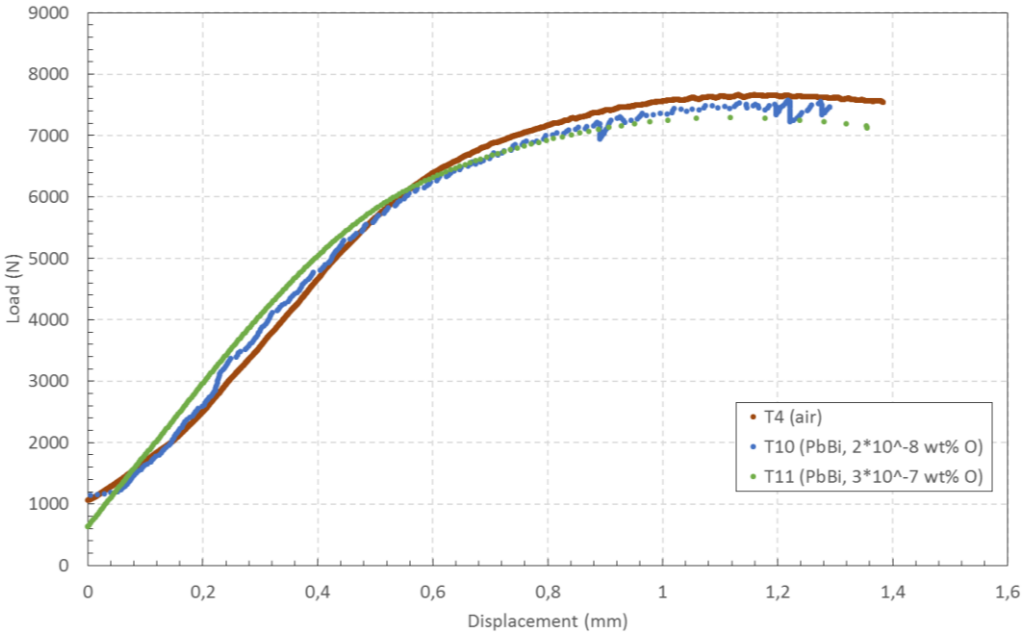


Figure 4.34: Comparison of load-displacement curves for T91 tapered specimens tested up to UTS at 300°C.

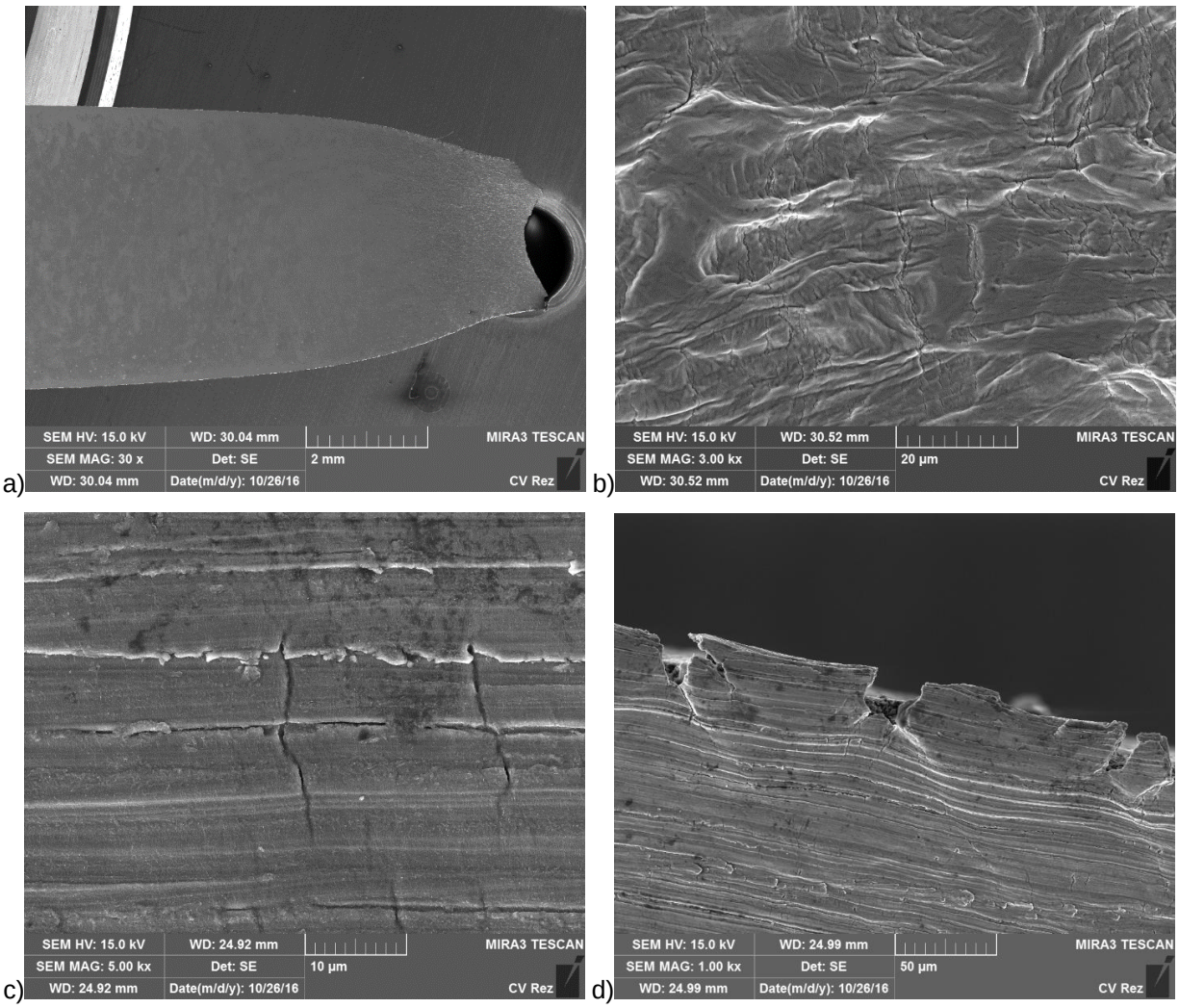


Figure 4.35: (a) T3, rupture (300°C, air), (b) detail of the polished side – ductile behavior of the necking, cracking perpendicular to the load direction, (c) detail of the ground side, similar to polished, (d) detail of the ground-EDM edge – ductile character, wide cracks and plastic deformation observed around the crack tip.

Figure 4.35 (a-d) shows T91 reference test in the air up to rupture. The material has ductile behavior with expected necking (Figure 4.35 b,d). Detailed views display small ductile cracks on the edges (Figure 4.35d) and in the loading axis area (Figure 4.35b,c). Cracks are more significant on the ground side of the specimen (Figure 4.35c). The cracks are mostly shallow and they are all concentrated around the rupture (necking) area.

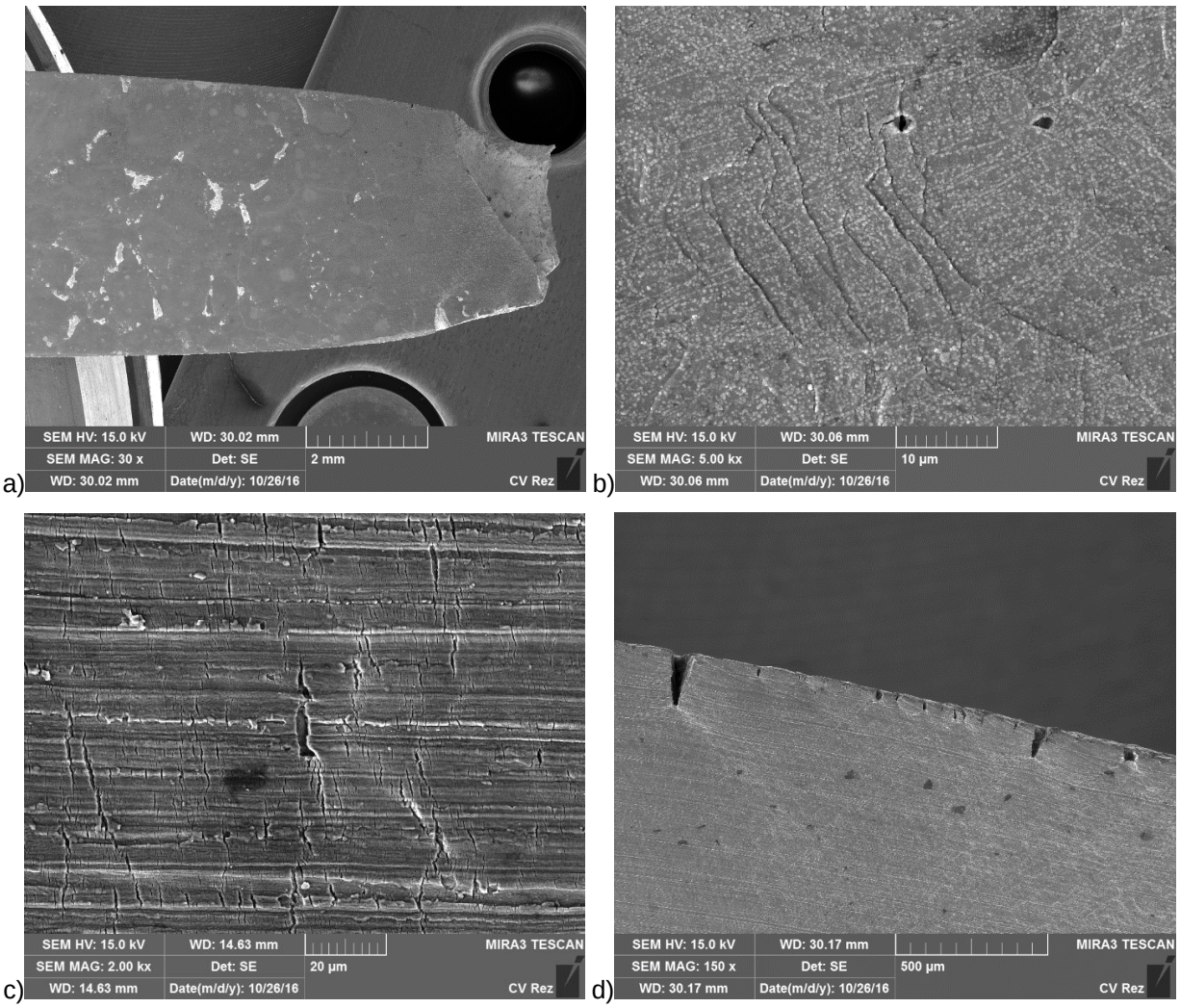


Figure 4.36: (a): T1, rupture (300 °C, LBE, $6 \cdot 10^{-6}$ wt% O), (b) detail, polished side, (c) detail, ground side with cracking, (d) detail, ground-EDM edge – sharp cracking with plastic deformation around the crack tip.

Figure 4.36 (a-d) show sample T1. The test was performed in LBE with $6 \cdot 10^{-6}$ wt% oxygen amount. Test was stopped after rupture. Ground side (Figure 4.36c) shows more significant crack than polished (Figure 4.36b). The crack shape is sharper (Figure 4.36d) than in the air (Figure 4.35d), which indicates lower ductility. Still ductile deformation was observed around the crack tips on the edge of the specimen. The cracks were also concentrated around necking area.

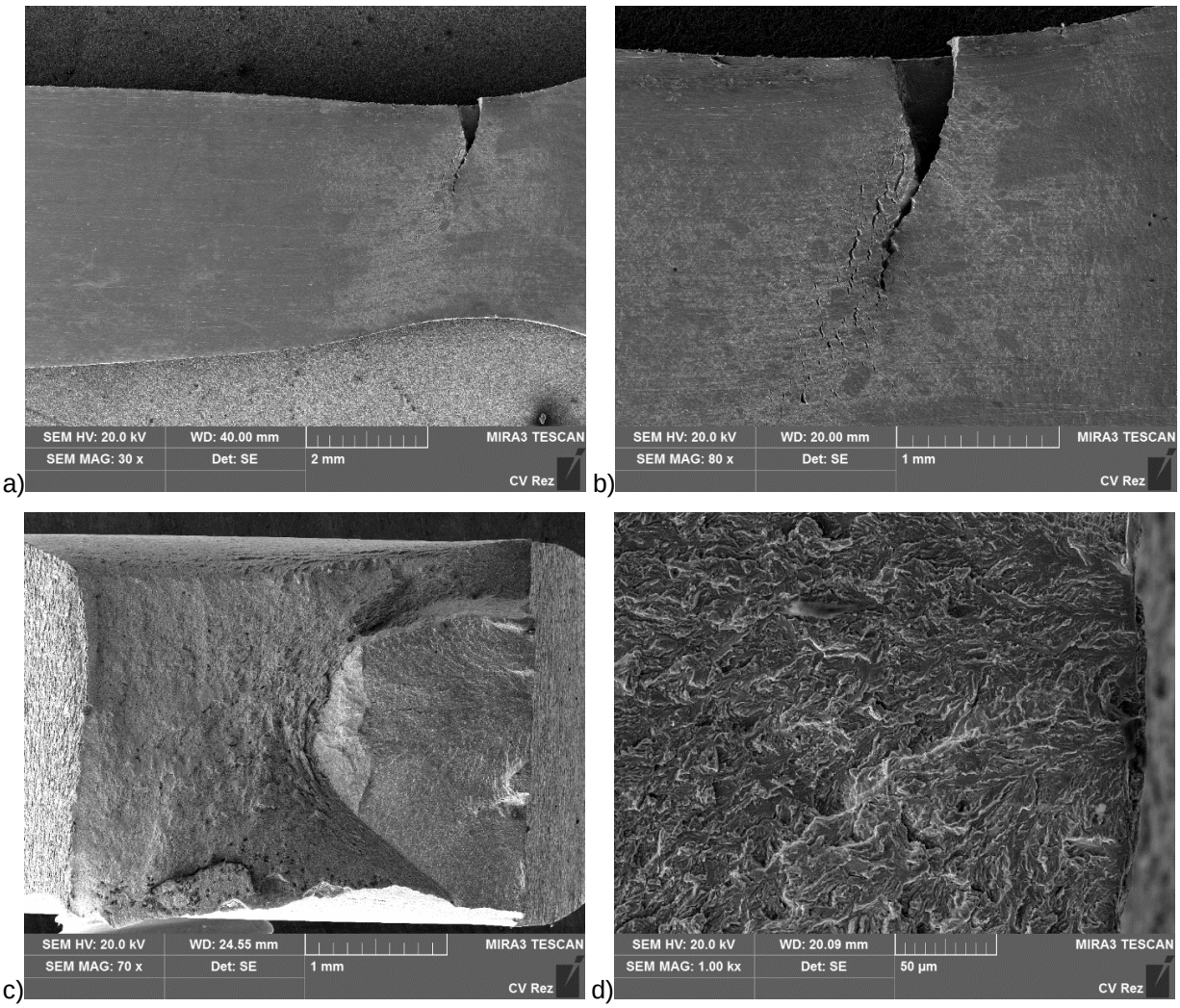


Figure 4.37: (a) T8, rupture (300 °C, LBE, $3 \cdot 10^{-13}$ wt% O), (b) detail on the main crack, ground side, (c) the crack area on the left side of the fracture surface, (d) detail, fracture initiation.

Figure 4.37(a-d) shows sample T8. The test was performed in LBE with $3 \cdot 10^{-13}$ wt% oxygen amount. Test was stopped after significant load drop which indicates rupture. However the total rupture has been done after test in air (room temperature) (Figure 4.37c). The specimen has one main crack and only small cracks occur near the rupture area (Figure 4.37b).

Ground side shows more significant cracking than the polished surface. The initiation is placed in the middle of the EDM side and the crack grows more toward to ground side (Figure 4.37c). The contrast between the ductile and the flat area is obvious from Figure 4.37(c).

Sample T9 tested in LBE with $10^{-8}$ wt% oxygen amount shows comparable results to T8 sample. The rupture was initiated from one main crack with small amount of micro-cracks around the necking area. Figure 4.33 shows similar plots for the samples T9 and T8.

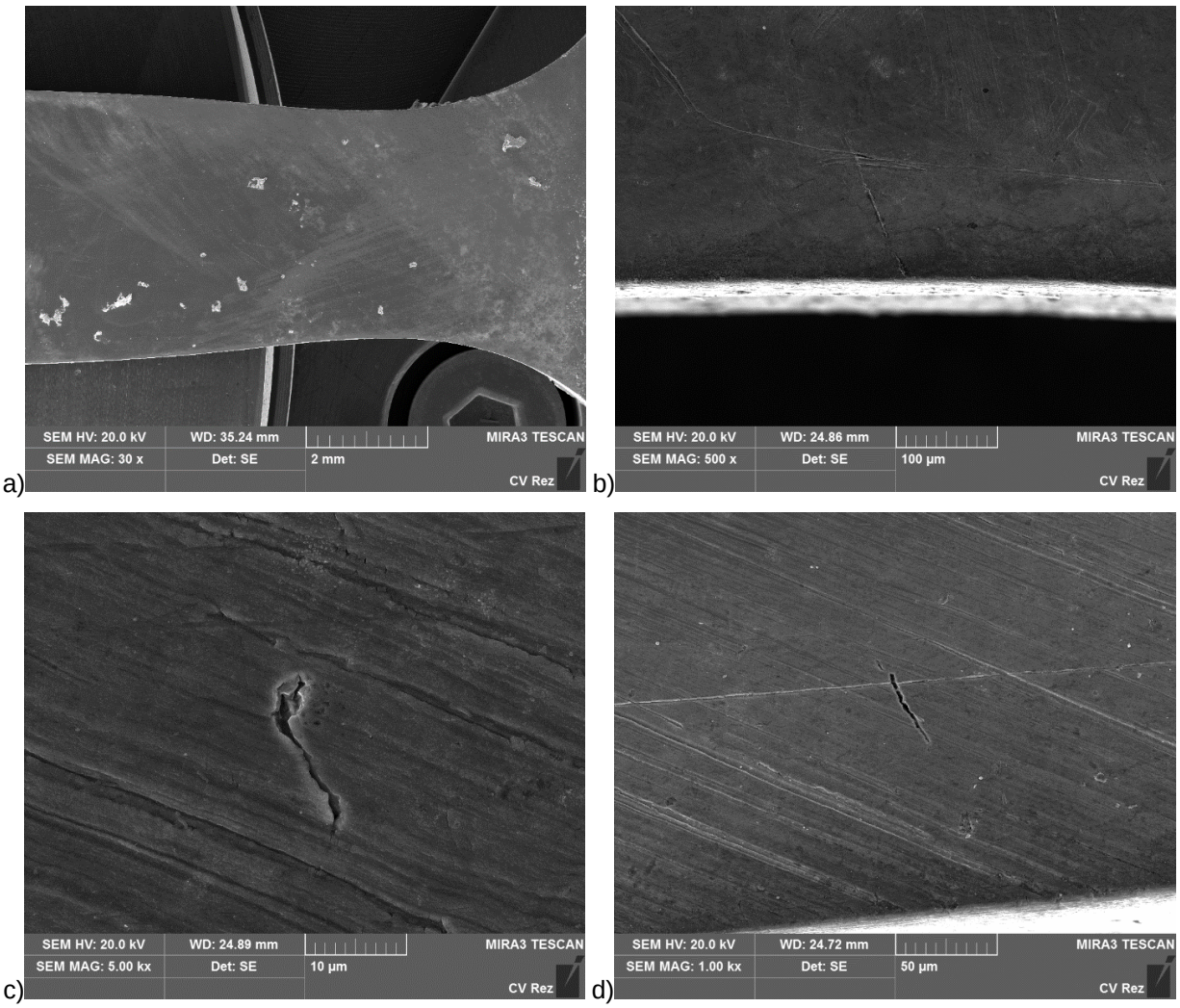


Figure 4.38: (a) T11 (300 °C, LBE, $c_o$=3·10$^{-7}$ wt%) UTS, (b) detail of the edge on the polished side – neck, (c) detail on the crack, ground side – neck, (d) detail, ground side – 2.8 mm from neck.

Several tests up to UTS were performed on T91 steel (in air and LBE). The area of necking shows only few negligible micro-cracks. The behavior of T91 steel is similar -for air and LBE. Specimens tested in LBE were in an environment with 2·10$^{-8}$ and 3·10$^{-7}$ wt% oxygen content.

The test results of T91 steel show crack growth after UTS. The influence of LBE- oxygen content on UTS is negligible, however the measured displacement of the specimens differs and it is decreasing with decreasing oxygen content. The results for specimens tested up to rupture in LBE with an oxygen content of 10$^{-8}$ to 10$^{-13}$ wt% show the same behavior. These results are similar to FCG results observed on CT specimens.

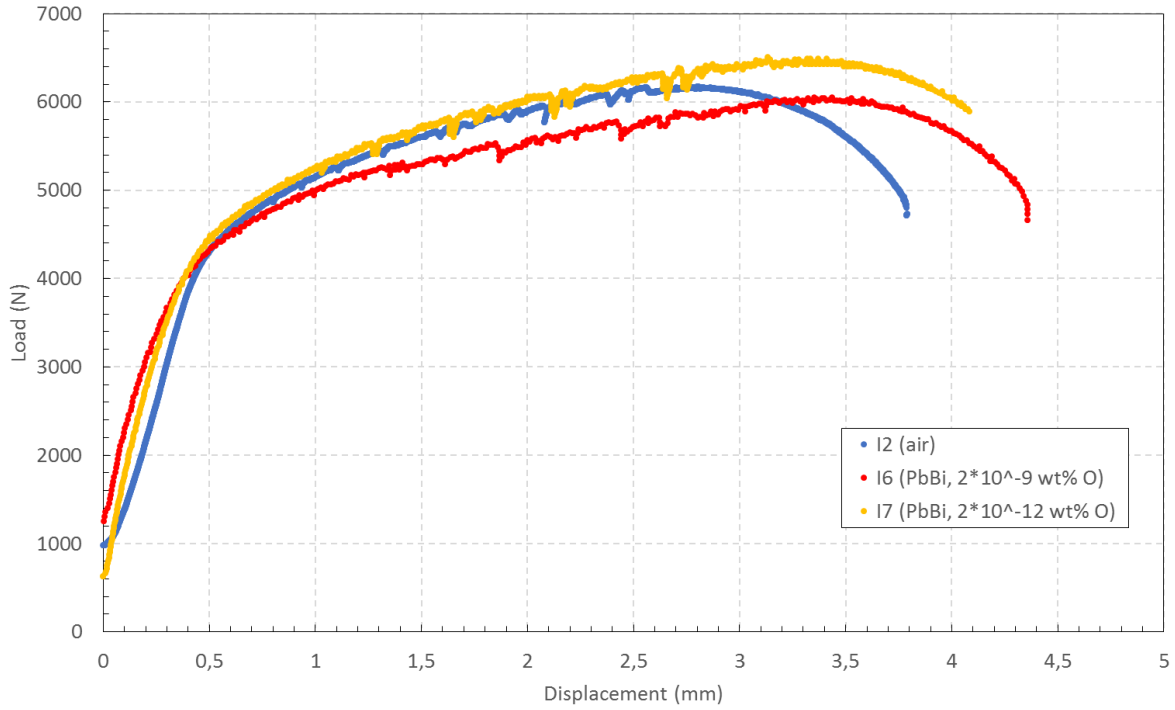


Figure 4.39: Comparison of load-displacement curves of 15-15Ti tapered specimens tested up to rupture at 300 °C.

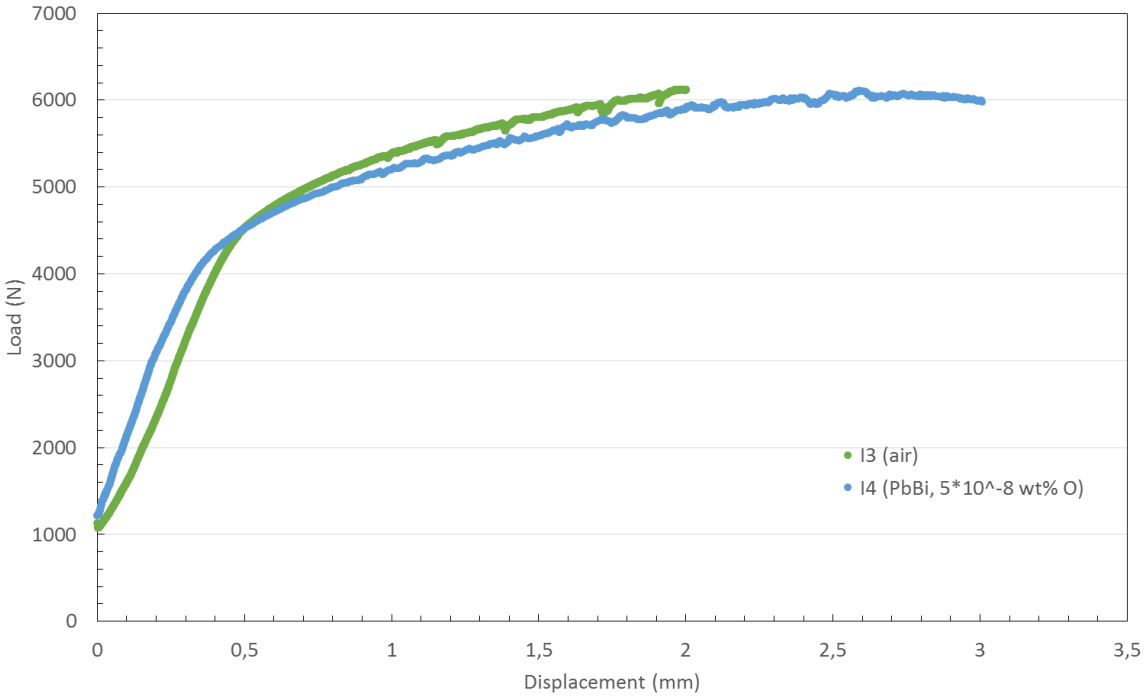


Figure 4.40: Comparison of load-displacement curves of 15-15Ti tapered specimens tested up to UTS at 300 °C.

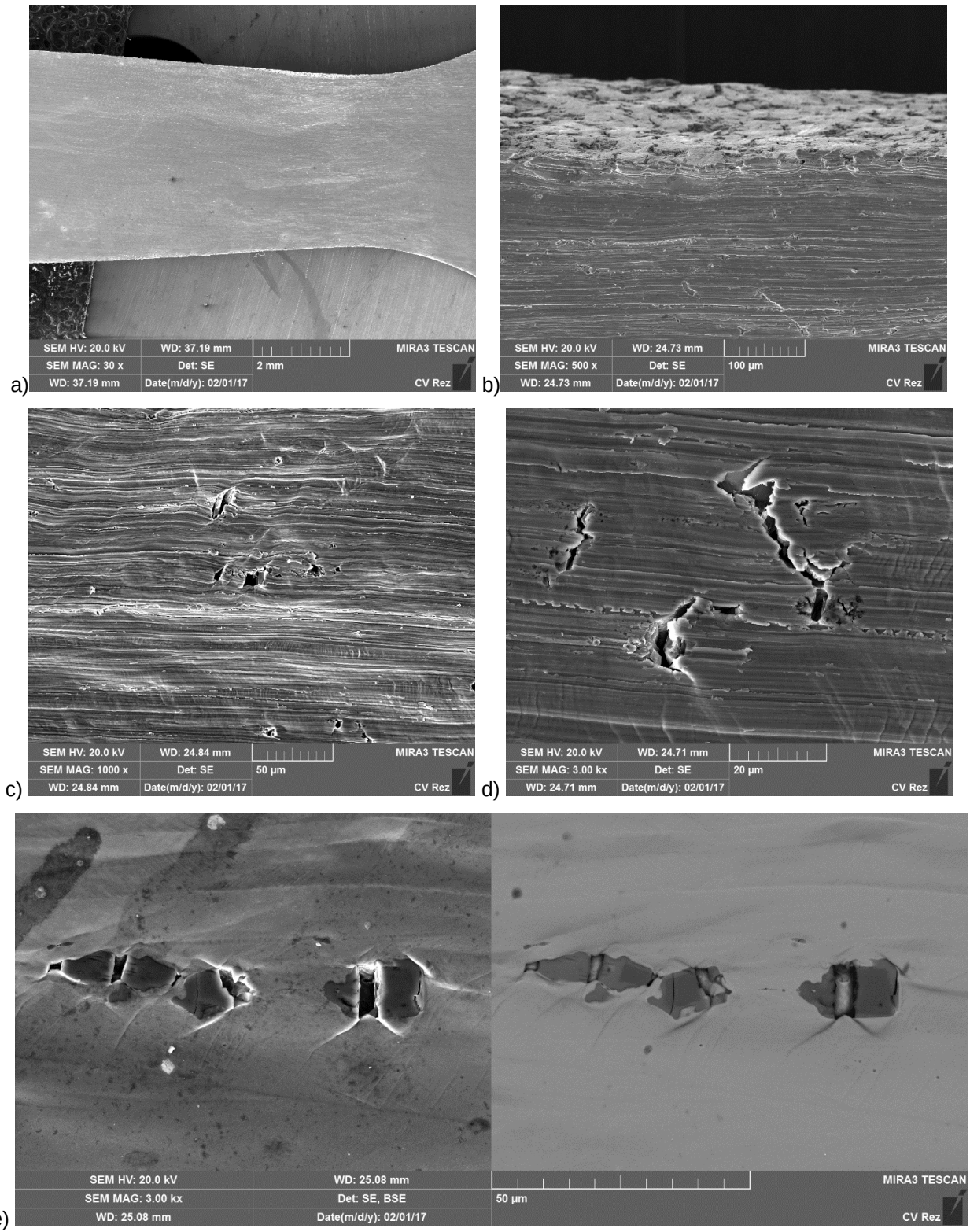


Figure 4.41: (a) I3 (300°C, air) UTS, (b) detail, ground-EDM edge. (c) detail, ground side - amid neck, (d) detail ground 3.48 mm from the neck, (e) detail, polished side – neck.

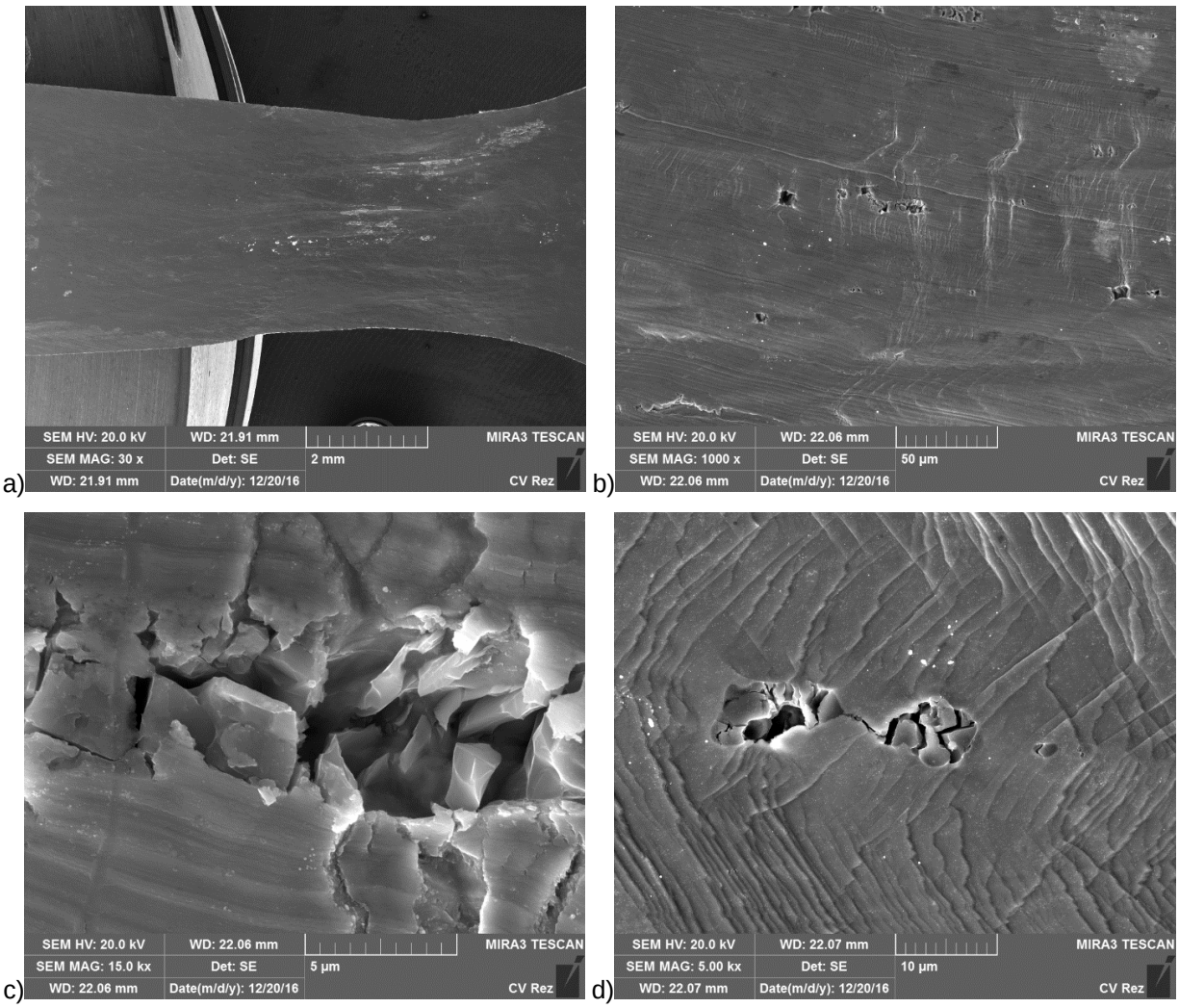


Figure 4.42: (a): I4 (300 °C, LBE, $5 \cdot 10^{-8}$ wt% O), UTS, (b) detail, ground side – neck, (c) detail, ground side – neck, (d) detail, polished side.

Figures 4.41 and 4.42 shows specimen surface of the steel 15-15Ti. The results of cracking were similar both for air and LBE. The test in LBE were performed with oxygen amount up to $2 \cdot 10^{-12}$ wt% and no embrittlement was observed. Several cracks (cavities) were observed on boundaries with Ti-carbides particles on specimens up to UTS and up to rupture too. The distribution of cavities is the same for all tested environments.

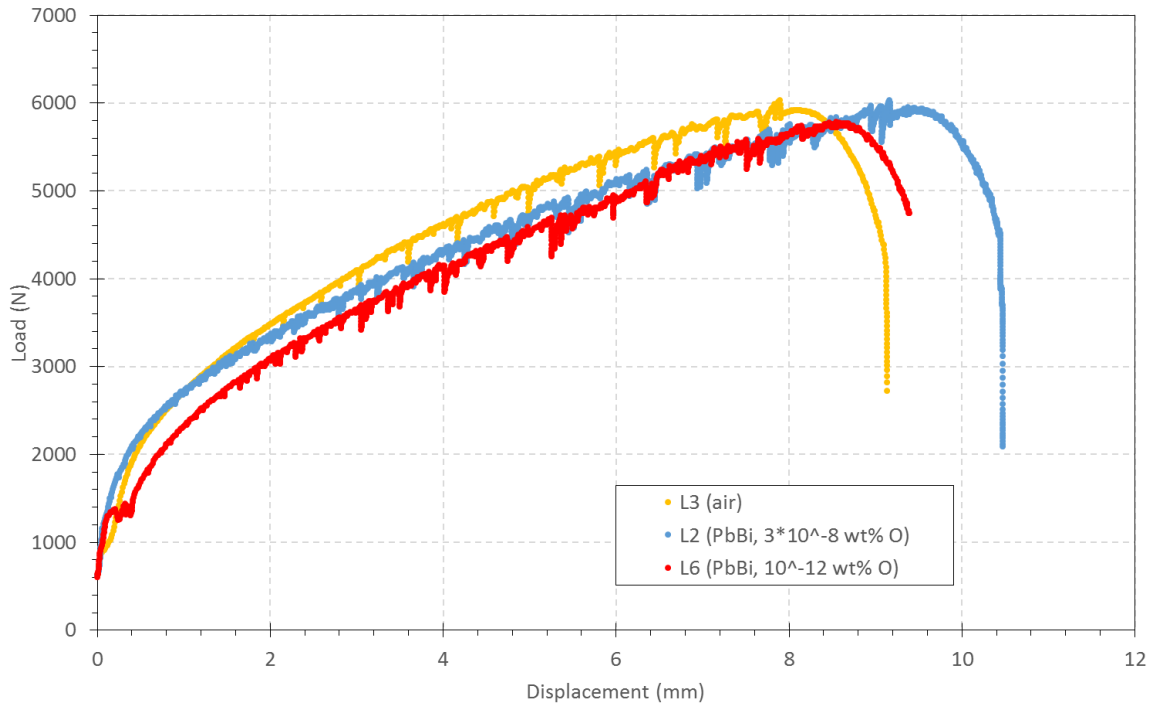


Figure 4.43: Comparison of load-displacement curves of 316L tapered specimens tested up to rupture at 300 °C.

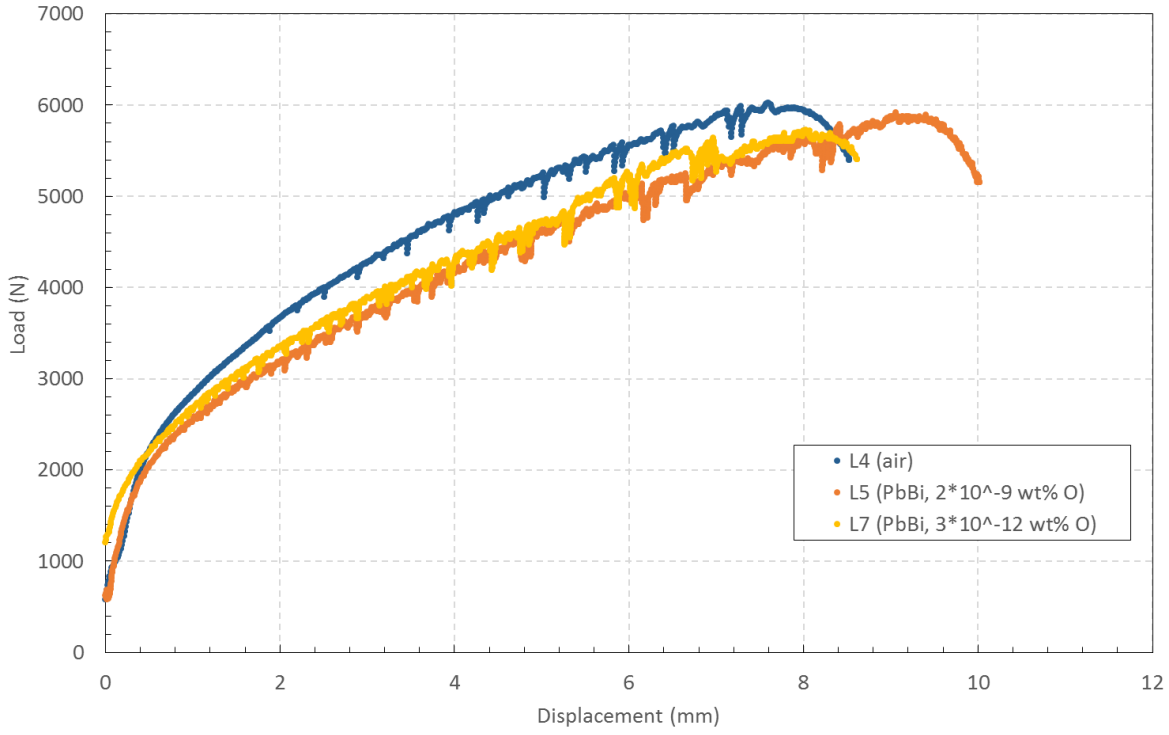


Figure 4.44: Comparison of load-displacement curves of 316L tapered specimens tested up to UTS at 300 °C.

a) 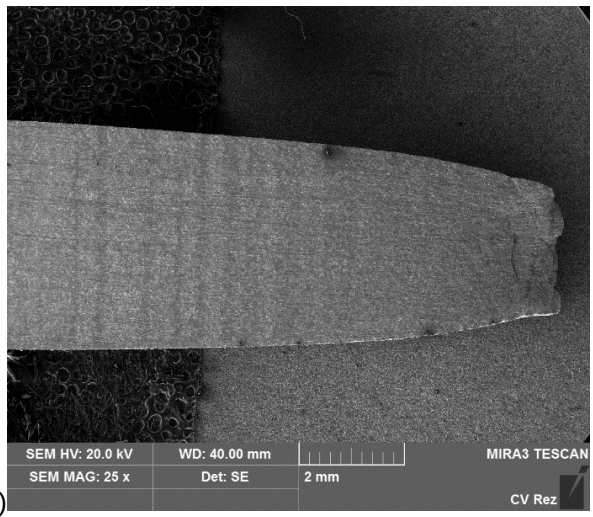

b) 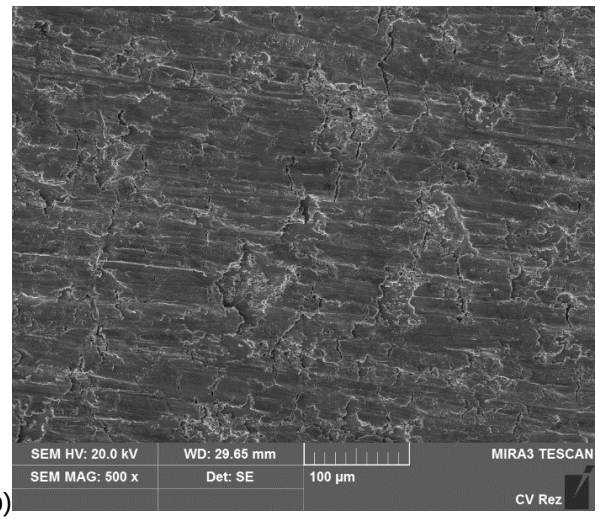


Figure 4.45: (a) L3 (300 °C, air), (b) detail on the necking, ground side.

a) 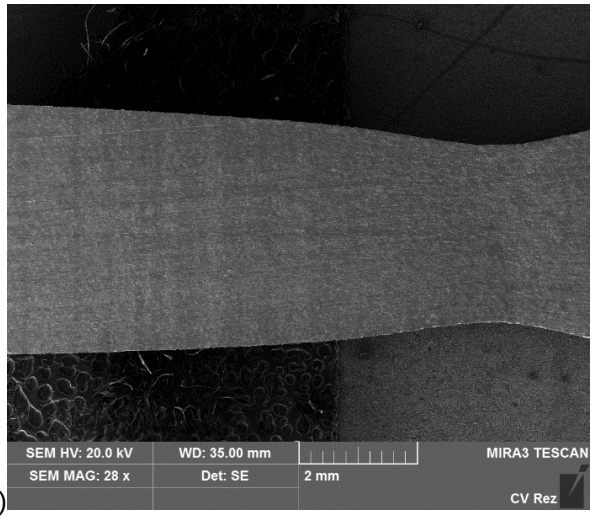

b) 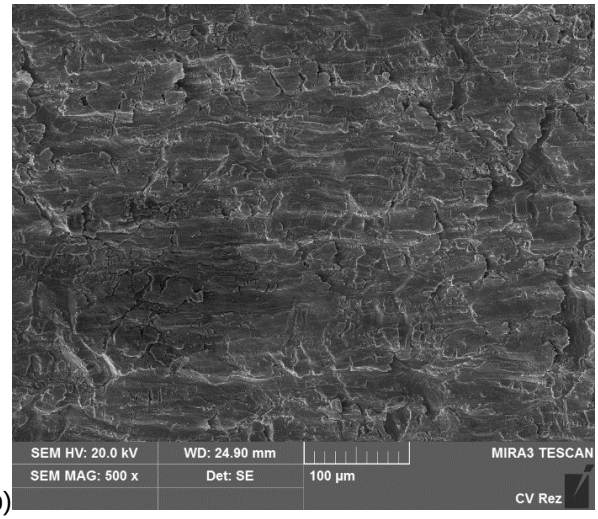


Figure 4.46: (a) L4 (300 °C, air), UTS, (b) detail on the necking, ground side.

Figures 4.45 and 4.46 shows 316L reference test in the air up to rupture and UTS. Material has ductile behavior with expected necking. Detailed views display first stadia of formatting ductile cracks in necking area.

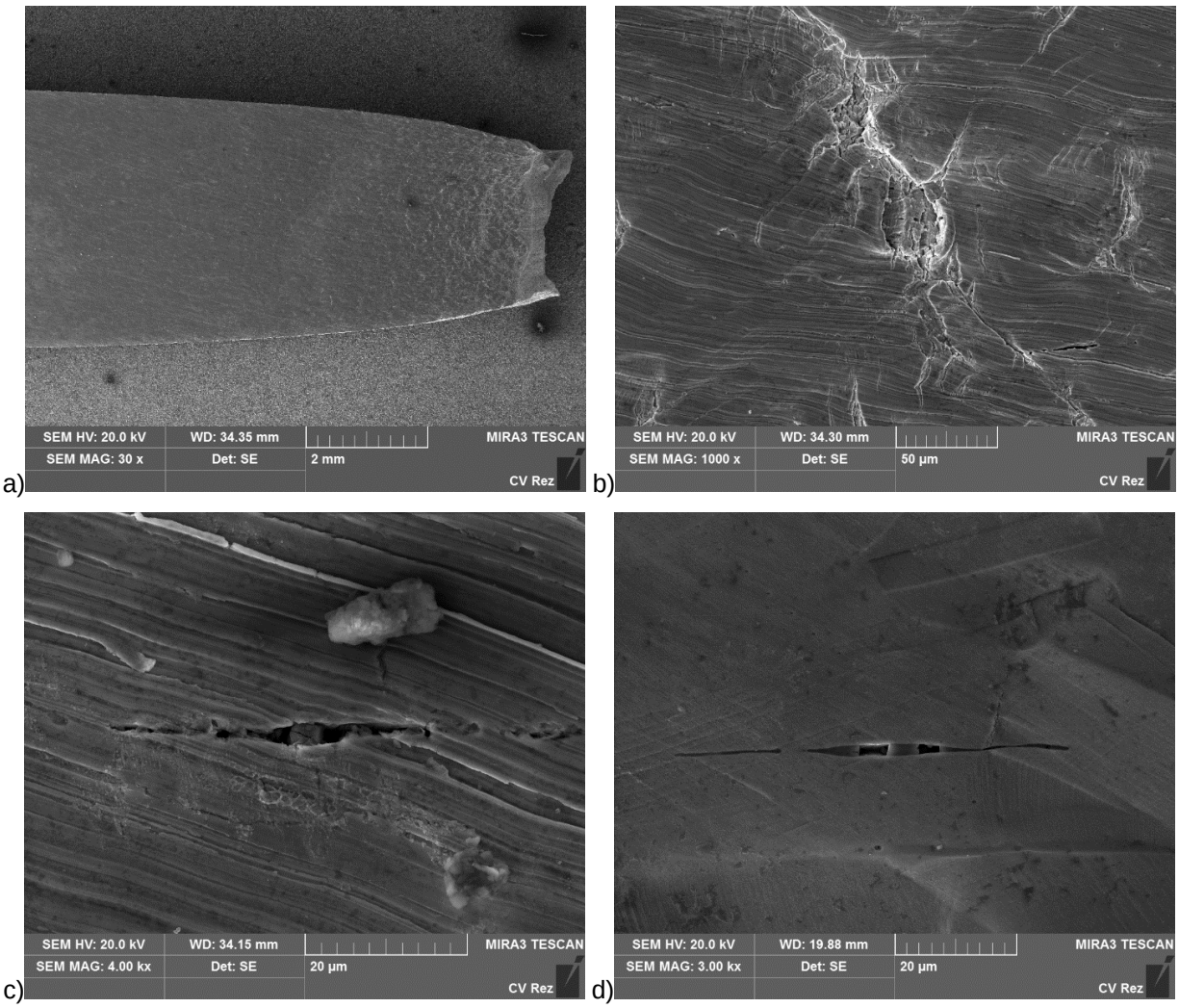


Figure 4.47: (a) L2 (300 °C, LBE, $3 \cdot 10^{-8}$ wt% O), (b) detail, ground side – 1.4 mm from the rupture (necking), (c) detail, ground side – 10.5 mm from the rupture, (d) detail, polished side.

Figure 4.47 (a-d) show sample L2. The test was performed in LBE with $3 \cdot 10^{-8}$ wt% oxygen amount. Test was stopped after rupture. Ground side shows more significant cracks than the polished side. Significant cracks (Figure 4.47 b) were observed on several places up to 5.75 mm from the rupture. Cracks in the axial direction were observed up to 10.5 mm from the rupture both on ground and polished sides. These cracks developed around Si rich, but there was no further investigation in the origin and composition of these particles.

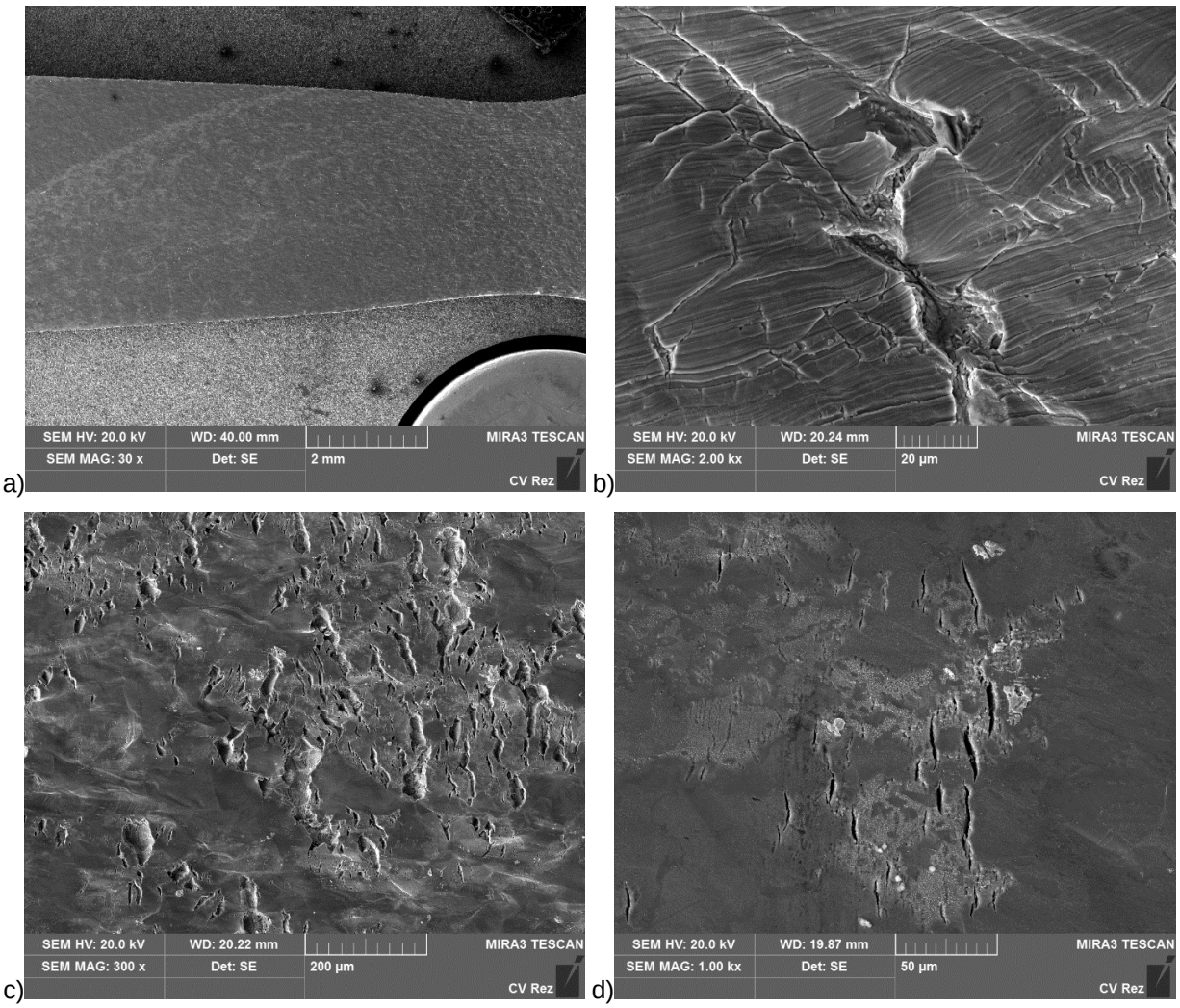


Figure 4.48: (a) L7 (300 °C, LBE, $3 \cdot 10^{-12}$ wt% O), UTS, (b) detail, ground side – neck, (c) detail polished side – neck, (d) detail, polished side – in the maximum distance.

Figure 4.48 (a-d) show sample L7. The test was performed in LBE with $3 \cdot 10^{-12}$ wt% oxygen amount. Test was stopped after UTS. Polished side shows more significant cracks than the ground side and these cracks can be observed on the whole specimen to the widest testing part. But the test was done in two parts, where the first part was unexpectedly stopped before UTS reaching and the second part of the test was reloaded. The reload was done at high deformation speed and was near the UTS limit, which caused crack initiation on the whole specimen. L6 sample was tested up to rupture in LBE with similar oxygen amount to L7 sample and ground side shows more cracks as expected. Maximum crack distance is 11.7 mm from the rupture.

The results from 316L stainless steel shows crack initiation before reaching the UTS. The influence of LBE and oxygen amount on UTS value is small, the measured displacement of the specimens differs and it is decreasing with lower oxygen amount. The results for specimens tested up to rupture in LBE with oxygen amount $10^{-8}$ to $10^{-12}$ wt% show similar behavior. Occasional cracks occur across the whole specimens which corresponds to low yield strength of the material.

## 4.4 Creep Tests

### 4.4.1 Creep Test at KIT

Original strain-vs.-time curves of 316L tested at 450-550°C in stagnant oxygen-controlled LBE and air show distinctive secondary and tertiary creep domains, while the primary creep domain is too short to be resolved, essentially for long-term-experiments (Figure 4.49). The steady-state creep rate, $\varepsilon_s$ and times corresponding to the transition (i) of primary to secondary creep, $t_{1,2}$, (ii) of secondary to tertiary creep, $t_{2,3}$, and rupture time, $t_R$, that belong to the set of creep-rupture data were identified from the original elongation/strain-vs.-time curves as described elsewhere [46]. All these parameters as well as strain at rupture, $\varepsilon_R$ and necking, $Z$ are presented in Table 4.3.

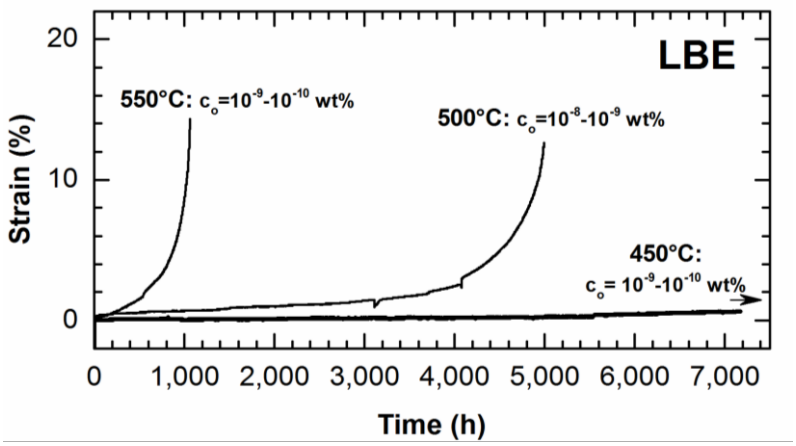


Figure 4.49: Strain-vs.-time curves obtained with 316L during creep(-to-rupture) testing in LBE at 450, 500 and 550°C and different oxygen content dissolved in liquid metal.

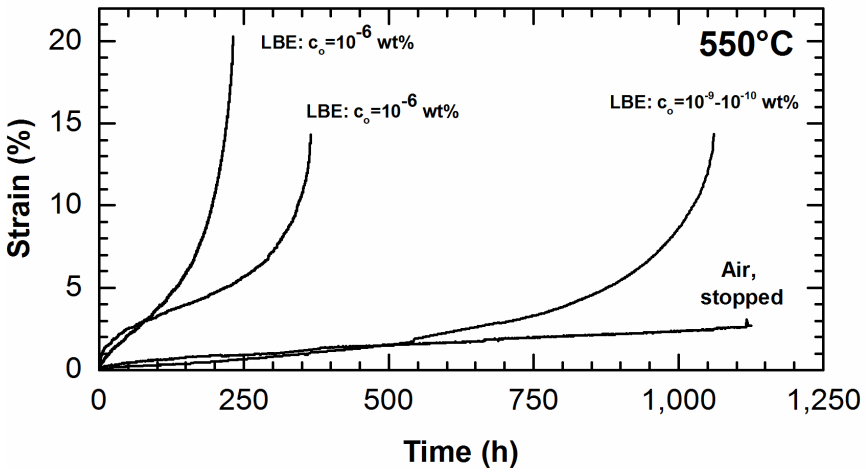


Figure 4.50: Strain-vs.-time curves obtained with 316L during creep(-to-rupture) testing in LBE with lowering oxygen content as well as $c_o=10^{-6}$ wt% and air at 550 °C.

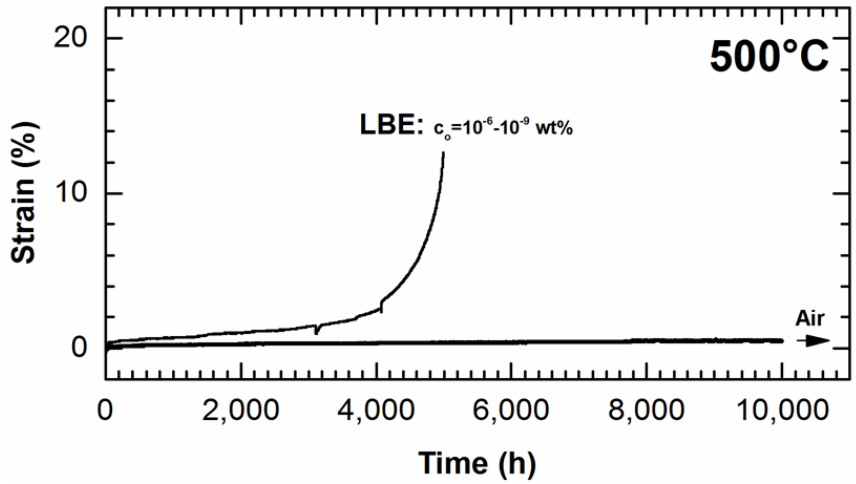


Figure 4.51: Strain-vs.-time curves obtained with 316L during creep(-to-rupture) testing in LBE with lowering oxygen content and air at 500 °C.

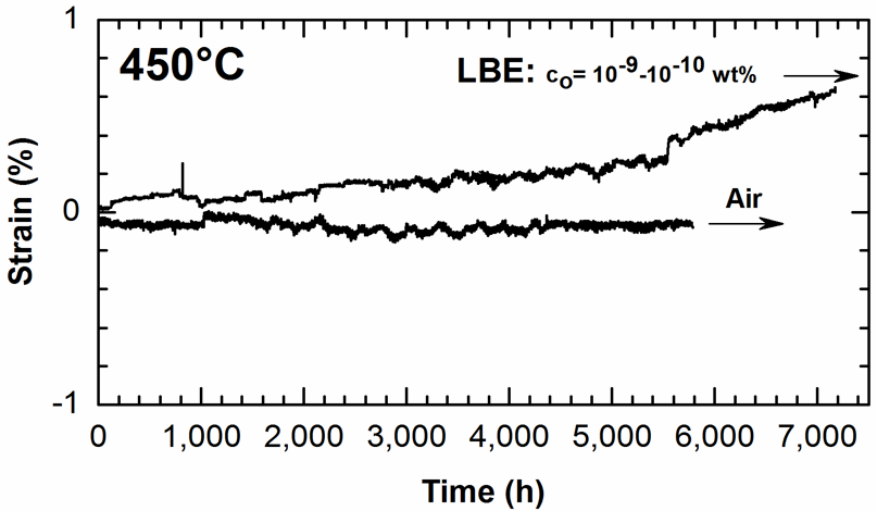


Figure 4.52: Strain-vs.-time curves obtained with 316L during creep(-to-rupture) testing in LBE with lowering oxygen content and air at 450 °C.

Table 4-3: Main creep-rupture characteristics obtained for the austenitic steel 316L tested in stagnant LBE (co ≤ $10^{-6}$ wt%) and in air at 450, 500 and 550°C.

| T, °C | Air | LBE/$c_o$, wt% | σ, MPa | $t_R$, h | $\varepsilon_R$, % | $Z$, % | $\dot{\varepsilon}_s$, %×$h^{-1}$ | $t_{1,2}$, h | $t_{2,3}$, h |
|---|---|---|---|---|---|---|---|---|---|
| 550 | | $10^{-9}$-$10^{-10}$ | 300 | 1,060 | 14 | 29 | $1.6\times10^{-3}$ | 34.9 | 155.9 |
| | | $10^{-6}$ | | 231 | 20 | 31.9 | $3.2\times10^{-2}$ | 19.6 | 111.8 |
| | | $10^{-6}$ | | 182 | - | - | - | - | - |
| | | $10^{-6}$ (i) | | 365 | 14 | - | $1.4\times10^{-2}$ | 70.9 | 188.6 |
| | Air (ii) | - | | >1.150 | >7.2 (iv) | >10.5 (iv) | $1.7\times10^{-3}$ | 382.0 | >1.150 |
| 500 | | $10^{-6}$-$10^{-9}$ | 325 | 5.025 | 18.5 | 43 | $3.1\times10^{-4}$ | 146.0 | 3162 |
| | Air (iii) | - | | >10,000 | - | - | $2.4\times10^{-5}$ | 88.0 | >10,000 |
| 450 | | $10^{-9}$-$10^{-10}$ (iii) | 375 | >4,630 | - | - | $3.5\times10^{-5}$ | 124.5 | - |
| | | - | | >3,265 | - | - | $1.1\times10^{-6}$ | ~0 | - |

(i) –the specimen was not cleaned from LBE after the creep-to-rupture test due to its specific microstructural study

(ii) – the creep(-to-rupture) test was stopped

(iii) – the creep(-to-rupture) test is still running

(iv) – creep characteristics after experiment was stopped and before the specimen was ruptured

Creep(-to-rupture) tests carried out in LBE at 450, 500, 550°C and different oxygen concentrations are presented in form of strain-vs.-time curves in Figure 4.49. An effect of the test temperature is clearly observed: the higher the temperature of LBE, the lower the time-to-rupture, $t_R$ of the steel was determined. It was expected that an increase of oxygen content in LBE at 550°C up to $c_o$=$10^{-6}$ wt% would lead to oxide scale formation on the austenitic steel and, therefore, to delay its degradation through steel elements dissolution. But the experiments showed no improvement of $t_R$ (Figure 4.50).

316L tested in LBE at all $c_o$ (≤$10^{-6}$ wt%) and elevated temperatures shows much shorter time-to-rupture, $t_R$ than in air (Figure 4.50 and Figure 4.51, Table 4.3) The creep test in air at 500 °C is running at least twice as long as $t_R$ was measured for 316L in LBE with low oxygen content (Figure 4.51).

The secondary creep rate, $\dot{\varepsilon}_s$ of the specimen tested in LBE at 550°C and $c_o$=$10^{-6}$ wt%, is one order of magnitude higher than in air (Table 4.3). But even when $\varepsilon_s$ of the steel tested in low oxygen containing LBE at 550°C and air are close to each other, the time that corresponds to the transition of secondary to tertiary creep, $t_{2,3}$, is much lower in LBE than in air and determines the time-to-rupture, $t_R$ in liquid metal. At 500 and 450 °C, the secondary creep rate is one order magnitude lower in air than in LBE with low oxygen content.

Preliminary results for strain at rupture, $\varepsilon_R$ and necking, $Z$ obtained for 316L tested in LBE at 550 and 500°C show that the strain at low oxygen concentration and both temperatures is in the $\varepsilon_R$-range at $c_o$=$10^{-6}$ wt% and 550°C, while $Z$ increases from 29-32% at 550°C to 43% at 500°C (Table 4.3). The steel crept in air at 550°C for 1,150 h (test was stopped before rupture) exhibits 7.2% strain and 10.5% necking. Comparing the strain-vs.-time curves that were obtained in air at all test temperatures before the specimens ruptured, it can be suggested that $\varepsilon_R$ and $Z$ will be significantly smaller after rupture.

## 4.5 Microstructural Investigations

### 4.5.1 Microstructural Investigations at KIT (after creep test)

Ductile fractures are generally characterized by tearing of metals accompanied by appreciable gross plastic deformation. The austenitic steel ruptured in LBE at 550 °C and 500 °C exhibits significant necking as well as a surface scale transformation independent on oxygen content (Figure 4.53 and Figure 4.54). Innumerable elongated dimples with their long axes in the direction of the shear force that are sign of the ductile fracture, are formed on the ruptured surface independently how complex topography of the failure is Figure 4.51a. It is very probable that the dimples originate by the nucleation and growth of micro-voids at secondary phase particles that were observed in as-received material (Figure 3.5 and Figure 3.6). Macroscopically the failure is

presented through shear-face fractures (at a 45° slant to the maximum tensile stress) that is a feature of the ductile fracture as well. Necking is visible through reduced cross-section area near the fracture surface. At lower test temperature, a more complicated fracture, *viz.* many shear planes ruptured at 45° to the stress direction were observed (Figures 4.53a and 4.54a,b).

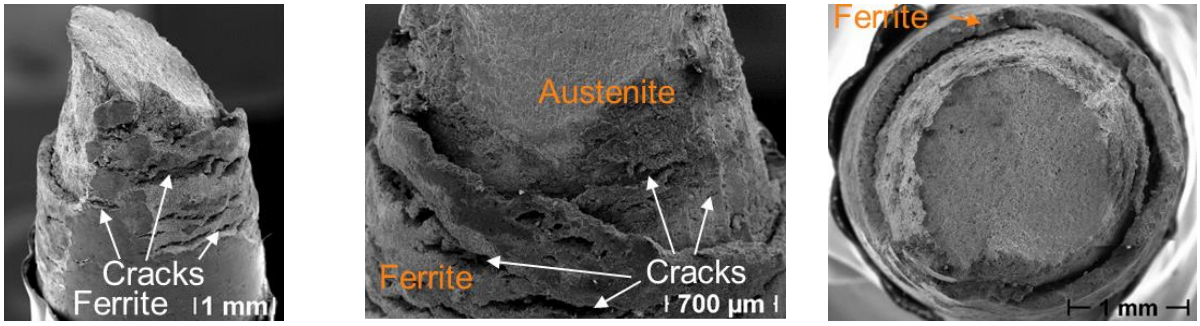


(a) (b) (c)

Figure 4.53: Failure of the austenitic steel 316L tested in LBE at 550°C and $c_o$=$10^{-7}$-$10^{-10}$ wt% for 1,060 h: (a) and (b) side view, (c) top view of the failure.

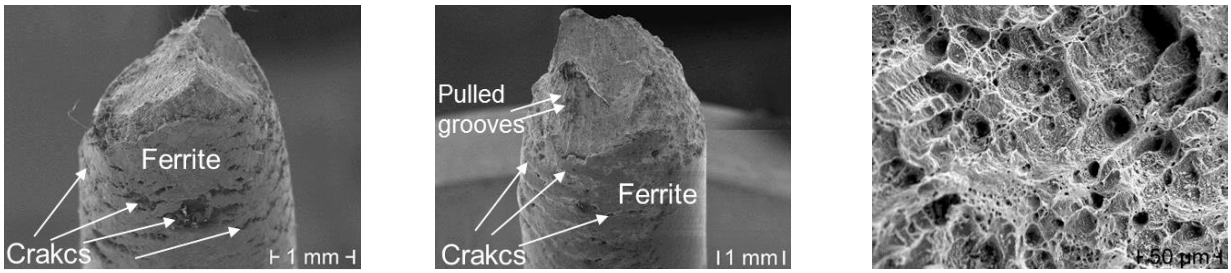


(a) (b) (c)

Figure 4.54: Failure of the austenitic steel 316L tested in LBE at: (a) 550°C and $c_o$ = $10^{-6}$ wt% for 182 h; (b) 500°C and $c_o$ = $10^{-8}$-$10^{-9}$ wt% for 5,025 h; (c) typical for ductile fracture dimples characterized failure surfaces of the ruptured 316L in LBE at 500 and 550°C.

Topographical study exhibits a new formed thick outer scale that exfoliated from the steel surface, while longitudinally pulled grooves are feature of the steel surface close to the failure (Figure 4.53). The outer scale is irregular in the length of the specimen with a tendency to disappear on the specimen the closer to the screw thread is (Figure 4.55).

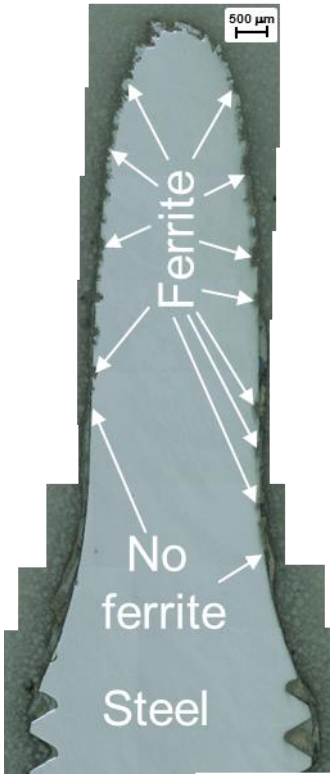


Figure 4.55: Longitudinal cross-section of 316L ruptured in LBE ($c_o$=$10^{-6}$ wt%) at 550°C after 231 h.

Austenite-ferrite transformation was observed after creep-to-rupture tests at 550 and 500°C independent on oxygen content in liquid metal. Typical elemental profile of ferrite layer formed on the surface of the austenitic steel 316L is presented in Figure 4.56. The concentration of Cr and Ni in the ferrite layer decreases in comparison to the steel matrix. Both concentrations decrease abruptly when crossing the interface between austenitic matrix and ferrite layer. Stepwise-like variation in the concentration of Pb and Bi in the ferrite layer indicates preferential penetration of liquid metal into ferrite along steel structural constituents (grain boundaries, sub-boundaries, twins) resulting in loosening of ferrite layer structure.

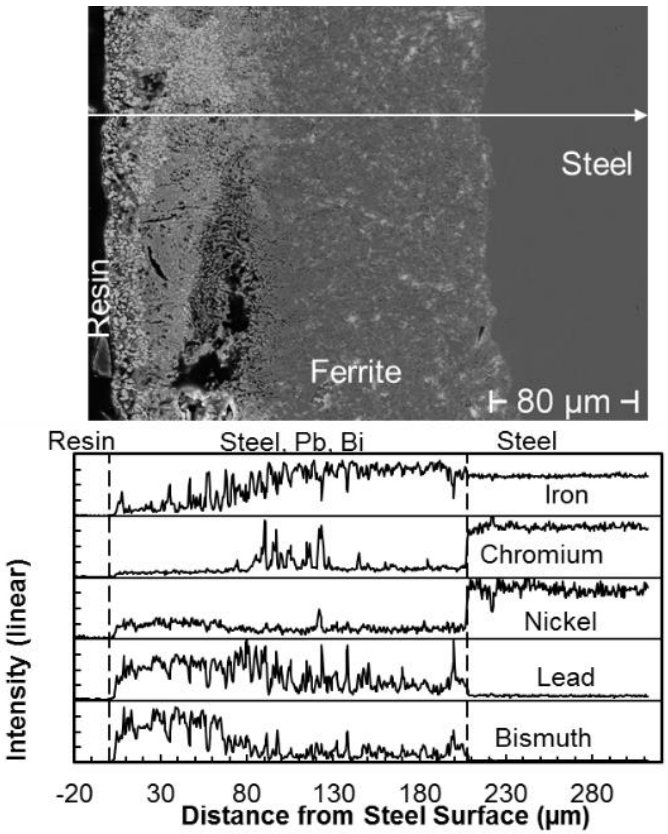


Figure 4.56: Elemental profile of ferrite layer formed on the surface of the austenitic steel 316L in static LBE at 550°C and $c_o=10^{-7}$ - $10^{-10}$ wt% during 1.060 h .

Against a background of general formation of oxides at $10^{-6}$ wt% oxygen dissolved in LBE at 550°C, no oxide layer(s) was observed on the austenitic surface. Some oxides were determined with EDX to form in the liquid metal close to the steel surface and at the austenitic steel/ferrite layer interface as well as in the ferrite layer itself (Figure 4.57a,b). One-time, a corrosion damage in the form of (Fe,Cr)-oxides formed in the steel along austenitic grain boundary was observed in the area close to the screw thread where ferrite scale was not formed (Figure 4.57c). Corrosion mechanism of the austenitic steel 316L is similar to that proposed for Ni-Cr alloys exposed to liquid Pb at 650 and 750°C [47]. Formation of thin oxide film on 316L in LBE at 550°C and $c_o=10^{-6}$ wt% is less stable to protect the steel surface from corrosion damages. If the austenitic surface close to screw thread is still free from ferrite and cracks, the rest of austenitic steel is damaged through selective-leaching attack and cracks formed under load (Figure 4.55). The ferrite layer grown irregularly has the deepest depth at places where cracks are filled with Pb-Bi (Figure 4.58a). Initial local damage of the thin oxide layer under load seems to be absolutely sufficient for initiation of local selective leaching of Ni and Cr directly from the steel area without oxide protective layer and from neighboring regions of sub-oxide layers. In the latter case, Ni and Cr from the neighboring areas do not diffuse directly though the oxide scale but are simply leached out by the liquid metal through the locally damaged film. Therefore, ferrite layer grows irregularly similarly to the case of exposition of 316L to LBE at 550°C and $c_o=10^{-7}$ wt% [48].

Additional damages of the steel in form of cracks that appear and prolong under stress affected by local stress: Closer to failure area, the amount of deeper cracks increases. The highest stress in the failure area has resulted in the cracks appearing under load only in the ferrite layer (Figure 4.53a, b and 4.55). These cracks that tip contacts directly the steel are filled with Pb-Bi (Figure 4.58a). Liquid LBE in the crack tip is depleted with oxygen that leads to activation of dissolution of the steel elements (Ni and Cr) at the contact area and therefore, to the more intensive degradation of the steel and its mechanical properties inclusive the creep strength. In comparison to our results, formation of layer-type corrosion damages as result of selective leaching attack (ferrite layer and initiation of local damage in the oxide film, i.e. pits) were observed without any traces of cracks on 316L exposed to flowing oxygen-containing LBE ($c_o=10^{-7}$ wt%) at 550°C (Figure 4.58b, used with permission of authors). Therefore, appearance of the cracks in the ferrite layer formed on 316L is a distinctive feature of the steel tested in LBE with oxygen content lower $10^{-6}$ wt% under load.

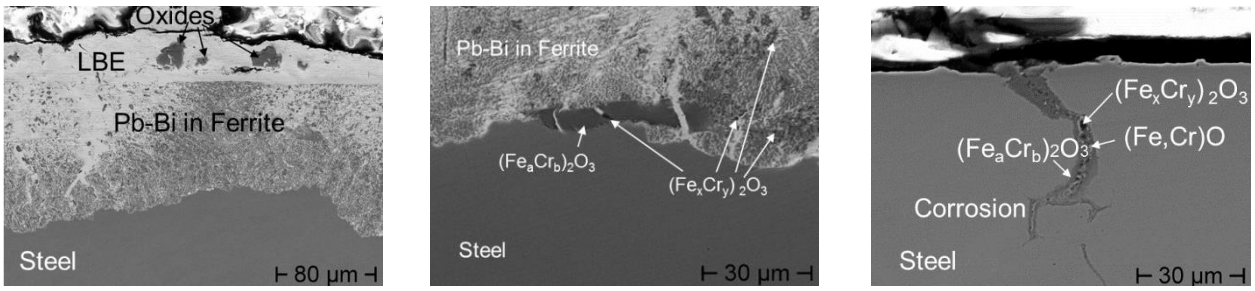


(a) (b) (c)

Figure 4.57: Perpendicular cross-section of 316L ruptured in LBE (co=10-6 wt%) at 550°C after 365 h. The specimen is not cleaned from the rest of LBE from the surface after creep-to-rupture test.

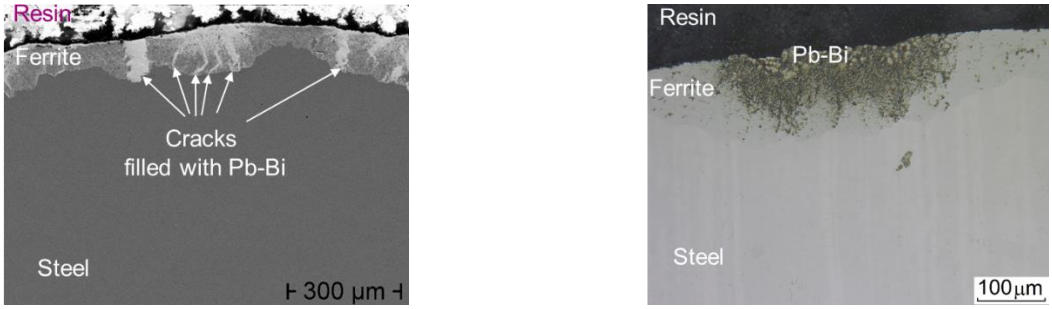


(a) (b)

Figure 4.58: Comparison of (longitudinal) cross-section of 316L crept in stagnant LBE (co=10-6 wt%) at 550°C after 231 h (a) and 316L exposed to flowing LBE (~2m/s, ~10-7 wt%) for 2,011 h at 550°C [49] (b).

A material loss of the austenitic steel under the test conditions may in general be a result of either oxidation or selective leaching. It was not possible to measure the thickness of oxide film since its thickness does not exceed ~0.5 µm at 500 and 550°C. The selective leaching attack is represented by a layer-type formation of ferrite zone.

Table 4-4 summarizes results of quantitative measurements of corrosion loss of the steel 316L depending on the temperature and oxygen content in liquid LBE. It is clear that corrosion loss of 316L increases expectedly with time and temperature rise. The thickness of the ferrite layer became more regular with time as it was observed for the steel at 500°C and 550°C and low $c_o$. So, after 1,060h at 550°C, when element diffusion is higher than at 500°C, and therefore ferrite has close thickness range at both temperatures with a tendency to slightly higher thickness at 550°C in comparison to the lower temperature. For shorter time-to-rupture at 550°C the ferrite layer was measured one order thinner. Formation of thicker ferrite layer after shorter $t_R$ (=325 h) and under the same further test conditions (at 550°C, $c_o=10^{-6}$ wt%) might originate that the cross-section investigated was cut from the area closer to the failure and/or the results of the ferrite thickness for both specimens might lie with a scattering range.

Table 4-4: Thickness of ferrite layer measured on the perpendicular cross-sections of 316L after creep-to-rupture tests in LBE at $c_o \leq 10^{-6}$ wt% and 550°C as well as 500°C.

| T, °C | $c_o$, wt% | σ, MPa | $t_R$, h | Thickness of ferrite, µm |
|---|---|---|---|---|
| | $10^{-9}$-$10^{-10}$ | | 1,060 | 79-220 |
| 550 | $10^{-6}$ | 300 | 231 | 0-86 |
| | $10^{-6}$ | | 325 | 0-37 |
| 500 | $10^{-8}$-$10^{-11}$ | 325 | 5,025 | 93-200 |

### 4.5.2 Microstructural Investigations at CNRS (after fatigue test)

The evolutions of the microstructure along the crack lips were analyses by SEM EBSD after tests in air and in oxygen saturated LBE at $\Delta\varepsilon_t$ = 1.2%. This reflects the evolution of the crack tip before the crack advance.

For that, after tests, transversal cuts of the specimen were done and the cut surfaces were carefully polished.

After test in air, a continuous raw of very fine and highly misoriented grains which size ranged from 0.2 µm to 0.5 µm was observed in the material at the surface of the crack.

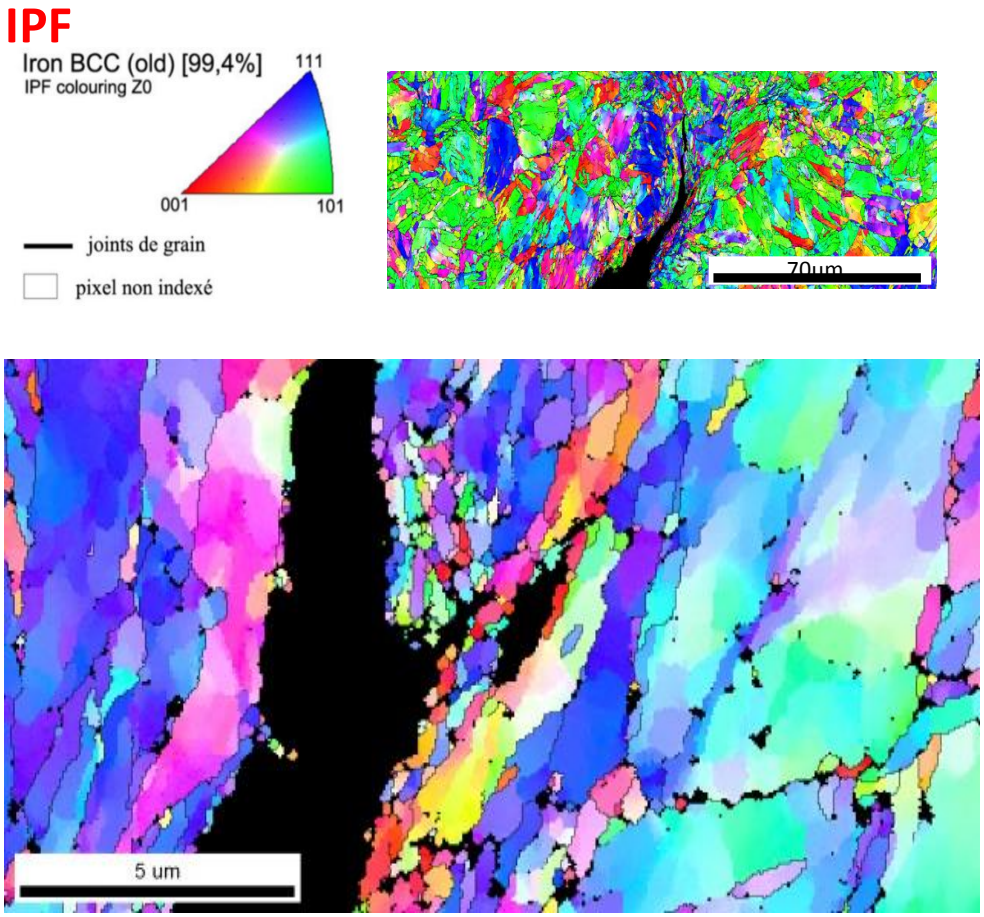


Figure 4.59: EBSD map of crack tip advance in T91 (fatigue test, air, 350 °C).

After test in oxygen saturated LBE, the crack lips were not decorated by the continuous raw of very fine and highly misoriented grains. Some fine grains packets were indeed observed but at some places of the crack lips.

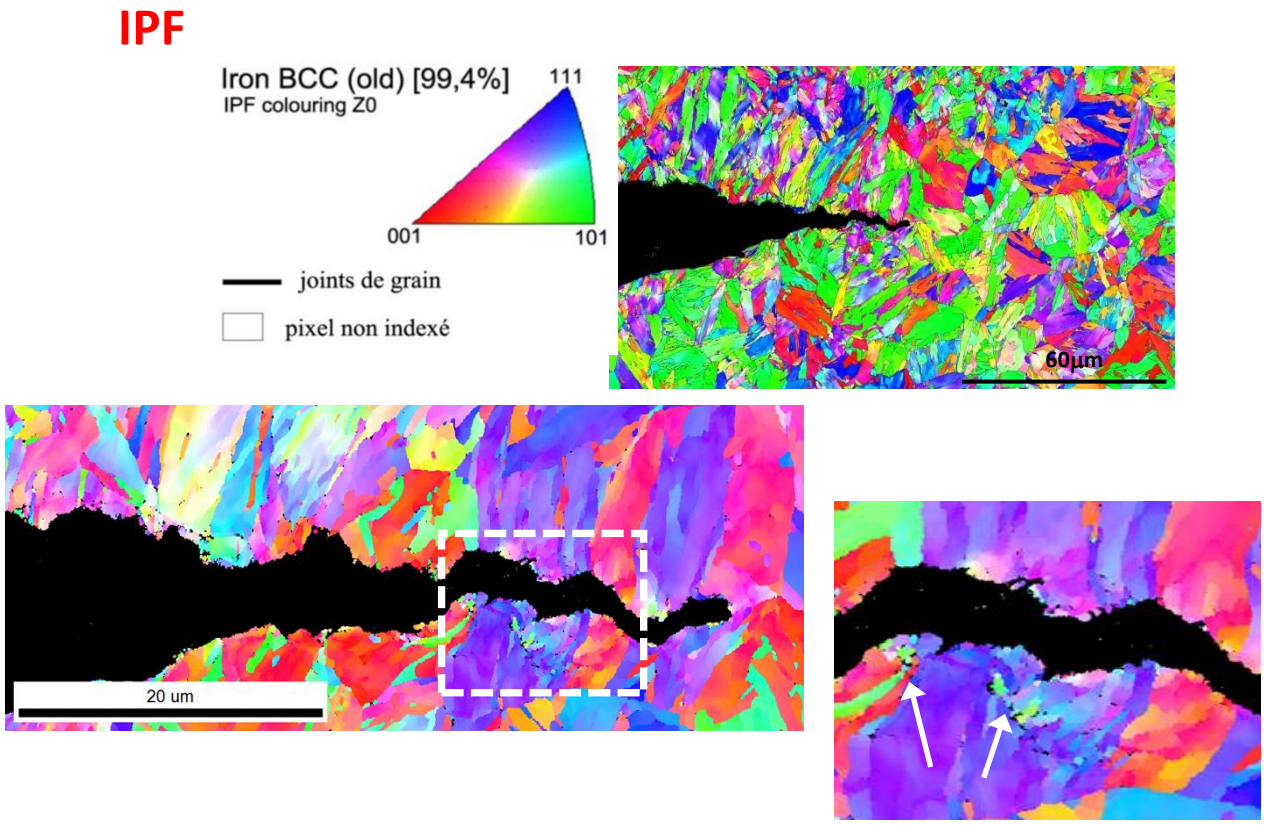


Figure 4.60: EBSD map of crack tip advance in T91 (fatigue test, LBE, 350 °C).

Additional analysis showed that the fine grains packets spacing was smaller than the distance between striations. It means that they are not the marks of the striations

In the present study, fatigue in air resulted in fatigue crack propagation by a classical mechanism. The plastic zone was large suggesting activity of dislocations from a big volume of material. On the other hand, the plastic zone was very restricted in test in saturated oxygen or low oxygen LBE and the material was not very plasticized.

The crack tip was blunted after test in air while it was very sharp in LBE.

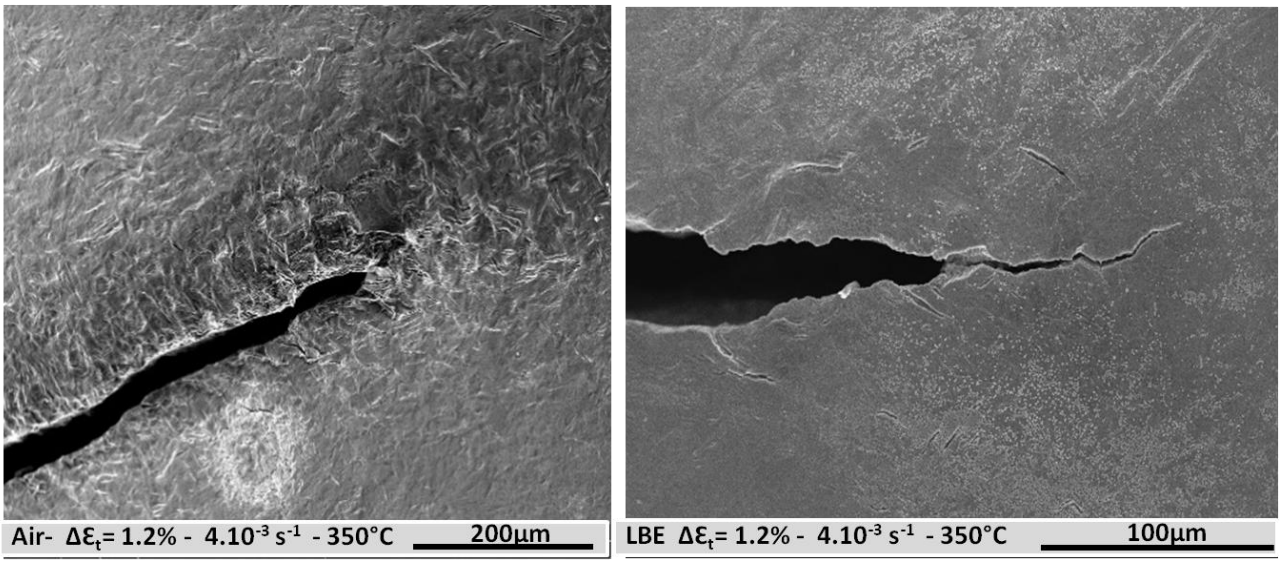


Figure 4.61: Comparing of crack tip shape – air vs LBE (T91, fatigue test, 350 °C).

The continuous raw of fine grains in the material fatigued in air may be explained by the high cyclic deformation localized in a small region at the crack tip. In the present case, the very first laths just ahead the crack tip are supposed to be highly strained which lead to dynamic recristallization.

For the test performed in LBE, when the microcrack was formed by fatigue, the adsorption of Pb or/and Bi atoms reduces the local stress intensity factor which may propagate the microcrack by cleavage. During a loading phase, the crack quickly advances in a brittle manner till the atoms of the liquid metal are in contact with the crack tip. If the atoms of the liquid metal are no more in real contact because oxidation occurred temporally or because of absence of liquid metal as capillarity effect, then the crack by cleavage advance stops temporally and then restarts when the required conditions are obtained.

### 4.5.3 Microstructural Investigations at SCK-CEN (after fatigue test)

In Figure 4.62 and Figure 4.63, EBSD investigations of the vicinity of fracture surfaces of fatigue samples tested in vacuum and LBE are shown. A comparison of the fatigue crack walls shows significant differences. Fatigue laths close to the crack walls have been transformed into very fine subgrains in case of tests in vacuum. The mean grain size of these grains can be estimated with 500 nm. In regions far from the fracture surfaces no refinement of the grains could be identified. The formation of these subgrains can be related to intense plastic deformation and recrystallization in the vicinity of the crack tip. In contrast to tests in vacuum no strong grain refinement around the crack can be identified for samples tested in LBE (Figure 4.63). Because of the absence of grain refinement the shape of split martensite laths can still be identified. This suggests that plastic deformation around the fatigue crack in the presence of LME is limited. For more detail please see Gong et al. [44].

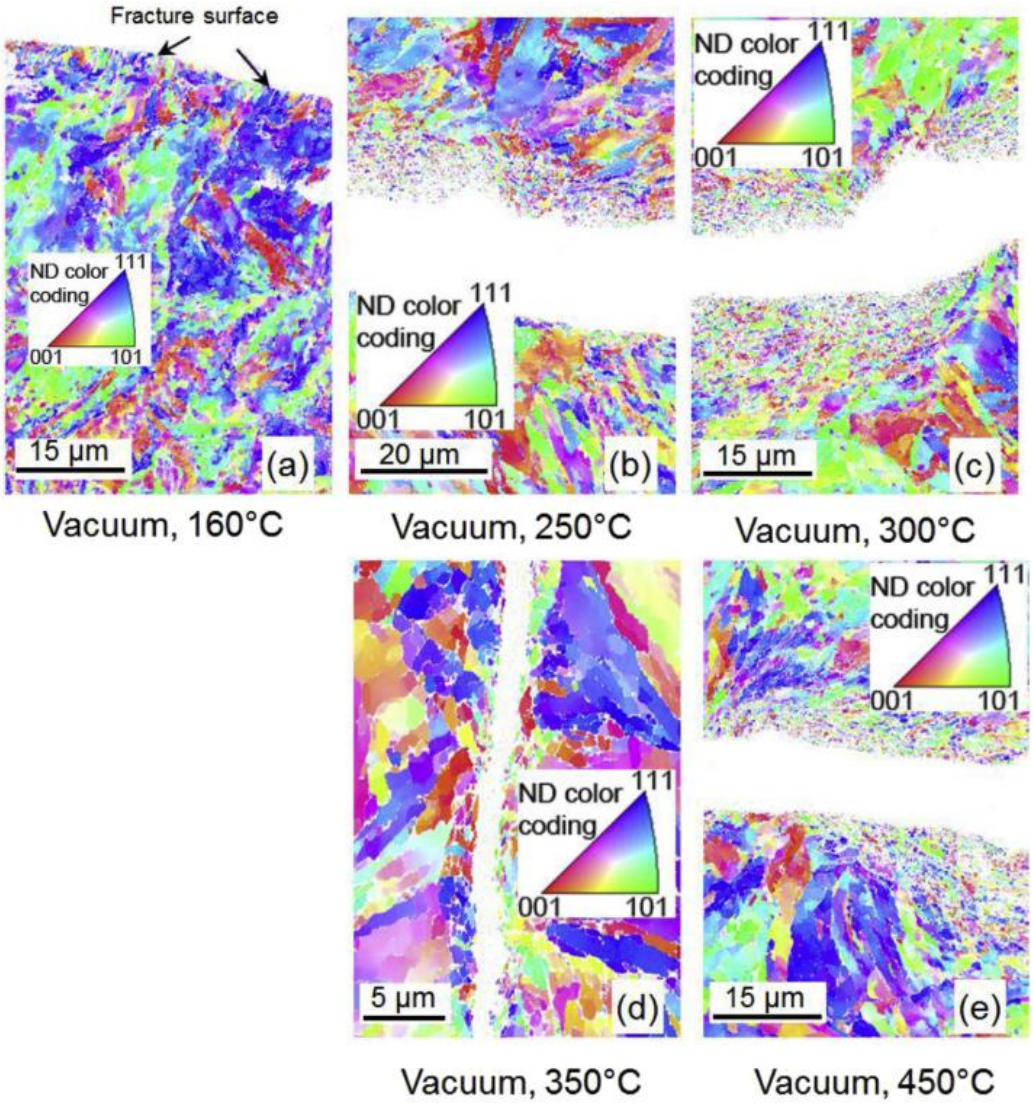


Figure 4.62: EBSD orientation maps showing the vicinity of fatigue cracks tested at different temperatures in vacuum [44].

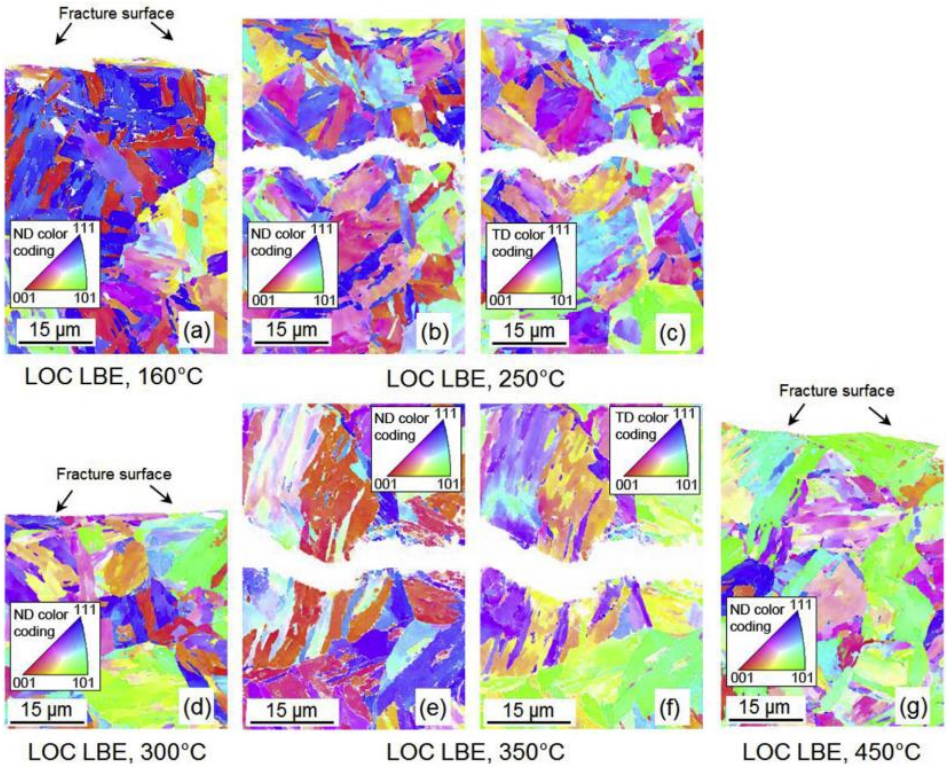


Figure 4.63: EBSD orientation maps showing the fatigue crack vicinity of samples tested at different temperatures in LBE [44]

### 4.5.4 Microstructural Investigations at CNRS MSSMat (after crack propagation)

The reference specimen (CT-sample 1) was pre-cracked by fatigue in Ar and then the crack was propagated in the ductile regime in Ar-5%$H_2$ at 350°C. In order to end the test, it was further cracked in liquid nitrogen. This sample gave the opportunity to analyze in some details the crack path in the intrinsic brittleness range at low temperature. The transverse cut on sample 1 revealed numerous secondary cracks. Some of them where connected to the main crack as can be seen in Figure 4.64a. Others were internal cracks that did not connect with the main crack, at least in this two-dimensional cross-section. Several EBSD orientation mapping of the microstructure surrounding secondary cracks were carried out with a fine step grid (50 nm). The one corresponding to Figure 4.64a is shown in Figure 4.64b and Figure 4.64c. The interlath character of the crack is obvious here. The internal cracks that where analyzed had no or a small disorientation between the lips of the crack which is typical of cleavage fracture. Therefore, a mixture of interlath and cleavage fracture was observed for fracture at liquid nitrogen temperature.

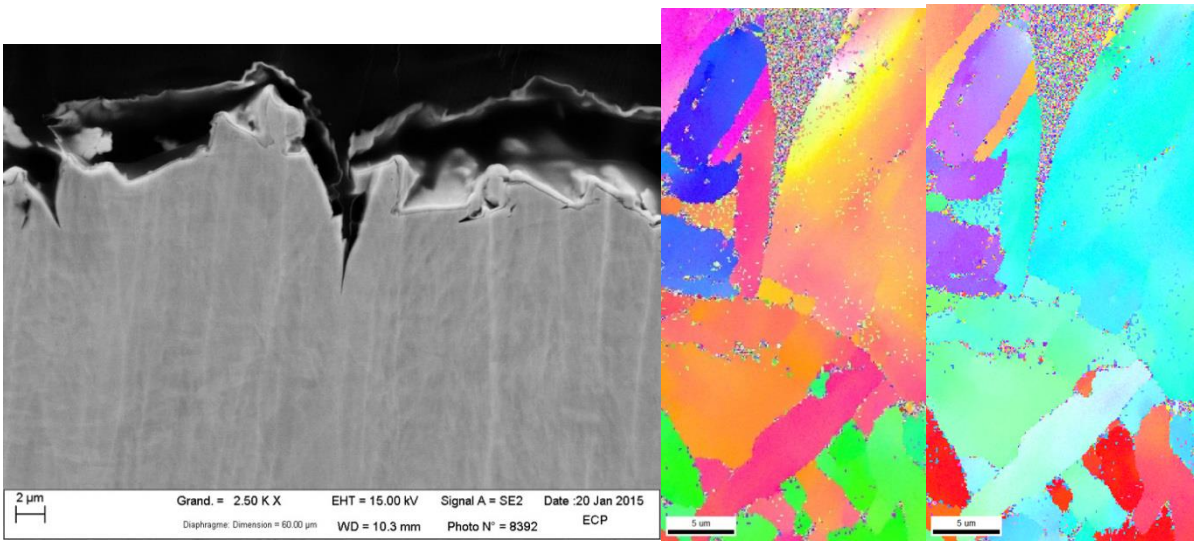


Figure 4.64: a) SEM view of the liquid nitrogen cracked area from Sample 1 b) EBSD mapping

The transverse cut in the pre-cracked area with LBE (CT-sample 2) revealed many secondary cracks as well. The pre-cracking being done by fatigue the main crack has a macroscopic wavy trajectory. The EBSD analysis carried out in the surroundings of several of them revealed that they clearly all had an interlath path as can be seen for example in Figure 4.65a and Figure 4.65b.

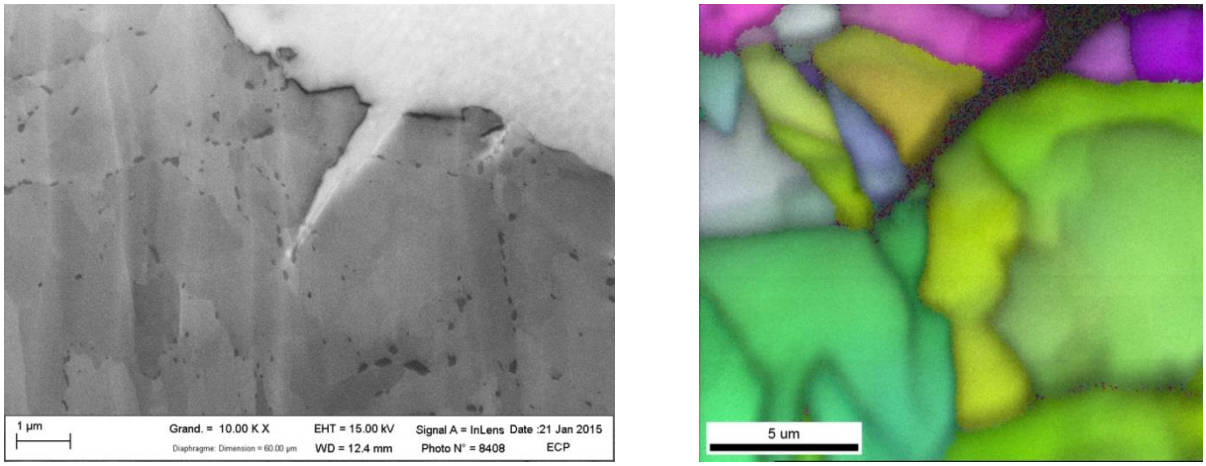


(a) (b)

Figure 4.65: a) SEM view of the cut in the pre-cracking area from Sample 2 (pre-cracked in LBE) b) orientation mapping by EBSD of the area.

In the CT-sample 2, multi-cracking pattern can also be observed in several areas. The EBSD analysis (not shown here) indicates that large chunks of grains were separated by intergranular decohesion in the pre-cracked area. Therefore, pre-cracking by fatigue in LBE proceeds by interlath and intergranular cracking as a main crack propagation mechanism.

The CT-sample 3 was pre-cracked and tested in LBE. It is therefore the characteristic sample of such highly demanding fracture mechanics test. The transverse cut of CT-sample 3 in the crack propagation part is shown in Figure 3.24. One can see many secondary cracks emanating from the primary crack. They are all filled with LBE up to the crack tip. It illustrates the success of pre-cracking in LBE in place of a pre-wetting treatment because it then provides the right conditions for proper LME testing. The EBSD analysis of two of these cracks are shown in Figure 4.66 and Figure 4.67. The crack path is interlath in the two examples shown although the analysis is not as easily carried out than with sample 2. The difference in orientation color code is small so it may not be easy to rationalize the slight change in orientation using a color code. Indeed, the martensitic variants are distributed following the $(111)_\gamma//(011)_\alpha$ Kurdjumov-Sachs relationship between parent orientation of the austenite. For one variant, there can be a small spread of final orientations (a few degrees) that reflects

the symmetries of the martensitic pathway. One has to take this into account as well as the crack opening angle that opens during loading. This was carried out in the analysis of the secondary cracks of sample 3 (Figure 4.66 and Figure 4.67).

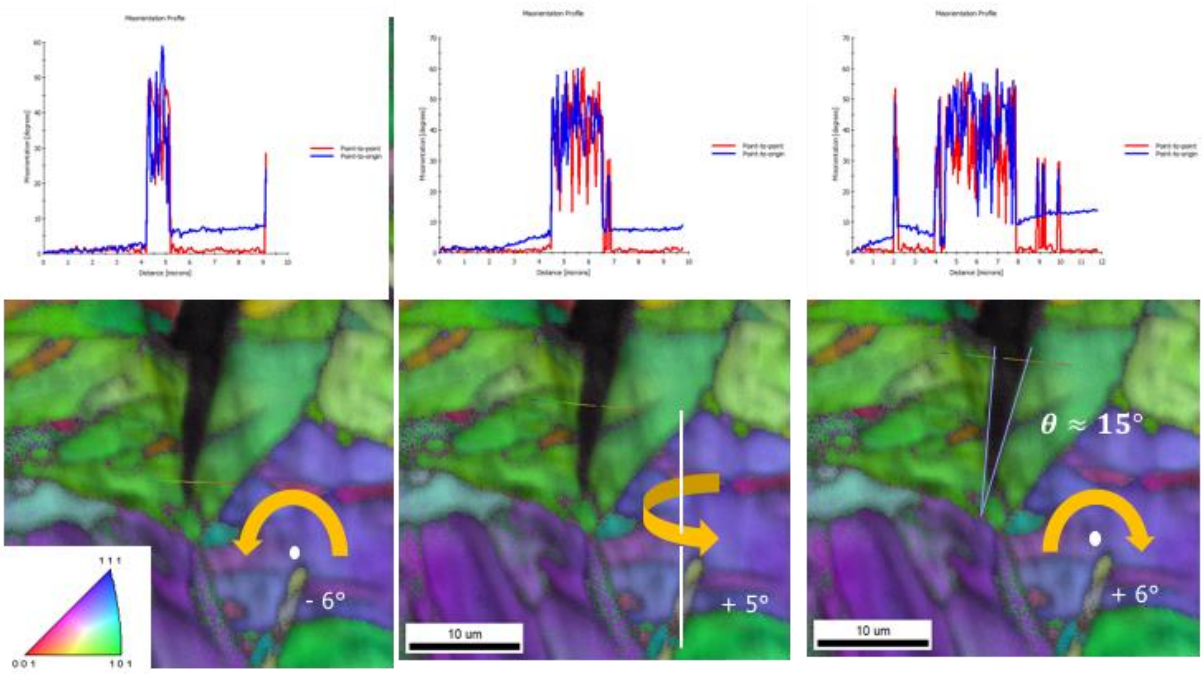


Figure 4.66: Orientation mapping by EBSD of the area, line profiles and rotations on the lips of the crack: a) near the crack tip b) in the middle part of the crack above the previous one c) away from the crack tip.

Misorientations plots (Figure 4.66) show small values of orientation change across the lips of the crack (as opposed to large values typical of general grain boundaries). If the fracture mode was cleavage, then there should be only one rotation angle required to bring all the orientations from one side of the crack to the corresponding one on the other side. The rotations were characterized along the two sides of the cracks on several locations. The equivalent rotation axis varies strongly from place to place with an axis that is not oriented transversely on several places. This can be seen in the Figure 4.66 and 4.67 where the rotation axis is shown at different places along the crack. It rules out a cleavage fracture mode that instead would have given a unique rotation for every path crossing the crack. Indeed, these rotations where present before cracking and so belong to interlath variants.

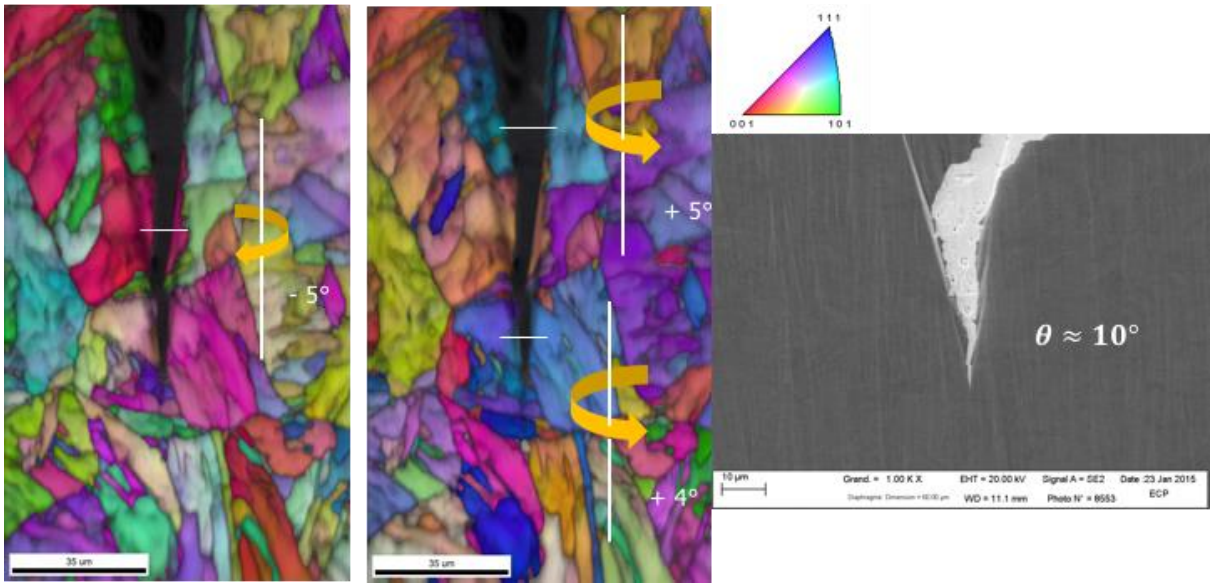


Figure 4.68: a) IPF view+axis of rotation on the lips of the profile b) IPF view of 90° rotated +axis of rotation on the lips of the profile c) SEM view of the area from Sample 3 selected for EBSD mapping.

The typical size of a martensite lath is of the order of 500 nm to 1 µm width for a length of several µm. The EBSD minimum step size is 50 nm. Since the EBSD technique has a limited resolution compared with the scale of the T91 microstructure, it is easy to miss domain boundaries by EBSD when the microstructure has such a small grain size. It is also experimentally difficult to carry out EBSD analysis with accuracy near edges due to potential electron beam drift during scanning. The main crack was therefore poorly characterized with this technique. The lowest resolution limit of conventional EBSD is removed by the TEM automated orientation technique applied on the FIB lift-outs. In addition, the FIB sampling technique allows to extract immediately below the fracture surface and to carry out a correlation with the position of the fracture surface. The use of TEM automated mapping technique gave extremely accurate results directly relevant for the analysis of the main crack next to the fracture surface as opposed to EBSD. The results of the use of such technique is shown in Figure 4.68. The fracture surface was seen in SEM as a step and a rather flat adjacent fracture surface on each side of the step. The automated mapping reveals that the step is indeed formed by two contiguous interlath cracks (see arrow in Figure 4.68). The contrast seen as a step in SEM would be produced by the interaction of the scanning electron beam with this surface relief. The plastically deformed microstructure composed of unbroken but distorted martensitic laths away from the step appears quite clearly suggesting that actually the flat surface is the result of an interlath debonding. It is interesting to mention that many microstructural details give rise to a surface relief giving a definite “microstructural” imprint on the SEM image.

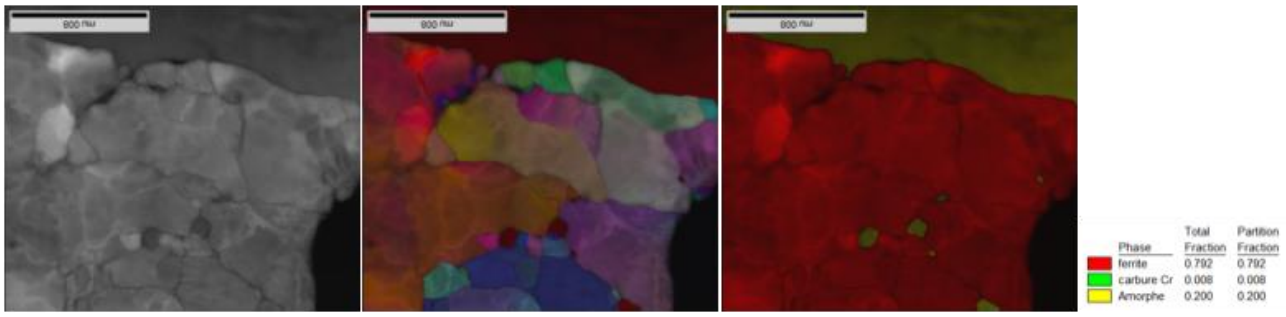


Figure 4.68: a) TEM view of the area from Sample 4 selected via FIB sampling b) high resolution orientation mapping c) phase map of the corresponding area

# 5 Discussion

The low cycle fatigue properties of the 9Cr–1Mo ferritic-martensitic steel have been tested in an LOC LBE environment and in vacuum at 160–450 °C under a strain amplitude of 0.42% and at a strain rate of $4.5 \times 10^{-3}$ $s^{-1}$. The variation of the fatigue lives with temperature shows a clear fatigue endurance "trough" in the presence of LOC LBE: the fatigue life decreases as the temperature is increased from 160 to 350 °C, while a reverse trend is observed in the temperature range of 350–450 °C. However, no such a strong temperature dependence of the fatigue endurance is visible when the steel is tested in vacuum. SEM fractographic micrographs show that all the specimens tested in LOC LBE at all the temperatures are characterized by quasi-cleavage fracture features. Interestingly, the EBSD observations show that martensitic laths in the vicinity of the fatigue crack walls or of the fracture surfaces are transformed into very fine equiaxed subgrains after testing in vacuum at 160–450 °C. The formation of the fine subgrains is attributed to extensive cyclic plasticity around the crack tips. By contrast, no such microstructural modifications are present in the specimens tested in LOC LBE. These microstructural differences suggest that LME is able to occur throughout the fatigue crack propagation in the full range of the temperatures investigated and is not very sensitive to temperature. Furthermore, it can be deduced that when LME occurs, plastic strain around the crack tips is greatly reduced or is localized into a very small region. The major contribution to the "trough" is from the effect of temperature on the fatigue crack initiation and subcritical propagation.

Figure 5.1 shows a schematic illustration of a possible mechanism for secondary cracking in inert (Figure 5.1a) and LBE (Figure 5.1b) environment. The fatigue crack tip in inert environment (Figure 5.1a) can be strongly blunted due to extensive plastic flow around the crack tip and the applied stress might not be released in time, so that a significantly large tensile stress is created to act on a notch-like root of a fatigue striation. As a result, a secondary crack can be formed at the fatigue striation and then deeply propagates into the bulk. In contrast, in LBE (Figure 5.1b) the weakening effect results in a much less blunted crack tip. Consequently, the applied stress can be taken away mostly by fast crack propagation, leading to a small tensile stress acting on the root of the fatigue striation and then the formation of a shallow secondary crack [33]. A more detailed description of this mechanism can be found in Gong et al. [33].

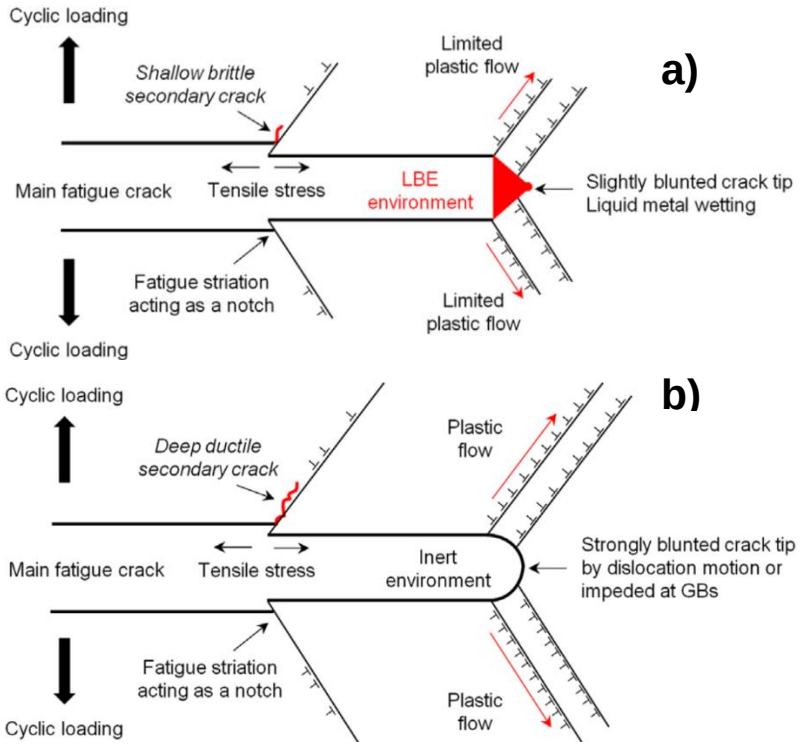


Figure 5.1: Outline of the formation mechanism of secondary cracks in a) LBE environment and b) inert environment [33].

A schematic illustration of fatigue crack propagation modes in the presence of LBE can be found in Figure 5.2. During propagation the fatigue crack cuts through prior austenite grain boundaries and interacts with the microstructure inside. In case the laths are inclined relative to the propagation axis alternate occurrence of translath and interlath cracking can occure Figure 5.2a. If the laths are laths are parallel or only slightly inclined to the crack propagation direction then complete interlath decohesion splitting two neighboring laths occur

(Figure 5.2b). Secondary cracking can occur on stress concentrators like sharp fatigue striations, carbides or grain boundaries (Figure 5.2c). The secondary crack behaves in a similar manner as the main crack but will be arrested at microstructural barriers once the main crack overcomes its barriers [33].

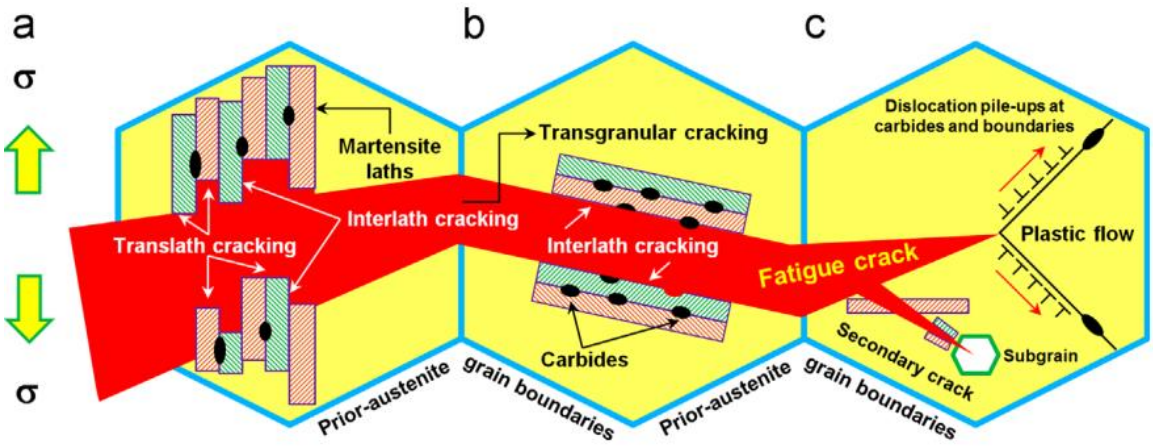


Figure 5.2: Illustration of different crack propagation modes [33].

A possible mechanism to explain LME is schematically illustrated in Figure 5.3. $\sigma_c$ defines the critical normal stress required to break the atomic bond A–A1, and $\tau_c$ determines the critical resolved shear stress to activate dislocation glide at a given slip plane ahead of the crack tip. In general, $\sigma_c$ is much greater than $\tau_c$, particularly for a ductile metal. Therefore, it is assumed that the moderate weakening effect reduces $\sigma_c$ but $\tau_c$ is not influenced and that the reduced $\sigma_c$ still remains higher than $\tau_c$. As described in Figure 5.3a, the initial normal stress σy acting on the atomic bond A–A1 being in intimate contact with the liquid metal atoms is limited or zero. In order to allow LME to take place by breaking the atomic bond A–A1, an external tensile force has to apply to the specimen to increase the normal stress $\sigma_y$ to overcome

σc. Under the external tensile force, both σy and τ (the actual shear stress at the slip plane) will increase simultaneously but the rate of their increase should be different. It is assumed that τ reaches $\tau_c$ earlier compared to $\sigma_y$ reaching $\sigma_c$, because the reduced $\sigma_c$ bythe moderate weakening still remains higher than $\tau_c$. Consequently, $\tau_c$ is surpassed by τ before $\sigma_y$ exceeds $\sigma_c$, activating dislocation glide and localizing plastic strain in a plastic zone around the crack tip. During the plastic deformation, tiny voids, dislocations and other defects are produced and stored in the plastic zone, leading to strain hardening and poor dislocation mobility. As the strain hardening proceeds, $\tau_c$ starts to climb up and thus s gets difficult to approach the increased $\tau_c$, but $\sigma_y$ becomes likely to surpass $\sigma_c$. In other words, $\sigma_y$ could overcome the actual $\sigma_c$ reduced by the weakening effect, before s reaches the new $\tau_c$ increased by the strain hardening. Immediately after this event occurs, the atomic bond A–A1 is broken and rupture occurs fast through the hardened plastic zone containing the ductile features like tiny voids, see Figure 5.3b. The cracking will not stop or slow down until the crack tip arrives at a new non-hardened place where $\tau_c$ is low. The same process repeats until the final failure of the specimen. After the failure, the fracture surface should be characterized by a mixture of tiny dimples and cleavage features, which could be termed as quasi-cleavage. It should be emphasized that the crack propagation is not due to nucleation and coalescence of the tiny voids during the plastic deformation in the plastic zone. The sizes of the ductile dimples left on the fracture surface depend on the extent of plastic deformation ahead of the crack tip or the magnitude of the weakening effect. In other words, when the actual $\sigma_c$ reduced by the weakening is higher than $\tau_c$, the greater the difference between these two parameters, the more plastic deformation and ductile features. If $\tau_c$ is lower than $\sigma_c$ after weakening, it is expected that plastic deformation cannot happen and ductile features should be absent on the fracture surface. Nevertheless, in the case of the T91/LBE couple, most likely the weakening effect decreases $\sigma_c$ to be comparable with or to be slightly higher than $\tau_c$, so that a limited amount of plastic deformation can be sufficient to raise $\tau_c$ and in turn $\sigma_y$ can exceed $\sigma_c$ earlier than τ surpassing $\tau_c$. This means that the atomic bonds at the crack tip can be broken before extensive plastic deformation is activated to create evident ductile characteristics like large voids. A more thorough explanation of the mechanism can be found in Gong et al. [44]

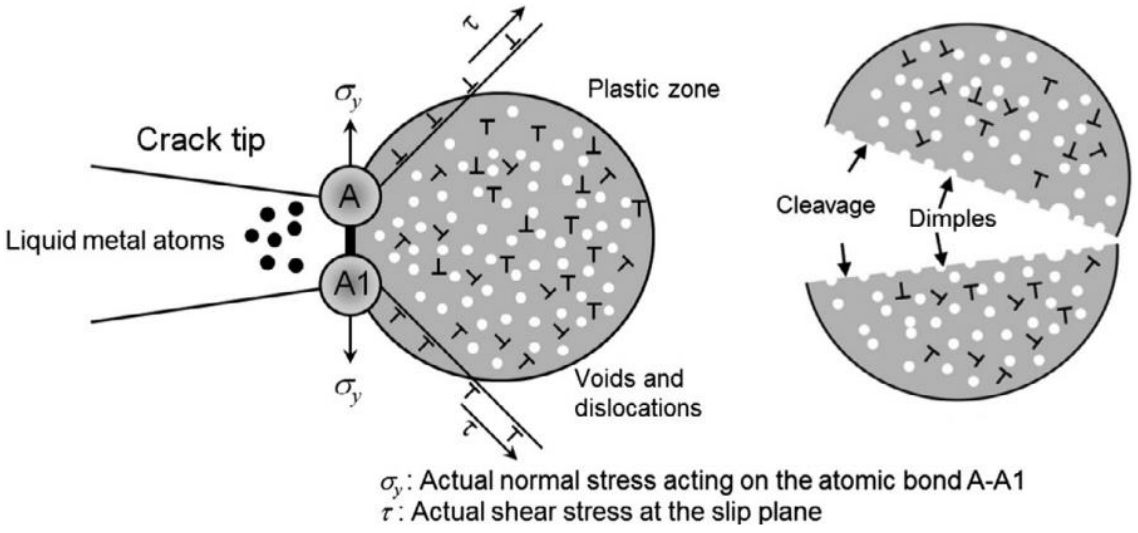


Figure 5.3: Schematic outline of a LME enhanced crack propagation mechanism [50].

An attempt to explain markings on fracture surface which have been reported in the past by other researchers [12, 5] has been made. The tensile behavior of notched T91 in contact with LBE at 350 °C has been studied and cracking jumps were observed at the tensile curves and the fracture surfaces. The presence of this unique and interesting phenomenon can be attributed to the coupled effects of LME and compliance of the tensile test machines, because such markings or steps tended to disappear with increasing stiffness of the tensile machines. The results presented in this work also demonstrate that T91 is strongly susceptible to liquid LBE embrittlement and the presence of a notch can significantly enhance crack initiation which is necessary to break surface oxides for triggering the subsequent LME effect.

The CT fracture mechanics test in liquid metal presents various areas corresponding to all the steps required to correctly assess the resistance to cracking in LBE (pre-cracking in LBE, crack propagation, final cracking). The EBSD analysis on transverse cuts of CT-sample 1, CT-sample 2 and CT-sample 3 revealed that numerous interlath cracks are seen at each of these stages. They are seen in the specimen part fractured at low temperature in the intrinsic brittle range of a martensitic steel (sample 1), in the pre-cracked area (sample 2) and in the crack propagation area (sample 3). In the area fractured in liquid nitrogen, some cleavage was also found as expected with the standard quasi-cleavage fracture mode with its distinctive fracture surface aspect. The intrinsic brittleness of martensitic steels at low temperature is therefore a mixture of cleavage and interlath cracking. In areas affected by LBE (pre-cracking and crack propagation areas), a cleavage fracture mode was not found. While somehow tricky for cracks in the same martensitic variant, it was nevertheless sufficiently resolved to be able to conclude about a major influence of the interlath character of the crack path in several typical areas of these stages. This study adds more cases to the already existing database of fracture modes investigation in LBE [50]. Furthermore, it confirms the importance of a dominance of interlath cracking in contact with LBE with all secondary cracks. However, because it was not carried out with the main crack due to EBSD limitations, an increase of the resolution of the analysis was required to be able to assess the links of the fracture surface topology with the underlying microstructure.

The running creep-to-rupture tests at 450°C and 375 MPa are long-term tests. 316L shows one order of magnitude higher secondary creep rate in liquid metal in comparison to air during the first 3,260 h. Despite the oxygen concentration in LBE is very low, no transition from the secondary to the tertiary creep was observed in both cases up to date. A question, whether oxides form on the steel surface and delay a steel damage during the test in LBE or diffusion processes in the steel are slow-going so that the dissolution of the steel elements takes probably place but is not critical, is still open. Nevertheless, it is worth to notice that the deformation rate at 450°C up to now is not critical for possibly initiated and intensive running dissolution attack.

Much higher secondary creep rate of the steel in LBE at 500 and 550°C results in dissolution of Cr and Ni as well as liquid metal attack, although Cr-rich oxides form on the steel surface. At 500°C, the austenitic steel tested in LBE at low oxygen concentration and 325 MPa ruptured after 5,025 h, while the test in air is still running after more than 10,000 h. The ferritisation of the steel surface in LBE and a liquid metal attack affect negative on the creep properties of 316L.

At 550°C, the damage of the steel in LBE at low oxygen concentration and 300 MPa is considerably stronger than at 500°C and resulted in much shorter time-to-rupture, viz. 1,060 h. The mechanical properties are strongly affected by LBE at low oxygen concentration in comparison to air. But even increasing the oxygen concentration up to $10^{-6}$ wt% at 550°C with a goal to form a stable oxide scale on the steel surface did not

affect the mechanical properties beneficially: three specimens tested at $10^{-6}$ wt% dissolved oxygen in LBE at 550°C ruptured after less than 365 h.

The above-mentioned data for time-to-rupture, $t_R$ obtained under different conditions is provided for the specimen with initial D = 3 mm. Varying D under the same applied stress has to change $t_R$, since corrosion rate remains the same while the real stress changes depending on the size of load-bearing cross-section. Therefore, the bigger D, the higher $t_R$ is to expect.

The first of its kind FIB-ASTAR TEM analysis of a step below the fracture surface (or equivalently the analysis of the main crack) in this case of LME provides a detailed view of typical features of the fracture surface. It reveals that the steps are the leftovers of intergranular or interlath cracking as well. A very important remark here is that individual martensitic laths are not fractured in a cleavage mode but that there are heavily deformed instead. The crack most likely grows at low speed along lath boundaries and propagation is probably strain controlled, giving its unusual look. A full quantification of the fraction of the fracture surface concerned by this fracture mode is probably out of the range of the FIB technique because it is a very localized and very time-consuming analysis. However, combined with prior results of ours, this further strengthen the conclusion that LME of T91 by LBE is basically an interfacial fracture process in a deformed microstructure. This constitutes further argument that the main issue in LME is to understand why and how the grain boundaries are embritled by LBE. This also strengthen the initial conclusion reached already in reference [50] that the SEM qualification of quasi-cleavage is misleading for LME and that a detailed analysis requires to take into account at the nanoscale the underlying microstructure.

This raises the level of understanding of LME of T91. The findings of this work pave the way for a better assessment of LME that future work on the subject will have to consider. Modelling of LME has imperatively to take into account its intergranular character. As a side effect of these findings, LME of the T91 steel is a lot closer to the phenomenology of LME model systems [51] than previously thought. Another related issue is whether or not LBE can diffuse in grain boundaries, it is still out of reach of electronic microscopy analytical techniques at this point. At last, this understanding may give an opportunity to tune the microstructure to limit or suppress LME. It appears clearly that in the crack paths observed by this analysis, carbides are rarely found. There are also sparsely present on the fracture surface. Given the fact that the main carbides of the T91 steel ($Cr_{23}C_6$, NbC, VC) are known not to be easily wetted by Pb or Bi [52], it may be possible to limit the advance of LBE in the microstructure. One could try to modify the precipitation of carbides at grain boundaries, either by modifying the heat treatment of the steel or by increasing its carbon content. A very interesting question then would be to see if the variability in the fracture toughness reduction [37, 20] can be correlated with the content and distribution of the carbides in the microstructure. This is left for future work.

# 6 Conclusions

- Microstructural observations on fatigue samples show that the dominant failure mode was intergranular or interlath rather than transgranular or translath,. The amount of intergranular or interlath decohesion was orientation dependent. Further investigation on this topic are still needed.
- Fine scale observations by EBSD and TEM on the crack propagation induced by LBE on T91 steel shows that the interlath crack path is key to the correct understanding of LME fracture surfaces. LME of martensitic steels shares many characteristics of LME of model systems.
- Results of crack propagation measurements can be influenced by machine compliance.
- Fracture surface markings reported earlier by different researchers could be related to equipment properties (system compliance) rather than material properties.
- The strain control procedure has no effect since stress values are nearly the same for a given strain range+
- During creep on 316L, ferritisation due to Ni loss, decreases creep life.
- Further investigations on 316L in LBE are required to understand these recent new findings.
- LBE significantly decreases fatigue life of T91. The procedure for immersion of the specimen in LBE together with the removal of oxygen can impact the fatigue lives.
    - The range of oxygen content in the LBE reached by SCK-CEN is so low that all fatigue life data fall in the same range. The oxygen content reached by CNRS-Lille is higher and the two groups of data point out a critical range of oxygen where detrimental effect can be observed in comparison with oxygen saturated LBE. This can be explained by a non homogeneous partition of oxygen in LBE which can provide enough local high oxygen content to lead to similar behavior as in high oxygen LBE.
    - The apparent higher fatigue resistance observed by SCK-CEN (in comparison with CNRS-Lille) may be related to presence of an oxide layer at the external surface of the fatigue specimen which protect the material against LBE.

# 7 List of publications

The following publications received partial financial support from the MatISSE project.

X. Gong, P. Marmy, L. Qin, B. Verlinden, M. Wevers and M. Seefeldt, "Effect of liquid metal embrittlement on low cycle fatigue properties and fatigue crack propagation behavior of a modified 9Cr-1Mo ferritic-martensitic steel in an oxygen-controlled lead-bismuth eutectic environment at 350 °C" Materials Science and Engineering A, vol. 618, pp. 406-415, 2014

X. Gong, P. Marmy, A. Volodin, B. Amin-Ahmadi, L. Qin, D. Schryvers, S. Gavrilov, E. Stergar, B. Verlinden, M. Wevers and M. Seefeldt, "Multiscale investigation of quasi-brittle fracture characteristics in a 9Cr-1Mo ferritic martensitic steel embrittled by liquid lead-bismuth under low cycle fatigue" *Corrosion Science,* vol. 102, pp. 137-152, 2015.

X. Gong, P. Marmy, B. Verlinden, M. Wevers and M. Seefeldt, "Low cycle fatigue behavior of a modified 9Cr-1Mo ferritic-martensitic steel in lead-bismuth eutectic at 350°C - Effects of oxygen concentration in the liquid metal and strain rate," vol. 94, pp. 377-391, 2015

X. Gong, P. Marmy, L. Qin, B. Verlinden, M. Wevers and M. Seefeldt, "Temperature dependence of liquid metal embrittlement susceptibility of a modified 9Cr-1Mo steel under low cycle fatigue in lead-bismuth eutectic at 160-450°C" Journal of Nuclear Materials, vol. 468, pp. 289-298, 2016

X. Gong, E. Stergar, P. Marmy and S. Gavrilov, "Tensile fracture behavior of notched 9Cr-1Mo ferritic-martensitic steel specimens in contact with liquid lead-bismuth eutectic at 350 °C" vol. 692, pp. 139-145, 2017.

# 8 References


[1] H. A. A. Abderrahim, P. Baeten, D. De Bruyn, J. Heyse, P. Schuurmans and J. Wagemans, "MYRRHA, a Multipurpose hYbrid Research Reactor for High-end Applications," *Nuclear Physics News,* vol. 20, pp. 24-28, #feb# 2010.

[2] H. A. Abderrahim, "Multi-purpose hYbrid Research Reactor for High-tech Applications a multipurpose fast spectrum research reactor," *Int. J. Energy Res.,* vol. 36, pp. 1331-1337, 2012.

[3] Y. Dai, B. Long and F. Groeschel, "Slow strain rate tensile tests on T91 in static lead-bismuth eutectic," *Journal of Nuclear Materials,* vol. 356, pp. 222-228, 2006.

[4] S. Guerin, J. L. Pastol, C. Leroux and D. Gorse, "Synergy effect of LBE and hydrogenated helium on resistance to LME of T91 steel grade," *Journal of Nuclear Materials,* vol. 318, pp. 339-347, 2003.

[5] J. Klecka, F. Di Gabriele and A. Hojna, "Mechanical properties of the steel T91 in contact with lead," *SI:NENE 2013,* vol. 283, pp. 131-138, #mar# 2015.

[6] B. Long and Y. Dai, "Investigation of LBE embrittlement effects on the fracture properties of T91," *Journal of Nuclear Materials,* vol. 376, pp. 341-345, 2008.

[7] B. Long, Y. Dai and N. Baluc, "Investigation of liquid LBE embrittlement effects on irradiated ferritic/martensitic steels by slow-strain-rate tensile tests," *Journal of Nuclear Materials,* vol. 431, pp. 85-90, #dec# 2012.

[8] B. Long, Z. Tong, F. Groschel and Y. Dai, "Liquid Pb-Bi embrittlement effects on the T91 steel after different heat treatments," *Journal of Nuclear Materials,* vol. 377, pp. 219-224, 2008.

[9] I. Serre and J.-B. Vogt, "Heat treatment effect of T91 martensitic steel on liquid metal embrittlement," *Journal of Nuclear Materials,* vol. 376, pp. 330-335, 2008.

[10] I. Serre and J.-B. Vogt, "Liquid metal embrittlement of T91 martensitic steel evidenced by small punch test," *Nuclear Engineering and Design,* vol. 237, pp. 677-685, 2007.

[11] J. Van den Bosch, G. Coen, A. Almazouzi and J. Degrieck, "Fracture toughness assessment of ferritic-martensitic steel in liquid lead-bismuth eutectic," *Journal of Nuclear Materials,* vol. 385, pp. 250-257, 2009.

[12] J. Van den Bosch, G. Coen, P. Hosemann and S. A. Maloy, "On the LME susceptibility of Si enriched steels," *J. Nucl. Mater.,* vol. 429, pp. 105-112, 2012.

[13] J. Van den Bosch, P. Hosemann, A. Almazouzi and S. A. Maloy, "Liquid metal embrittlement of silicon enriched steel for nuclear applications," *J. Nucl. Mater.,* vol. 398, pp. 116-121, 2010.

[14] A. Verleene, J. B. Vogt, I. Serre and A. Legris, "Low cycle fatigue behaviour of T91 martensitic steel at 300 degrees C in air and in liquid lead bismuth eutectic," *International Journal of Fatigue,* vol. 28, pp. 843-851, 2006.

[15] J.-B. Vogt, A. Verleene, I. Serre and A. Legris, "Mechanical behaviour of the T91 martensitic steel under monotonic and cyclic loadings in liquid metals," *Journal of Nuclear Materials,* vol. 335, pp. 222-226, 2004.

[16] J.-B. Vogt and I. Proriol-Serre, "Fatigue Behaviour of a Martensitic and an Austenitic Steel in Heavy Liquid Metals," *Procedia Engineering,* vol. 55, pp. 812-818, 2013.

[17] J.-B. Vogt, A. Verleene, I. Serre, F. Balbaud-Celerier, L. Martinelli and A. Terlain, "Understanding the liquid metal assisted damage sources in the T91 martensitic steel for safer use of ADS," *Engineering Failure Analysis,* vol. 14, pp. 1185-1193, 2007.

[18] C. Ye, J.-B. Vogt and I. Proriol Serre, "Liquid metal embrittlement of the T91 steel in lead bismuth eutectic: The role of loading rate and of the oxygen content in the liquid metal," *Materials Science and Engineering: A,* vol. 608, pp. 242-248, #jul# 2014.

[19] C. Ye, J.-B. Vogt and I. Proriol-Serre, "Brittle fracture of T91 steel in liquid lead-bismuth eutectic alloy," *Nuclear Engineering and Design,* pp. --.

[20] T. Auger, D. Gorse, Z. Hamouche-Hadjem, J. V. den Bosch, G. Coen, A. Almazouzi, A. Hojna, K. Dalikova, F. D. Gabriele, M. Serrano, A. Gessi, P. Agostini, J.-B. Vogt and I. Serre, "Fracture mechanics behavior of the T91 martensitic steel in contact with liquid lead--bismuth eutectic for application in an accelerator driven system," *Journal of Nuclear Materials,* vol. 415, pp. 293-301, 2011.

[21] T. Auger, D. Gorse, Z. Hamouche-Hadjem, J. Van den Bosch, G. Coen, A. Almazouzi, A. Hojna, K. Dalikova, F. Di Gabriele, M. Serrano, A. Gessi, P. Agostini, J.-B. Vogt and I. Serre, "Fracture mechanics behavior of the T91 martensitic steel in contact with liquid lead-bismuth eutectic for application in an accelerator driven system," *Journal of Nuclear Materials,* vol. 415, pp. 293-301, 2011.

[22] F. Di Gabriele, A. Doubkova and A. Hojna, "Investigation of the sensitivity to EAC of steel T91 in contact with liquid LBE," *Journal of Nuclear Materials,* vol. 376, pp. 307-311, 2008.

[23] A. Hojna and F. Di Gabriele, "On the kinetics of LME for the ferritic-martensitic steel T91 immersed in liquid PbBi eutectic," *Journal of Nuclear Materials,* vol. 413, pp. 21-29, #jun# 2011.

[24] S. Hong, "The tensile and low-cycle fatigue behavior of cold worked 316L stainless steel," *International Journal of Fatigue,* no. 26, p. 899–910, 2004.

[25] M. Mataya, E. Nilsson, E. Brown and G. Krauss, "Hot working and recrystallization of As-Cast 316L," *Metall and Mat Trans,* vol. A, no. 34, p. 1683–1703, 2003.

[26] M. Abbod, C. Sellars, A. Tanaka, D. Linkens and M. Mahfouf, "Effect of changing strain rate on flow stress during hot deformation of Type 316L stainless steel," *Materials Science and Engineering,* vol. A, no. 491, p. 290–296, 2008.

[27] E. Otero, Padro, Utrilla, M. E. Saenz and J. Alvarez, "Corrosion behaviour of AISI 293L and 205L stainless steels prepared by powder metallurgy in the presence of sulfuric and phosphoric acid," *Corrosion Science,* p. 1421–1434, 1998.

[28] T. S. Byun and T. G. Lach, "Mechanical Properties of 304L and 316L Austenitic Stainless Steels after Thermal Aging for 1500 Hours," *LWR Sustainability R&D Cast Stainless Steels Aging,* Vols. (WP#: LW-16OR040215), no. M3LW-16OR0402153, 2016.

[29] R. Desu, H. N. Krishnamurthy, A. Balu, A. Gupta and S. Singh, "Mechanical properties of Austenitic Stainless Steel 304L and 316L at elevated temperatures," *Journal of Materials Research and Technology,* no. 5, p. 13–20, 2016.

[30] D. Gorse-Pomonti and V. Russier, "Liquid metals for nuclear applications," *Journal of Non-Crystalline Solids,* no. 353, p. 3600–3614, 2007.

[31] X. Gong, P. Marmy, L. Qin, B. Verlinden, M. Wevers and M. Seefeldt, "Effect of liquid metal embrittlement on low cycle fatigue properties and fatigue crack propagation behavior of a modified 9Cr-1Mo ferritic-martensitic steel in an oxygen-controlled lead-bismuth eutectic environment at 350 °C (MatISSE)," *Materials Science and Engineering A,* vol. 618, pp. 406-415, 2014.

[32] J. van den Bosch and A. Almazouzi, "Procurement and characterisation of T91 and SS316L plates," *EUROTRANS FI6W-CT-2004-516520, Deliverables: D 4.5a & D 4.6, R4197,* 2005.

[33] S. Ren-bo, X. Jian-ying and H. Dong-po, "Characteristics of mechanical properties and microstructure for 316L austenitic stainless steel," *Journal of iron and steel research, International 2011,* p. 53–59, 2011.

[34] P. Marmy and X. Gong, "LIMETS 3, a novel system for high strain fatigue testing in lead-bismuth eutectic," *Journal of Nuclear Materials,* vol. 450, pp. 256-261, #jul# 2014.

[35] F. Ersoy, S. Gavrilov and K. Verbeken, *J. Nucl. Mater.,* no. 472 , pp. 171-177, 2016.

[36] S. Berger and e. al., "Mitigation of crack initiation in LWRs (MICRIN+)," in *Eurocorr, Paper No. 65952*, Montpellier, 2016.

[37] Handbook on lead-bismuth eutectic alloy and lead properties, materials compatibility, thermal-hydraulics and technologies, 2007th ed., Issy-les-Moulineaux, France: OECD Nuclear Energy Agency, 2007.

[38] M. Yurechko-Hussy, C. Schroer, A. Skrypnik, O. Wedemeyer and K. J., "Creep behavior of ferritic/martensitic steel T91 in oxygen-containing Pb and LBE at 450-650°C," in *24th Int. Conf. on Nuclear Engineering (ICONE24)*, Charlotte, NC, USA, June 26–30, 2016.

[39] C. Schroer, O. Wedemeyer and J. Konys, "Aspects of minimizing steel corrosion in liquid lead-alloys by addition of oxygen," *Nuclear Engineering and Design,* no. 241 , p. 4913–4923, 2011.

[40] B. Barkia, T. Auger, J. L. Courouau and J. Bourgon, *Corros. Sci. ,* no. 127 , p. 213–221, 2017.

[41] E. F. Rauch, M. Véron, J. Portillo, D. Bultreys, Y. Maniette and S. Nicolopoulos, *Microsc. and Anal.,* no. 22 , pp. 5-8, 2008.

[42] X. Gong, P. Marmy, L. Qin, B. Verlinden, M. Wevers and M. Seefeldt, "Temperature dependence of liquid metal embrittlement susceptibility of a modified 9Cr-1Mo steel under low cycle fatigue in lead-bismuth eutectic at 160-450°C (MatISSE)," *Journal of Nuclear Materials,* vol. 468, pp. 289-298, #jan# 2016.

[43] X. Gong, P. Marmy, A. Volodin, B. Amin-Ahmadi, L. Qin, D. Schryvers, S. Gavrilov, E. Stergar, B. Verlinden, M. Wevers and M. Seefeldt, "Multiscale investigation of quasi-brittle fracture characteristics in a 9Cr-1Mo ferritic martensitic steel embrittled by liquid lead-bismuth under low cycle fatigue (MatISSE)," *Corrosion Science,* pp. --.

[44] X. Gong, E. Stergar, P. Marmy and S. Gavrilov, "Tensile fracture behavior of notched 9Cr-1Mo ferritic-martensitic steel specimens in contact with liquid lead-bismuth eutectic at 350 °C (MatISSE)," vol. 692, pp. 139-145, 2017.

[45] D. Kalkhof and M. Grosse, "Influence of PbBi environment on the low-cycle fatigue behavior of SNS target container materials," *Journal of Nuclear Materials,* vol. 318, pp. 143-150, 2003.

[46] M. Yurechko, C. Schroer, O. Wedemeyer, A. Skrypnik and J. Konys, "Creep-to-rupture of 9%Cr steel T91 in air and oxygen-controlled lead at 650°C," *Journal of Nuclear Materials,* vol. 419 , p. 320–328, 2011.

[47] O. Picho, Beständigkeit von Nickel- Chrom-Legierung und Eisenaluminidschnichten in Sauerstoffhaltigen flüssigen Bleilegierungen, Karlsruhe: Karlsruher Institut für Technologie (KIT), Diss., 2014, KIT-Bibliothek, 2014.

[48] V. Tsisar, C. Schroer, O. Wedemeyer, A. Skrypnik and J. Konys, "Corrosion behavior of austenitic steels 1.4970, 316L and 1.4571 in flowing LBE at 450 and 550°C with 10−7mass% dissolved oxygen," *Journal of Nuclear Materials,* no. 454 , p. 332–342, 2014.

[49] X. Gong, P. Marmy, B. Verlinden, M. Wevers and M. Seefeldt, "Low cycle fatigue behavior of a modified 9Cr-1Mo ferritic-martensitic steel in lead-bismuth eutectic at 350°C - Effects of oxygen concentration in the liquid metal and strain rate," vol. 94, pp. 377-391, #may# 2015.

[50] M. L. Martin, T. Auger, D. D. Johnson and I. M. Robertson, *J. Nucl. Mater. ,* no. 426 , pp. 71-77, 2012.

[51] K. Wolski and V. Laporte, *Mater. Sci. Eng.,* vol. A , no. 495 , p. 138–146, 2008.

[52] G. V. Samsonov, A. D. Panasyuk, G. K. Kozina and Porosh, *Metall.,* no. 11 , pp. 42-48, 1968.